Monitoring tumour response to extracellular matrix modulation with multiparametric MRI

Emma L. Reeves

A thesis submitted for the degree of

Doctor of Philosophy

from the

University of London

Division of Radiotherapy & Imaging

The Institute of Cancer Research, London

December 2021

Declaration

I hereby declare that this thesis reports on my own original work. Any contribution made to this research by others whom I have worked with is explicitly acknowledged in the thesis.

Emma Reeves

Abstract

Primary breast tumours are characterised by a dense extracellular matrix (ECM), with accumulation of collagen and hyaluronan (HA). This stromal dense phenotype is associated with tumour progression, metastasis and poor drug delivery. PEGPH20 degrades HA and has been shown to improve tumour response to therapy. Imaging biomarkers which inform on therapeutic efficacy may accelerate development of ECM targeted therapies.

This PhD used a pre-clinical multiparametric MRI approach to identify imaging biomarkers that can inform on breast tumour response to PEGPH20. Multiparametric MRI was performed before and after PEGPH20 treatment in three *in vivo* breast tumour models with different baseline HA accumulation and included MRI relaxometry (T_1 and T_2), magnetisation transfer (MT) imaging, diffusion weighted imaging (DWI), intrinsic susceptibility MRI (R_2*), and MR elastography (MRE).

4T1/HAS3 tumours had the highest baseline HA accumulation. In this model, T_1, T_2, and the apparent diffusion coefficient (ADC) decreased and MT ratio (MTR) and R_2* increased following PEGPH20 treatment. However, T_1, T_2, MTR and R_2* were not significantly different following PEGPH20 in MDA-MB-231 LM2-4 and 4T1 tumours which had lower baseline HA accumulation. There was a decrease in ADC in MDA-MB-231 LM2-4 tumours following PEGPH20, suggesting that this biomarker is the most sensitive to HA degradation. Despite no significant difference in ADC in 4T1 tumours, spatial correspondence between ADC and HA was apparent. The reduction in ADC is likely due to a PEGPH20-induced reduction of the extracellular space. In addition, of all the MRI biomarkers evaluated, ADC had the strongest correlation with percent HA.

Tumour viscoelastic properties, measured by MRE, increased following PEGPH20 in MDA-MB-231 LM2-4 breast tumours. Elevated stiffness is associated with tumour progression and so these data suggest a potentially

negative effect of PEGPH20. No change in viscoelastic properties was apparent following PEGPH20 in 4T1 and 4T1/HAS3 tumours.

In conclusion, this project revealed that ADC is the most sensitive biomarker of HA accumulation and its therapeutic degradation by PEGPH20. In addition, the increase in MDA-MB-231 LM2-4 tumour viscoelastic properties following PEGPH20 may be an early sign of tumour progression and indicate a negative effect of targeting the tumour associated ECM, but further investigation is needed.

Acknowledgements

This research was funded by the Cancer Research UK Centre at the ICR. I give huge thanks to my supervisor Dr Simon Robinson for his help, support and encouragement throughout my PhD. I would also like to thank my supervisor Dr Jin Li for always being there to answer my questions and offer advice, even after her move to China. Thanks to Dr Yann Jamin and Professor Jeff Bamber for their support and guidance. I also want to thank Dr David Kang and Dr Barbara Blouw from Halozyme Therapeutics for all their advice and willingness to share materials and methods. Thanks to Craig Cummings and James Sullivan for their assistance creating the MR elastography (MRE) platform used. Thanks to Professor Ralph Sinkus for his advice and expertise with MRE. Thanks to Dr Konstantinos Zormpas-Petridis for his assistance with the quantification of collagen distribution. Thanks to Dr Jessica Boult and Dr Carol Box for their advice, kind words and lab support. Thanks to the rest of the pre-clinical MRI team at the ICR (past and present), it has been a great pleasure working and learning alongside all of you. Finally, thank you to my family, friends and boyfriend for keeping me sane and always supporting me, I dedicate this PhD thesis to you.

"Never let the fear of striking out keep you from playing the game"

- A Cinderella Story, 2004

Contents

List of Tables

Chapter 1

Chapter 2

List of Figures

Chapter 1

Figure 1.9: A schematic of PEGPH20 treatment effects as a monotherapy and in combination with chemotherapy – adapted from [15]. Cancer and stromal cells are shown in blue and orange respectively. PEGPH20 can degrade HA (yellow), decompress blood vessels (red), and improve chemotherapy delivery (dark blue dots).

Figure 1.10: Measurement of viscoelastic properties with magnetic resonance elastography (MRE). The characteristics of the propagating mechanical wave will change depending on the local stiffness and viscosity of the tissue or phantom. Imaging the wave propagation with MRE can give, under certain simplifying assumptions, an estimate of the viscoelastic properties. Wave images provided by Professor Ralph Sinkus.

Chapter 2

Figure 2.1: Mould used to manufacture gelatine phantoms. The 3D printed design is identical in semi-cylindrical shape to the MRE set up (diameter 35 mm, length 80 mm).

Figure 2.2: Graphic describing the *in vivo* workflow used throughout this thesis. Pre-treatment MRI was performed when tumour reached sufficient size. Mice were then given 5 hours to recover from the anaesthesia before either saline or PEGPH20 (1 mg/kg) was administered intravenously. MRI was repeated 24 hours after treatment. After post-treatment MRI a terminal IFP measurement was taken, mice were killed (by cervical dislocation), and tumours were bisected at the MRI plane. One tumour half was embedded in formalin for histology and the other was weighed and freeze dried for estimation of tumour water content.

Figure 2.3: Graphical representation of the purpose-built MRE platform used. Figure adapted from [157]. During MRE, a mechanical vibration is generated by an electromagnetic shaker, transmitted through a flexible nylon rod to a square piston which is in direct contact with the tumour or phantom. A cantilever allows conversion of the horizontal vibration of the shaker into vertical vibrations onto the tissue or phantom.

Figure 2.4: Types of piston used for MRE. A semi-curved piston **(A)** was used for *in vivo* tumour studies and a flat piston **(B)** was used for gelatine phantoms. The depth of available pistons varied from 2 to 7 mm; the piston was changed to suit the size of the subject. Typically, a 5 mm semi-curved piston was used for 4T1 and 4T1/HAS3 tumours and a 3 mm semi-curved piston was used for MDA-MB-231 LM2-4 tumours.

Figure 2.5: Summary of the method used to separate total tissue pressure (TTP) into interstitial fluid pressure (IFP) and solid stress (SS) components. Images of the Millar SPR-1000 pressure catheter are shown. The probe was first covered with perforated tube to estimate the IFP, following which the tubing was removed to measure TTP. When both TTP and IFP are measured in the same region of the tumour the difference between them gives the SS. Figure created using [40].

Chapter 3

Figure 3.1: Multiparametric MRI of gelatine phantoms. Representative T_1, T_2, MTR and ADC maps are shown, alongside anatomical T_2-weighted (T_2w) images, for gelatine phantoms with concentrations of 6, 8, 10 and 12% (w/w). For each phantom, a region of interest (ROI; black dashed rectangle) was drawn within the shimmed region to calculate median T_1, T_2, MTR and ADC values.

Figure 3.2: Plots of T_1 (Pearson's correlation coefficient r = -0.76, p = 0.03), T_2 (r = -0.96, p = 0.0002), MTR (r = 0.94, p = 0.0004) and ADC (r = -0.90, p = 0.003) against gelatine phantom concentration (weight/weight percentage). Median values from each individual phantom are plotted (n = 2 for each concentration tested).

Figure 3.3: 4T1, 4T1/HAS3 and MDA-MB-231 LM2-4 tumour growth. Here tumour volume was measured using callipers. Each black line connects the data points from each individual tumour (4T1 n = 13, 4T1/HAS3 n = 23, and MDA-MB-231 LM2-4 n = 23). Tumour volume is shown up until the day of pre-treatment MRI. The doubling times for 4T1, 4T1/HAS3 and MDA-MB-231 LM2-4 tumours were 2.6 days, 2.4 days and 4.3 days respectively.

Figure 3.4: Anatomical T_2-weighted (T_2w) MRI and parameter maps of T_1, T_2, MTR and ADC, for a representative 4T1, 4T1/HAS3 and MDA-MB-231 LM2-4 tumour prior to and 24 hours after saline. The tumour ROI from which necrosis was excluded is shown by a white dashed line on the T_2-weighted images. The artefact on the 4T1 tumour ADC parametric maps was excluded from quantitative analyses.

Figure 3.5: Anatomical T_2-weighted (T_2w) MRI and parameter maps of T_1, T_2, MTR and ADC, for a representative 4T1, 4T1/HAS3 and MDA-MB-231 LM2-4 tumour prior to and 24 hours after PEGPH20 treatment (1 mg/kg). The tumour ROI from which necrosis was excluded is shown by a white dashed line on the T_2-weighted images.

Figure 3.6: MRI-derived tumour volume and median T_1, T_2, MTR and ADC for 4T1, 4T1/HAS3 and MDA-MB-231 LM2-4 tumours pre-saline, post-saline, pre-PEGPH20 and post-PEGPH20 (1 mg/kg). Data from each individual tumour are plotted, with saline controls in blue and PEGPH20 treated tumours in red. Sample sizes for 4T1, 4T1/HAS3 and MDA-MB-231 LM2-4 tumours were: n = 6 saline and n = 6 PEGPH20; n = 12 saline and n = 11 PEGPH20; and n = 11 saline and n = 12 PEGPH20 respectively.

Figure 3.7: Percentage change in MRI-derived tumour volume, T_1, T_2, MTR, and ADC between pre- and post-treatment MRI for saline and PEGPH20 treated mice bearing 4T1, 4T1/HAS3 or MDA-MB-231 LM2-4 tumours. PEGPH20 reduced the growth of 4T1 (***p=0.0005, unpaired Student's t-test), 4T1/HAS3 (****p<0.0001) and MDA-MB-231 LM2-4 (****p<0.0001) tumours. PEGPH20 treatment did not significantly change T_1, T_2, MTR and ADC in 4T1 tumours (ns; p>0.05). PEGPH20 reduced T_1 (**p=0.01), T_2 (**p=0.005), and ADC (*p=0.03), and increased MTR (****p<0.0001) in 4T1/HAS3 tumours. PEGPH20 treatment of MDA-MB-231 LM2-4 tumours decreased ADC (**p=0.003) but no significant change was seen in T_1, T_2 or MTR (ns; p>0.05). Data points are each individual tumour and are summarised by the cohort mean ± 1 SEM.

Figure 3.8: Measurements of IFP, SS and TTP in 4T1, 4T1/HAS3 and MDA-MB-231 LM2-4 tumours 24 hours after treatment with either saline (blue) or PEGPH20 (red). These invasive pressure measurements were taken following the post-treatment MRI from one region within the centre of each tumour. PEGPH20

treated tumours did not have significantly different IFP, SS or TTP compared to saline controls in any of the three breast tumour models (ns; p>0.05). A trend to lower IFP in PEGPH20 treated 4T1/HAS3 and MDA-MB-231 LM2-4 tumours was apparent (p = 0.08 and p = 0.06 respectively). There was also a trend to lower TTP in PEGPH20 treated 4T1 and 4T1/HAS3 tumours (p = 0.06 and p = 0.09 respectively). Each data point is from an individual tumour and these are summarised by the cohort mean ± 1 SEM.

Figure 3.9: Water content of 4T1, 4T1/HAS3 and MDA-MB-231 LM2-4 tumours 24 hours after treatment with either saline (blue) or PEGPH20 (red). Water content was measured ex vivo from one half of each tumour following post-treatment MRI and tumour pressure measurements. PEGPH20 treated MDA-MB-231 LM2-4 tumours had lower water content than saline control tumours (**p = 0.001). A trend to decreased water content in PEGPH20 treated 4T1 and 4T1/HAS3 tumours was apparent (p = 0.12 and p = 0.27 respectively). Each point is from an individual tumour and data are summarised by the cohort mean ± 1 SEM.

Figure 3.10: T_2-weighted (T_2w) MRI alongside aligned 4T1, 4T1/HAS3 and MDA-MB-231 LM2-4 tumour tissue sections (5 μm) stained with H&E, HTI-601 (HA), or picrosirius red (collagen I & III). Representative magnified images (20x) are presented alongside whole tumour section images for one saline control and one PEGPH20 treated tumour per in vivo model. Histology sections were closely spatially matched to the MRI.

Figure 3.11: Quantification of nuclear density, HA (%) and collagen I & III (%) from H&E, HTI-601 and picrosirius red staining. Quantification of HTI-601 staining revealed different baseline HA accumulation in 4T1, 4T1/HAS3 and MDA-MB-231 LM2-4 tumours and marked HA reduction in all models with PEGPH20 treatment (****p < 0.0001). Saline treated MDA-MB-231 LM2-4 tumours had significantly less collagen deposition compared to 4T1 (**p = 0.003) and 4T1/HAS3 (*p = 0.02) tumours.

Chapter 4

Figure 4.1: Evaluation of gelatine phantoms with MRE. Representative G_d, G_l, |G*|, and Y maps are shown, alongside anatomical T_2-weighted (T_2w) images, for

gelatine phantoms with concentrations of 6, 8, 10 and 12% (w/w). For each phantom, a ROI (black dashed rectangle) was drawn within the shimmed region to calculate median values of G_d, G_l, $|G^*|$, and Y.

Figure 4.2: Plots of elasticity (G_d; Pearson's correlation coefficient r = 0.99, p < 0.0001), viscosity (G_l; r = 0.99, p < 0.0001), the absolute value of the complex shear modulus ($|G^*|$; r = 0.99, p < 0.0001) and phase angle (Y; r = 0.88, p = 0.004) against gelatine phantom concentration (weight/weight percentage). Median values from each individual phantom are plotted (n = 2 for each gelatine concentration tested).

Figure 4.3: Anatomical T_2-weighted (T_2w) MRI and parameter maps of G_d, G_l, $|G^*|$ and Y, generated using MRE for a representative 4T1, 4T1/HAS3 and MDA-MB-231 LM2-4 tumour prior to and 24 hours after saline. The tumour ROI from which necrosis was excluded is shown by a white dashed line.

Figure 4.4: Anatomical T_2-weighted (T_2w) MRI and parameter maps of G_d, G_l, $|G^*|$ and Y, generated using MRE for a representative 4T1, 4T1/HAS3 and MDA-MB-231 LM2-4 tumour prior to and 24 hours after PEGPH20 treatment (1 mg/kg). The tumour ROI from which necrosis was excluded is shown by a white dashed line.

Figure 4.5: Median G_d, G_l, $|G^*|$, and Y values for 4T1, 4T1/HAS3 and MDA-MB-231 LM2-4 breast tumours before either saline or PEGPH20 treatment. 4T1 tumours exhibited significantly higher G_d, G_l, and $|G^*|$ at baseline compared to 4T1/HAS3 and MDA-MB-231 LM2-4 tumours (one-way ANOVA; ***p=0.0002, ****p<0.0001). 4T1/HAS3 tumours had significantly higher G_d (**p=0.008), but similar G_l and $|G^*|$ (p>0.05), compared to MDA-MB-231 LM2-4 tumours. Y was similar across all tumour models (p>0.05). Data are summarised by the cohort mean ± 1 SEM.

Figure 4.6: Ladder plots showing individual median values of G_d, G_l, $|G^*|$, and Y for 4T1, 4T1/HAS3 and MDA-MB-231 LM2-4 tumours prior to and post-treatment with either saline (blue) or PEGPH20 (red). Sample sizes for 4T1, 4T1/HAS3 and MDA-MB-231 LM2-4 tumours were n = 6 saline and n = 5 PEGPH20; n = 12 saline and n = 10 PEGPH20; and n = 9 saline and n = 11 PEGPH20 respectively.

Figure 4.7: Percentage change in G_d, G_l, |G*|, and Y between pre- and post-treatment MRI for saline and PEGPH20 treated mice bearing 4T1, 4T1/HAS3 or MDA-MB-231 LM2-4 tumours. PEGPH20 treatment did not significantly change G_d, G_l, or |G*| in 4T1 or 4T1/HAS3 tumours (ns; $p>0.05$, unpaired Student's t-test). PEGPH20 significantly increased G_d (*p=0.02), G_l (*p=0.02) and |G*| (*p=0.02) in MDA-MB231 LM2-4 tumours. No significant change in Y was seen in any of the breast tumour models (ns; $p>0.05$). Data points are median values from each individual tumour and are summarised by the cohort mean ± 1 SEM.

Figure 4.8: Collagen content (%), fractal dimension, and entropy quantified from picrosirius red stained 4T1, 4T1/HAS3 and MDA-MB-231 LM2-4 tumour sections. The graph of collagen content is also shown in Chapter 3 (Figure 3.11). Significant differences between saline controls, and between saline and PEGPH20 treated tumours within the same tumour model are shown (one-way ANOVA; *p<0.05, **p<0.01, ***p<0.001, ****p<0.0001).

Chapter 5

Figure 5.1: Anatomical T_2-weighted (T_2w) MRI and parameter maps of R_2*, generated using IS-MRI, for a representative 4T1, 4T1/HAS3 and MDA-MB-231 LM2-4 tumour prior to and 24 hours after saline. The tumour ROI from which necrosis was excluded is shown by a white dashed line.

Figure 5.2: Anatomical T_2-weighted (T_2w) MRI and parameter maps of R_2*, generated using IS-MRI, for a representative 4T1, 4T1/HAS3 and MDA-MB-231 LM2-4 tumour prior to and 24 hours after PEGPH20 treatment (1 mg/kg). The tumour ROI from which necrosis was excluded is shown by a white dashed line.

Figure 5.3: Median R_2* for 4T1, 4T1/HAS3 and MDA-MB-231 LM2-4 tumours pre-saline, post-saline, pre-PEGPH20 and post-PEGPH20. Data from each individual tumour are plotted, with saline controls in blue and PEGPH20 treated tumours in red. Sample sizes for 4T1, 4T1/HAS3 and MDA-MB-231 LM2-4 tumours were: n = 6 saline and n = 5 PEGPH20; n = 6 saline and n = 6 PEGPH20; and n = 11 saline and n = 12 PEGPH20 respectively.

Figure 5.4: Percentage change in R_2* between pre- and post-treatment MRI for saline and PEGPH20 treated mice bearing 4T1, 4T1/HAS3 or MDA-MB-231 LM2-4 tumours. PEGPH20 treatment did not significantly change R_2* in 4T1 or MDA-MB-231 LM2-4 tumours (ns; $p>0.05$, unpaired Student's t-test). PEGPH20 increased R_2* (**$p=0.003$) in 4T1/HAS3 tumours. Data points are percentage differences (post minus pre) of median values from each individual tumour and are summarised by the cohort mean ± 1 SEM.

Figure 5.5: T_2-weighted (T_2w) MRI alongside representative aligned 4T1, 4T1/HAS3 and MDA-MB-231 LM2-4 tumour tissue sections (5 μm) stained for CD31 (blood vessels). Representative magnified images (20x) are presented alongside whole tumour section images for one saline control and one PEGPH20 treated tumour per tumour model.

Figure 5.6: Blood vessel density (number per mm^2 tumour tissue) quantified from CD31 stained 4T1, 4T1/HAS3 and MDA-MB-231 LM2-4 tumour tissue sections. Blood vessel density was highest in 4T1/HAS3 tumours, followed by 4T1 tumours, and lowest in MDA-MB-231 LM2-4 tumours (one-way ANOVA with multiple comparisons; ****$p<0.0001$). PEGPH20 treated tumours had similar blood vessel density to saline controls in all three tumour models ($p>0.05$).

Chapter 6

Figure 6.1: Representative MRI and matched histology images (whole section and 10x magnification images) from a representative MDA-MB-231 LM2-4 tumour post-treatment with saline. Necrosis, which was excluded from quantitative analyses, is indicated by a white dashed line. MRI-aligned tumour tissue sections were stained using H&E (morphology), HTI-601 (HA), picrosirius red (collagen I & III), and CD31 (blood vessels).

Figure 6.2: Correlation matrices of MRI biomarkers and matched histological staining. The correlation matrices show Pearson's correlation coefficient (r) for each pairing. Relationships were evaluated with all data pooled together **(A)**, and with saline **(B)** and PEGPH20 treated **(C)** tumour data kept separate. Nuclear density, percentage HA, percentage collagen (I & III), and vessel density were calculated from H&E, HTI-601, picrosirius red, and CD31 staining respectively.

Negligible levels of HA (< 2%) were detectable in the PEGPH20 treated tumours, hence percent HA was excluded from the correlation analysis in this group (crossed-out squares). For blank squares r < 0.01.

Figure 6.3: Sample sizes (blue) and p-values (red) for the correlation matrices of MRI biomarkers (T_1, T_2, MTR, ADC, R_2*, G_d, G_l, |G*|, and Y) and matched histological staining shown in Figure 6.2. Relationships were evaluated with all data pooled together **(A)**, and with saline **(B)** and PEGPH20 treated **(C)** tumour data kept separate. Significant p-values are shown in bold ($p < 0.05$).

Figure 6.4: Correlations between MRI biomarkers in saline (HA present) and PEGPH20 treated (HA degraded) 4T1, 4T1/HAS3, and MDA-MB-231 LM2-4 breast tumours. Saline control and PEGPH20 treated tumour data are shown in blue and red respectively, with different shaped symbols indicating the different breast tumour models. The sample size (n), Pearson's correlation coefficient (r), and p-value are shown by the linear regression they relate to.

Figure 6.5: Correlations between MRI biomarkers and nuclear density (quantified from H&E staining) in saline (HA present) and PEGPH20 treated (HA degraded) 4T1, 4T1/HAS3, and MDA-MB-231 LM2-4 breast tumours. Saline control and PEGPH20 treated tumour data are shown in blue and red respectively, with different shaped symbols indicating the different breast tumour models. The sample size (n), Pearson's correlation coefficient (r), and p-value are shown by the linear regression they relate to.

Figure 6.6: Correlations between MRI biomarkers and percent HA (quantified from HTI-601 staining) in saline (HA present) and PEGPH20 treated (HA degraded) 4T1, 4T1/HAS3, and MDA-MB-231 LM2-4 breast tumours. Saline control and PEGPH20 treated tumour data are shown in blue and red respectively, with different shaped symbols indicating the different breast tumour models. The sample size (n), Pearson's correlation coefficient (r), and p-value are shown by the linear regression they relate to.

Figure 6.7: A HTI-601 (HA) stained section **(A)** alongside matched parametric maps of T_2 **(B)**, MTR **(C)**, and ADC **(D)** for one saline control 4T1 tumour with representative intra-tumour heterogeneity in HA accumulation for this model. Spatial associations between T_2, ADC, and HA were apparent, with areas of high

HA accumulation corresponding to areas of high T_2 and ADC (green arrows) and regions of low HA related to areas of low T_2 and ADC (blue arrows). Some regions of the T_2 map appeared unrelated to HA accumulation (yellow arrow). Tumour areas with high HA accumulation did not correspond to low MTR as suggested by the inter-tumour correlation in Figure 6.6. An artefact on the T_2 map was excluded from analyses (red dashed ROI).

Figure 6.8: Correlations between MRI biomarkers and collagen content (quantified from picrosirius red staining) in saline (HA present) and PEGPH20 treated (HA degraded) 4T1, 4T1/HAS3, and MDA-MB-231 LM2-4 breast tumours. Saline control and PEGPH20 treated tumour data are shown in blue and red respectively, with different shaped symbols indicating the different breast tumour models. The sample size (n), Pearson's correlation coefficient (r), and p-value are shown by the linear regression they relate to.

Figure 6.9: Correlations between MRI biomarkers and blood vessel density (quantified from CD31 staining) in saline (HA present) and PEGPH20 treated (HA degraded) 4T1, 4T1/HAS3, and MDA-MB-231 LM2-4 breast tumours. Saline control and PEGPH20 treated tumour data are shown in blue and red respectively, with different shaped symbols indicating the different breast tumour models. The sample size (n), Pearson's correlation coefficient (r), and p-value are shown by the linear regression they relate to.

Figure 6.10: A simplified graphic summarising the hypothesised explanation for the different characteristics of pre-clinical breast tumours treated with either saline (HA present; blue) or PEGPH20 (HA degraded; red). ADC = the apparent diffusion coefficient. IFP = interstitial fluid pressure. ECM = extracellular matrix.

Abbreviations List

$\|G^*\|$	Absolute value of the complex shear modulus
ω_0	Larmor frequency
^1H	Hydrogen proton
ADC	Apparent diffusion coefficient
ARRIVE	Animal research: reporting *in vivo* experiments
AT1R	Angiotensin receptor type 1
ATP	Adenosine triphosphate
BAX	Bcl-2-associated X protein
BLI	Bioluminescence imaging
BOLD	Blood oxygen level dependent
CAF	Cancer associated fibroblast
CE	Contrast enhanced
CEST	Chemical saturation transfer
COX-2	Cyclooxygenase-2
CTGF	Connective tissue growth factor
CV_{WS}	Within-subject test-retest coefficient of variation
DT	Doubling time
DWI	Diffusion weighted imaging
ECM	Extracellular matrix
EGFR	Epidermal growth factor receptor
EMT	Epithelial to mesenchymal transition
FAK	Focal adhesion kinase
FBS	Foetal bovine serum
FFPE	Formalin fixed paraffin embedded
FLT	^{18}F-Fluorothymidine
GAG	Glycosaminoglycan
GBCA	Gadolinium-based contrast agent
G_d	Elastic modulus
GEM	Genetically engineered mouse
G_l	Viscous modulus
GLUT	Glucose transporter
GPI	Glycosylphosphatidylinositol

H&E	Haematoxylin & eosin
HA	Hyaluronan
HABP	HA binding protein
HAS	HA synthase
HCC	Hepatocellular carcinoma
HMW	High molecular weight
HTI-601	TSG-6 based HA binding probe
IFP	Interstitial fluid pressure
K^{trans}	Volume transfer constant
LAIR	Leucocyte associated immunoglobulin like receptor
LMW	Low molecular weight
LOX	Lysyl oxidase
MAPK	Mitogen-activated protein kinase
MD	Mammographic density
MGE	Multiple gradient echo
MMP	Matrix metalloprotease
MRE	Magnetic resonance elastography
MRI	Magnetic resonance imaging
MT	Magnetisation transfer
MTR	MT ratio
OE	Oxygen enhanced
OS	Overall survival
$p0^2$	Partial pressure of oxygen
PDAC	Pancreatic ductal adenocarcinoma
PDX	Patient derived xenograft
PEGPH20	Pegvorhyaluronidase alfa
PET	Positron emission tomography
PI3K	Phosphoinositide-3-kinase
PTEN	Phosphatase and tensin homolog
PTFE	Polytetrafluoroethylene
r	Pearson's correlation coefficient
R_2*	Transverse relaxation rate
RARE	Rapid acquisition with refocussed echoes
RB	Retinoblastoma

RBC	Red blood cell
RF	Radiofrequency
RHAMM	Receptor for HA mediated motility
ROCK	Rho-associated protein kinase
ROI	Region of interest
SC	Susceptibility contrast
SEM	Standard error of the mean
SHH	Sonic hedgehog
SPECT	Single photon emission computed tomography
SS	Solid stress
STR	Short tandem repeat
T_1	Longitudinal relaxation time
T_2	Transverse relaxation time
TACS	Tumour associated collagen signature
TGF-β	Transforming growth factor β
TME	Tumour microenvironment
TSG-6	Tumour necrosis factor stimulated gene 6
TTP	Total tissue pressure
US	Ultrasound
USPIO	Ultrasmall superparamagnetic iron oxide
Y	Normalised phase angle

Chapter 1: Introduction

1.1 Breast cancer

Breast cancer is the most common cancer in the UK and the leading malignancy in women worldwide. It is most prevalent in well-developed countries[1]. The 10-year survival rate has doubled over the last 40 years and stands at 78%; however, this disease remains the 3rd largest contributor to cancer related deaths.

Breast cancer often arises in the mammary gland, a dense region of tissue which contains extensive extracellular matrix (ECM) in the form of basement membrane and interstitial ECM[2, 3]. Basement membrane disruption and stiffening of the interstitial ECM can facilitate tumour development and progression[4, 5]. Tissue density on mammogram, which suggests increased cellularity and collagen deposition, increases breast cancer susceptibility 2 to 6-fold and may predict disease recurrence (Figure 1.1)[3, 6, 7]. Palpation is an important clinical tool for diagnosis of breast tumours as they are often stiffer than the surrounding normal tissue. Primary breast tumours with high metastatic ability are often characterised by accumulation of fibrillary collagens, fibronectin, laminins, proteoglycans and hyaluronan (HA or hyaluronic acid)[2].

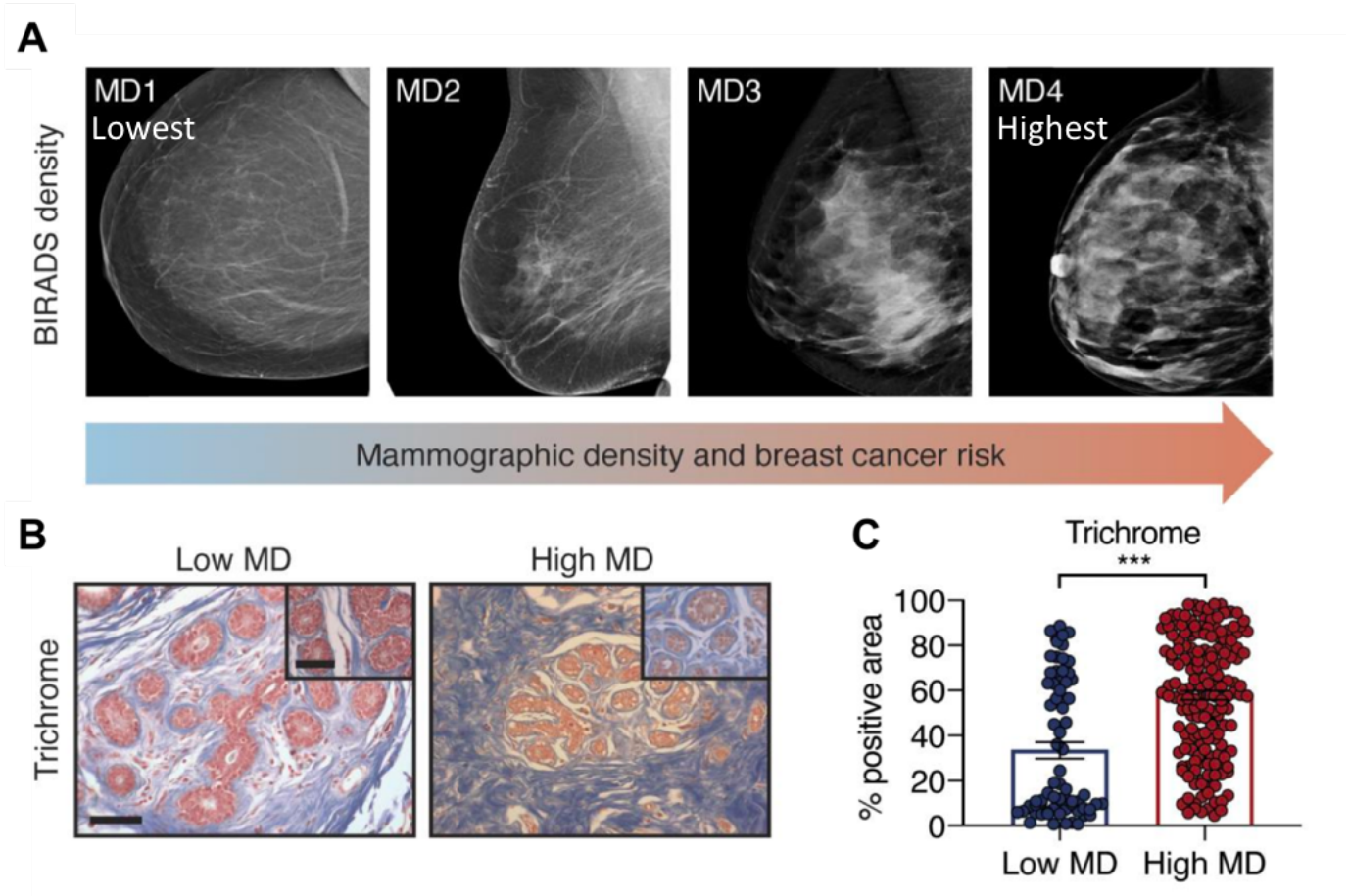

Figure 1.1: (A) *Increased mammographic density (MD) of breast tissue is associated with a higher risk of breast cancer.* ***(B & C)*** *High MD is linked to elevated collagen deposition, quantified by Masson's trichrome staining (blue). Images from [7]. Scale bar: 100μm and 50μm (insert).*

1.1.1 In vivo modelling of stromal-dense tumours

Tumour stiffness and ECM composition are not characteristics of malignant cells in isolation but the tumour mass as a whole. Thus, *in vitro* approaches to assess stromal-dense tumours including breast are limited. Animal models of stromal-dense tumours often provide greater insight. Systematic use of these models must be supported by evidence that the tumour development, progression and radiology recapitulate the human disease. Typically, orthotopic (cancer cells injected or implanted into the organ from which the cancer originated), genetically engineered mouse (GEM) and patient derived xenograft (PDX) models better represent the stromal composition, vasculature and metastatic potential of human disease compared to ectopic (subcutaneous) tumours.

1.2 The ECM

The ECM is a key functional regulator present to different degrees within all body tissues[8]. It is composed on an extremely interconnected web of macromolecules including collagens, proteins, polysaccharides, glycoproteins (e.g. fibronectin and laminin), proteoglycans (e.g. heparan sulphate), glycosaminoglycans (GAGs; e.g. HA), and integrins. Differing amounts of these macromolecules provide unique biochemical, biophysical and structural support to different normal tissues and pathologies[9, 10]. The interstitial ECM is rich in fibrillar collagens, proteoglycans, tenascin C and fibronectin. It is highly charged, hydrated and contributes hugely to the tensile strength of tissues[9]. Basement membranes are made up of type IV collagen, laminins, fibronectin and linker proteins. These membranes are compact and less porous compared to interstitial matrix.

The ECM provides mechanical strength and is highly resistant to alterations in tension. In addition, the ECM can sequester molecules, such as growth factors, control their release and establish chemical gradients[10]. A summary of the roles of the ECM is shown in Figure 1.2.

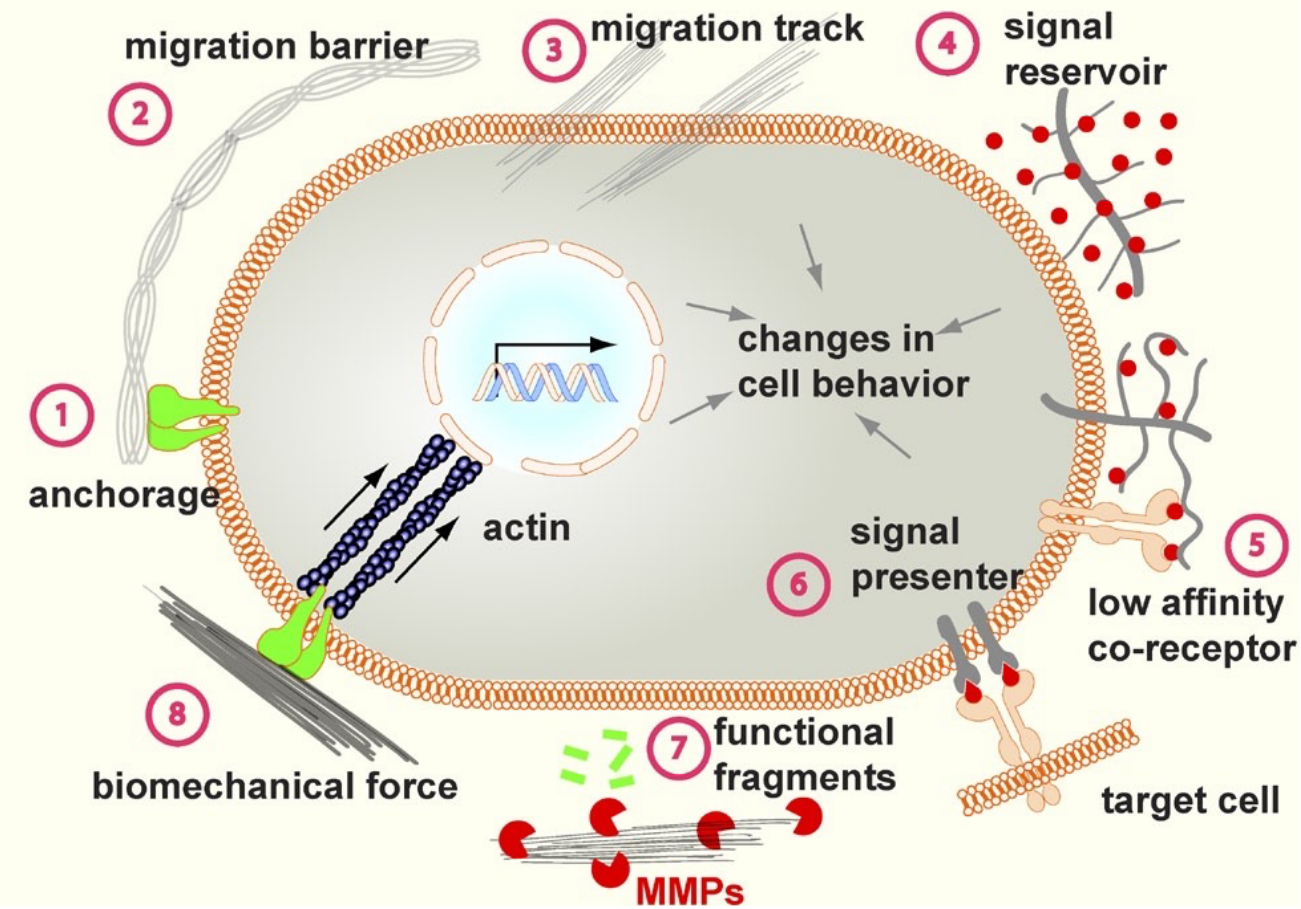

Figure 1.2: *Functions of the extracellular matrix (ECM), taken from [10].*

In healthy tissue, the synthesis of ECM components is tightly controlled, and regions of abnormal ECM are detected and rectified by local fibroblasts[9, 11]. However, in cancer aberrant ECM production, degradation and remodelling persists without correction (Figure 1.3)[10, 12]. A dense tumour-associated ECM, primarily produced and remodelled by cancer associated fibroblasts (CAFs), is associated with poor patient prognosis[12]. ECM density drives tumour progression, contributes to high interstitial fluid pressure (IFP) and vascular collapse, and acts as a barrier to perfusion, diffusion, immune infiltration and drug delivery[13-15]. Remodelling occurs primarily through increased collagen crosslinking and reorientation[16]. More than 80% of cancers are derived from epithelial tissues, termed carcinomas, and contain a basement membrane which must be breached during cancer cell invasion[8, 17]. Metastasis is the leading cause of cancer-related mortality, and so understanding how ECM modification influences this would be of huge benefit.

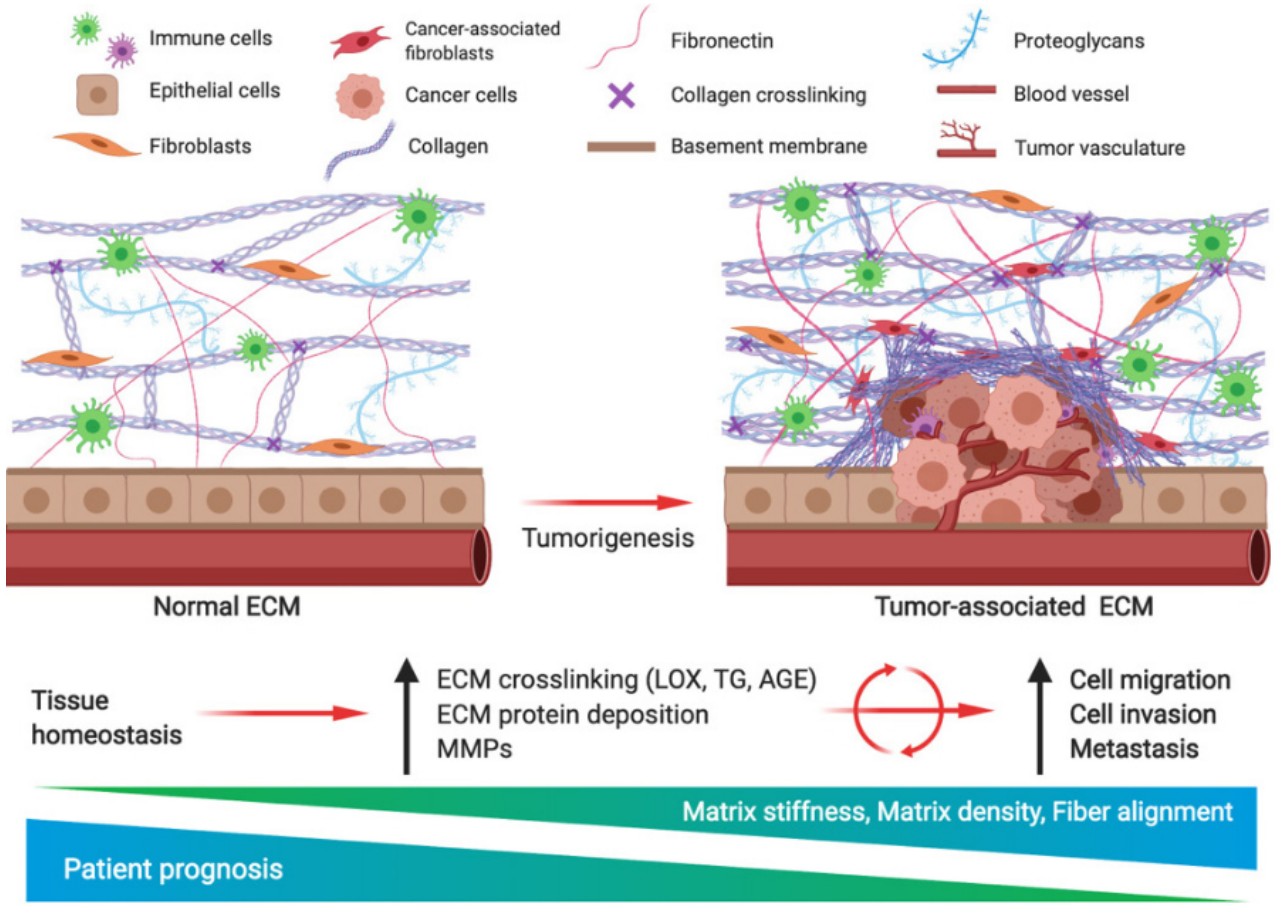

Figure 1.3: *The altered microenvironment of tumours. Accumulation of ECM components can drive malignancy, act as a barrier to drug delivery, and is associated with poor patient prognosis. Image from [12].*

1.2.1 The ECM influences the hallmarks of cancer

The rapidly evolving tumour-associated ECM can influence the hallmarks of cancer (Figure 1.4)[18]. The eight hallmarks of cancer, highlighted by Hanahan & Weinberg, are the ability of cancer cells to sustain proliferative signalling; evade growth suppressors; resist cell death; enable replicative immortality; induce angiogenesis; activate invasion and metastasis; reprogram energy metabolism and evade immune destruction[19].

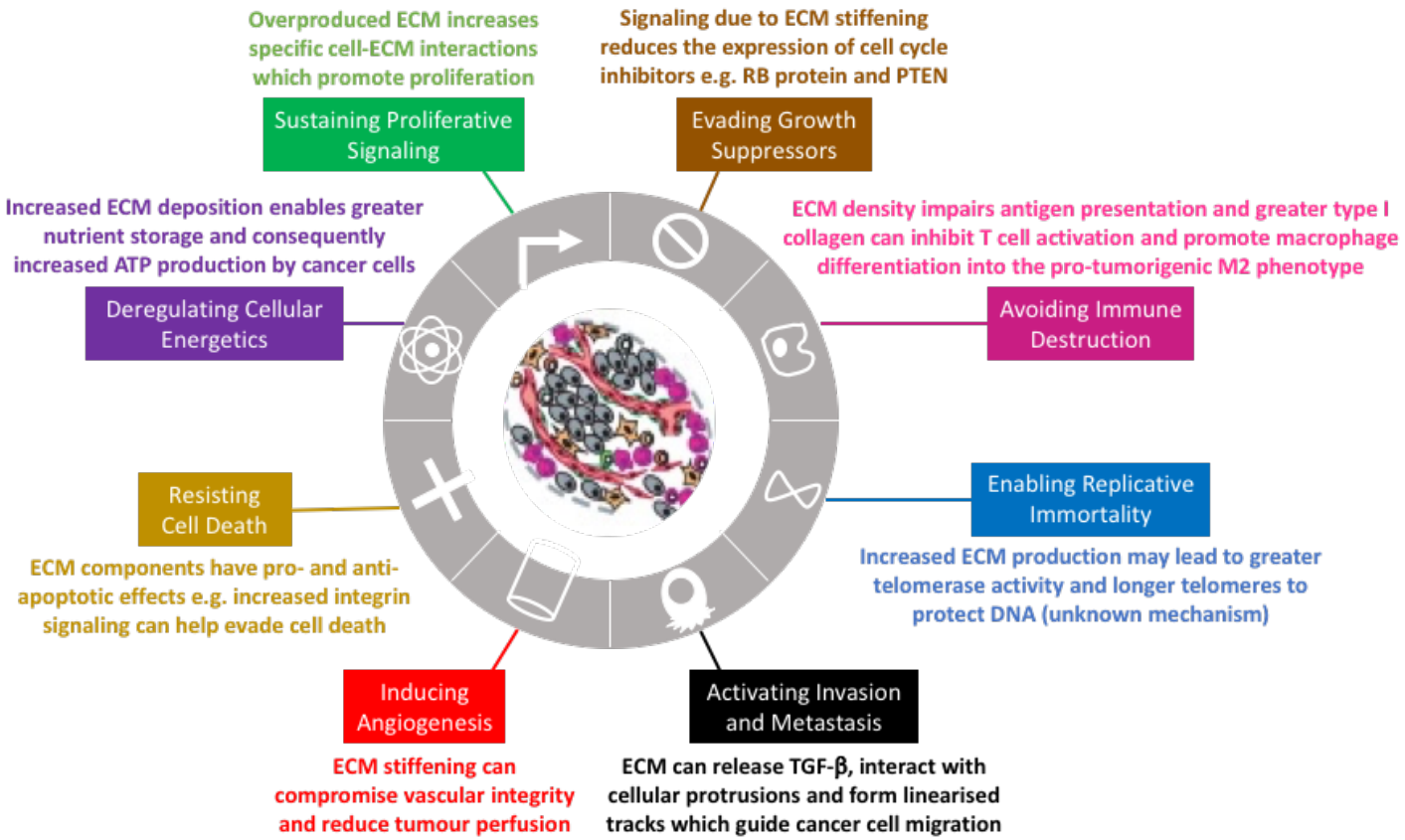

Figure 1.4: *The influence of the extracellular matrix (ECM) on the hallmarks of cancer. Eight hallmarks are highlighted in different coloured boxes and the ECM impact is noted in the same colour beside each box. N.B. this is a general summary and is not applicable to all cancer types. Image created using [18, 19].*

Tumour cell proliferation is increased in regions of elevated ECM due to greater cell-ECM interactions. Firstly, some ECM components, such as heparan sulfate proteoglycans, act as co-receptors in growth factor signalling. Secondly, increased integrin signalling, through upregulated collagen or ECM stiffness, promotes focal adhesion kinase (FAK) phosphorylation, and stimulation of intracellular signalling cascades, including mitogen-activated protein kinase (MAPK) and phosphoinositide-3-kinase (PI3K), which promote cell cycle acceleration through the G1/S checkpoint[10, 18, 20, 21]. Furthermore, a stiffened ECM reduces the expression of cell cycle inhibitors such as retinoblastoma (RB) protein and PTEN (phosphatase and tensin homolog)[18].

ECM components or their functional fragment derivatives can have pro- or anti-apoptotic effects. Most normal cells require ECM adhesion for survival[22]. Accumulation of ECM components can assist cancer cell evasion of apoptosis through increased focal adhesions and upregulation of integrin signalling which results in downstream inactivation of pro-apoptotic molecules such as Bcl-2-associated X protein (BAX)[18, 23].

The mechanism of replicative immortality is not fully understood but evaluation of pulmonary fibrosis suggests that elevated ECM deposition and tissue stiffening leads to increased telomerase activity and longer telomeres[18, 24]. Telomeres are normally shortened over-time through repeated cell division and their preservation in fast growing cells will protect from DNA damage and cell death.

The ECM plays a dual role in angiogenesis because it acts as a reservoir for both pro- and anti-angiogenic factors[18]. More specifically, a dense and stiff ECM in an environment of increased cellularity can compromise vascular integrity and reduce perfusion into the tumour microenvironment (TME), resulting in regions of hypoxia and increased IFP[25]. Conversely, overexpression of ECM remodelling enzymes, for example matrix metalloproteases (MMPs), can increase angiogenesis[10, 26].

Uncontrolled ECM production and maintenance can activate tumour cell invasion and metastasis. Cell movement requires ECM adhesion, and linearisation can create tracks used by migratory cells[27]. The ECM can also sequester and release transforming growth factor β (TGF-β) and induce epithelial-to-mesenchymal transition (EMT); a process used by cancer cells to increase their migration and metastatic potential[18]. Experimental reduction of interstitial ECM stiffness, for example through inhibition of collagen crosslinking, can prevent metastasis[28, 29]. However, degradation of ECM components in the basement membrane can also increase tumour cell invasion[10, 26].

ECM nutrient storage is crucial for cellular production of adenosine triphosphate (ATP), the energy source required by all living cells. Through the Warburg effect, tumour cells typically respire through the less efficient mechanism of anaerobic glycolysis. This strategy reduces the need for oxygen, reducing competition with adjacent healthy cells and enabling survival in hypoxic conditions[30]. Anaerobic glycolysis produces two ATP from each glucose molecule compared to oxidative phosphorylation which yields over thirty. As well as providing nutrients, the ECM can bind cancer cells and cause upregulation of glucose transporter (GLUT) 1 and GLUT4 at the tumour cell surface which increases glucose influx and ATP production enough for tumour cells to continue growing and bypass a starvation phenotype[18, 30].

ECM migratory tracks and chemo-attractant gradients can encourage or discourage immune cell infiltration into the TME. Once inside, ECM components can directly modify the proliferation and activation status of T cells; for example, type I collagen can inhibit T cell proliferation via ligation to leucocyte associated immunoglobulin like receptors (LAIRs). Moreover, the ECM can physically impair antigen presentation, and a collagen-rich ECM can promote macrophage activation, proliferation and differentiation into the pro-tumorigenic M2 phenotype[18]. Degradation of collagen with collagenase can increase immune-cancer cell interactions[31].

1.2.2 The ECM influences cancer treatment responses and disease recurrence

The tumour-associated ECM can reduce therapeutic responses through hypoxia and physical obstruction of drug delivery. Hypoxia is common in solid tumours and provides resistance to treatments including radiation, chemotherapy, and immunotherapy[32-34]. ECM density within the TME reduces perfusion, leaving many tumour cells more than 100μm away from the nearest blood vessel[25, 35]. Following release from the blood, drug molecules moving through the tumour mass can be slowed by dense ECM and, as a result, drug concentrations in tumour regions distant from blood vessels are likely to be lower than the efficacious dose[25]. Physical barriers to drug delivery must be considered alongside molecular mechanisms when evaluating drug resistance[36].

Degradation of ECM components, such as collagen and HA, can significantly improve interstitial transport of drug molecules in dense treatment-resistant tumours[14, 35, 37, 38]. However, some ECM components are not suitable therapeutic targets. For example, fibronectin can promote EMT but physiological levels are low and the upregulation seen in breast tumours is small, transient and cannot be measured effectively[2].

1.2.3 The role of collagen in cancer

There are 28 types of collagen, both fibrillar and non-fibrillar forms, which account for approximately 30% of the protein mass in the human body[2]. Type I collagen is fibrillary and a principal component of the interstitial matrix whilst type VI collagen is non-fibrillar and is a key constituent of basement membranes[9]. In stromal-dense cancers, increased levels of type I, III and V collagens confer stiffness and increased pressure within the interstitial matrix, whilst decreased type IV collagen in the basement membrane facilitates invasion and metastasis[2, 39, 40]. A uniform and random distribution of type I collagen is apparent in smaller tumours

(diameter ~2mm) but a highly organised and linear network has been noted at the periphery of larger tumours (diameter ~7mm)[41].

Long, linearized and crosslinked collagen fibres in the tumour-associated ECM contribute to tumour desmoplasia which has been linked to reduced survival in patients and mouse models[9, 42]. Evaluation of tumour associated collagen signatures (TACS1-3) may predict breast cancer survival. The highest phenotype (TACS3) is associated with the poorest patient survival and describes collagen fibres which have been bundled, reoriented and aligned perpendicular to the tumour mass[3, 43]. Picrosirius red or Masson's trichrome staining of formalin fixed paraffin embedded (FFPE) tissue sections is commonly used to detect expression of collagen type I and III; polarized light microscopy can further analyse the picrosirius red stain and may provide information on collagen fibre structure[44]. Collagen content in pre-clinical tumour models positively correlates with tumour stiffness which in turn is associated with metastatic propensity[45, 46].

1.2.4 The role of HA in cancer

Approximately 25-30% of human tumours overexpress HA; a simple, linear, non-sulphated GAG[47-49]. These include pancreatic, breast, prostate, bladder, and gastric cancers[14, 47]. Many cells can synthesise HA but, under healthy conditions, it is predominantly produced by HA synthases (HAS1-3) on the surface of mesenchymal cells. HA polymer expression is tightly controlled by hyaluronidase-mediated cleavage (HYAL1-4, PH20 and HYALP1), endocytic uptake, and scavenger-mediated removal from the blood stream[50-52]. Optimum length and expression of HA during each stage of tumour development is likely to result from variable expression of different HAS and hyaluronidase isoforms, and maintenance of scavengers[52, 53].

HA consists of up to 25,000 repeating disaccharide subunits of glucuronic acid and N-acetylglucosamine[47]. The repeating sequence is

homogeneous across all vertebrate species, but polymer length varies[54]. HA polymer size is important. HA is commonly synthesised as a high-molecular weight (HMW) polymer (~1000 - 8000 kDa) which absorbs water, swells and presses against surrounding cells and structural elements of the tissue increasing pressure within the tumour mass[54]. In contrast, low molecular weight (LMW) HA is thought to play a greater role in cell signalling[2, 55, 56].

HA is negatively charged and has high colloid osmotic pressure which enables coordination of up to three water molecules per disaccharide unit[51, 57]. This hygroscopicity provides elasticity, lubrication, and enables HA to fill the extracellular space. Many hydrophilic proteoglycans bind HA polymers, making a viscoelastic gel-like matrix which supports cells and insoluble collagen fibres[14]. Elevated HA can increase IFP, promote metastasis, reduce treatment efficacy, and decrease overall survival[47, 58-61]. TGFβ, a key promoter of tumour progression, stimulates HA synthesis through HAS2 upregulation[62].

HA-induced intracellular signalling is commonly mediated by cell surface receptors CD44 and RHAMM (receptor for HA mediated motility)[63]. CD44 and RHAMM activity is inhibited by the tumour suppressor p53 and CD44 is a marker of cancer stem cells[64-66]. In the clinic, increased expression of HA and its receptors are prognostic for poor outcome and disease recurrence in various tumour types including breast cancer[64, 67, 68].

1.2.4.1 Experimental detection of HA

Due to its simple structure and ubiquitous expression across all vertebrates, HA is not immunogenic and histological detection using antibodies is not possible[69]. Probes designed from regions of HA-binding proteins (HABPs or hyaladhesins) are currently used to evaluate HA accumulation. Probes include cartilage derived HABP, PEP-1 synthetic peptide, recombinant versican G1 domain, and a modified tumour necrosis factor-stimulated gene 6 (TSG-6)[70]. One caveat is that HA polymers

already bound to numerous proteins may be underreported when using HABPs for detection[69].

Commercially available cartilage derived HABP is not suitable for a clinical companion diagnostic assay because it requires both HA-protein and protein-protein interactions for HA detection and cannot obtain accurate quantitative binding constants. In addition, these preparations have low purity and batch-to-batch variability[70].

The TSG-6 probe (HTI-601, Halozyme Therapeutics) was developed using a small HA binding link module with well-defined structure and relatively high HA-binding affinity. It contains an inactivated heparin binding domain and the addition of a human IgG1 Fc region enhances probe purification and detection (Figure 1.5)[70]. Five repeating disaccharide units (2 kDa) is the minimum HA oligosaccharide length detected with this probe. The heparin binding domain is mutated, lysine to alanine, at three sites to reduce heparin binding activity, minimising cross reactivity and increasing HA specificity. Like many other probes, biotin can be added to improve detection. The TSG-6 probe is sensitive to pharmacological modulation of HA, and exhibited greater sensitivity compared to cartilage derived HABP, with 5-fold less TSG-6 probe required[70].

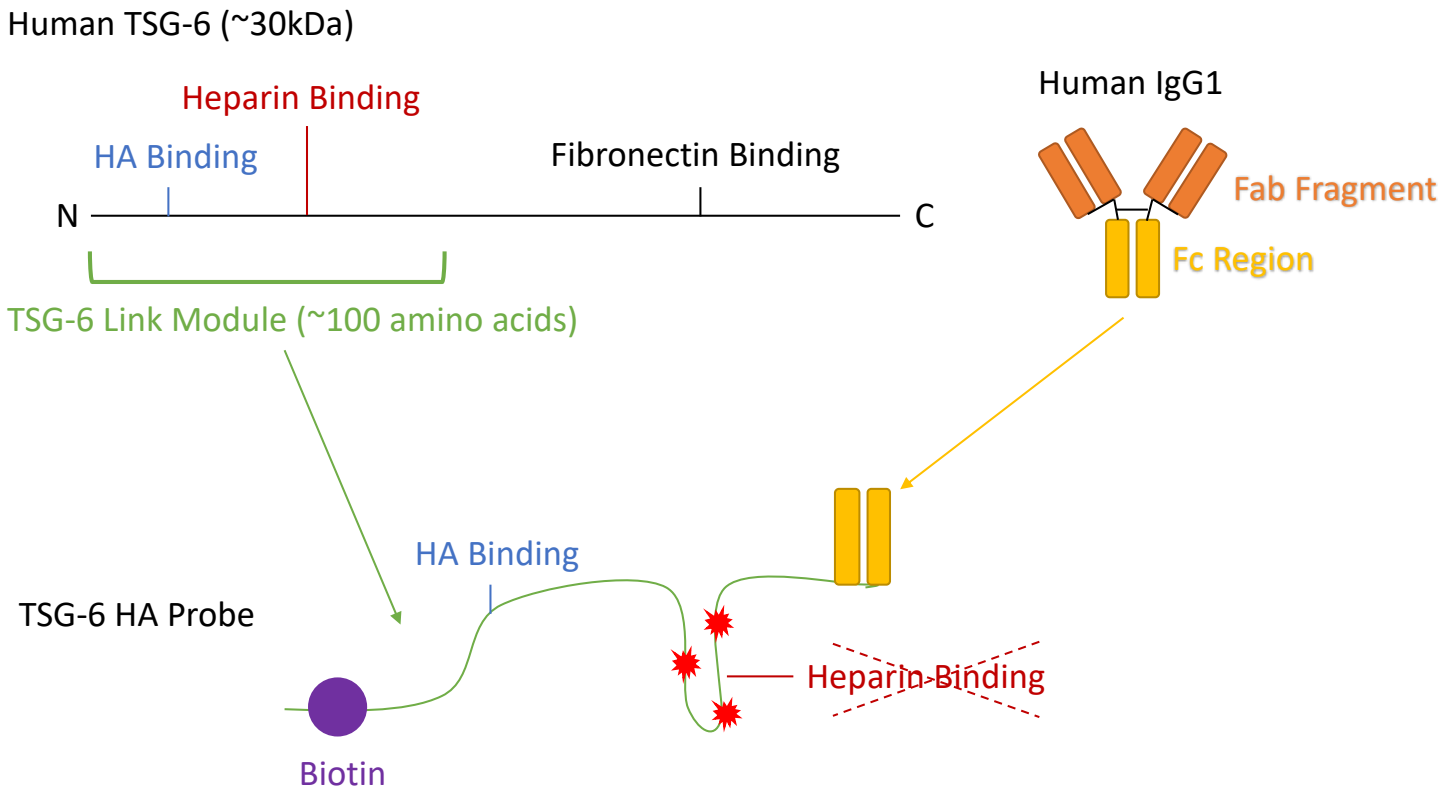

Figure 1.5: *Graphical representation of the modified TSG-6 probe (HTI-601) used for HA detection. Information from [70]. Red stars represent three lysine to alanine mutations which decrease heparin binding activity by 90%.*

1.3 Mechanical forces within the TME

Generally, an aberrant tumour-associated ECM is associated with altered tissue viscoelasticity and amplification of local forces, such as IFP and solid stress, which have been linked to poor patient prognosis (Figure 1.6)[71, 72].

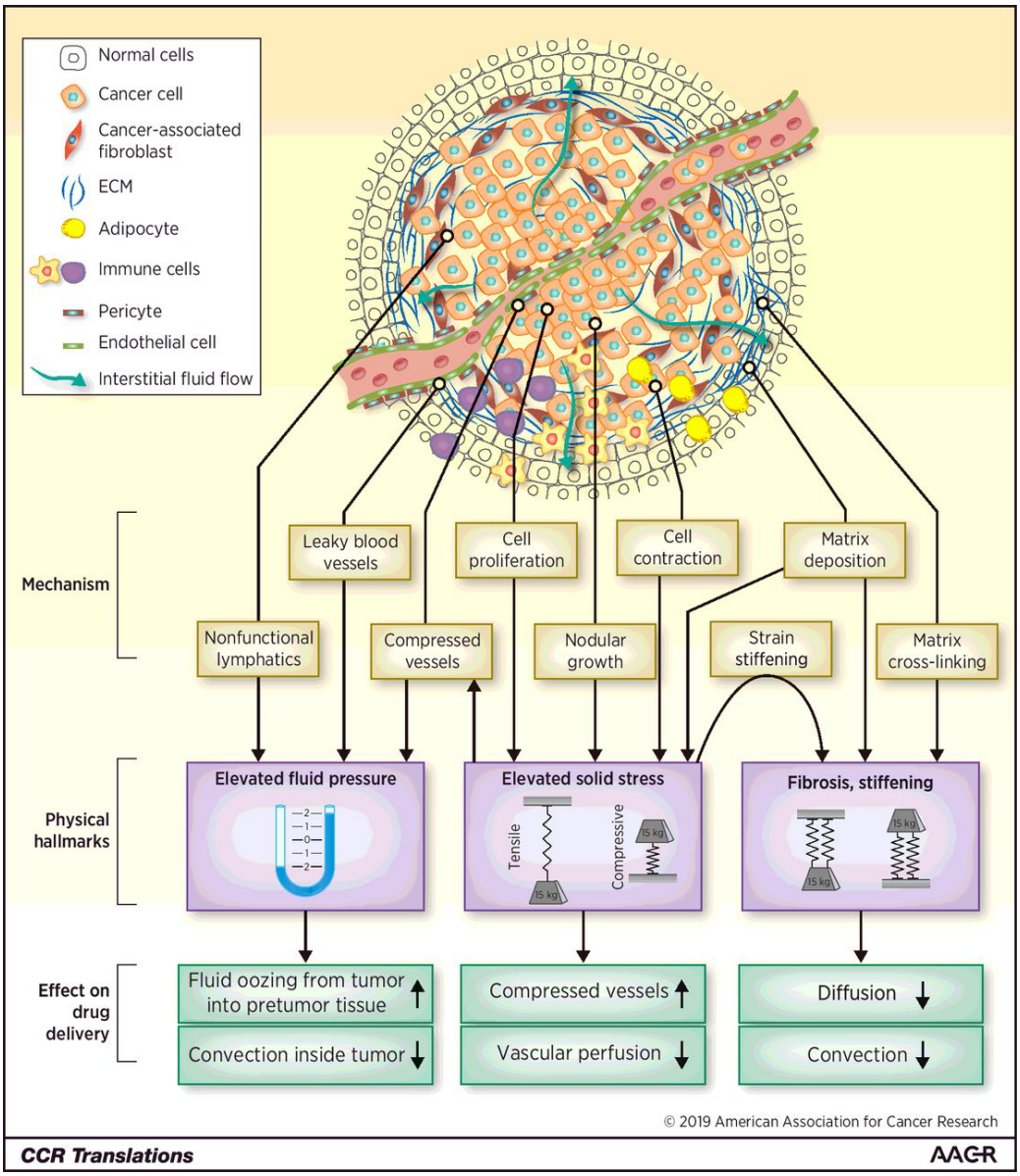

Figure 1.6: *The physical microenvironment of tumours. Elevated interstitial fluid pressure (IFP), solid stress, and stiffness are the three major features of the tumour physical microenvironment and all hinder drug delivery. Image from [72].*

1.3.1 Viscoelastic properties

Most biological tissues exhibit both viscous and elastic properties. Viscosity is defined as a resistance to flow which leads to a frictional loss of energy as heat, whilst elasticity is the ability of a material to store energy and resume its normal shape following deformation[73-75]. Using viscous and elastic moduli, tissue stiffness can be calculated which is defined as the extent an object can resist deformation in response to an applied force.

Solid tumours are often markedly stiffer than the surrounding healthy tissue, and this elevated stiffness can promote cancer growth, invasion and metastasis[11, 71, 76-80]. Computational modelling suggests that solid tumour stiffness, with some exceptions, must be greater than 1.5 times the stiffness of surrounding healthy tissue in order for a tumour mass to expand[81]. Local tissue rigidity can alter cell differentiation and promote a more aggressive phenotype[82]. Many brain tumours, evaluated pre-clinically and clinically, are unusual as, unlike other solid tumours, they are inherently soft[83].

Often only a small percentage of the tumour is made up of malignant cells. Tumour stiffness is thus largely the result of stromal cell proliferation and synthesis of a dense ECM[84]. Necrotic regions of solid tumours add further complexity, commonly contributing to tumour softness[85]. The stiffness of cancer cell lines and patient tumour cells inversely correlates with invasion and migration[84]; soft and deformable cancer cells located within a stiff TME have a higher metastatic potential. The increasing compressive and tensile stresses in the local environment encourage malignant cells located at the tumour periphery to migrate through a weakened area of basement membrane[86]. A graphical summary of this phenomena is shown in Figure 1.7. Physical deformation of a cancer cell nucleus during invasion is associated with increased DNA damage and mutational load which can further promote an aggressive phenotype[11, 87]. Migration is initiated by a few leading cells which are deformable, extend filopodia and bind to a fibronectin-enriched type-IV-collagen-depleted matrix[88].

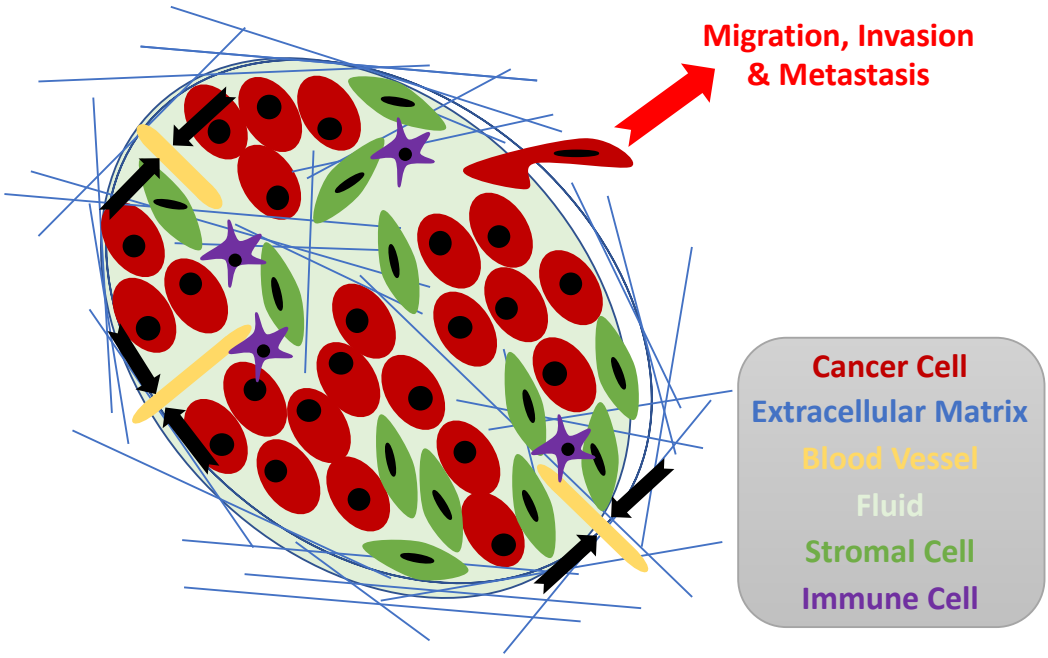

Figure 1.7: *Graphical representation of a soft and deformable cancer cell migrating out of a highly pressurised and stiff tumour microenvironment (TME). Black arrows represent pressure which compresses blood vessels in the TME.*

1.3.2 Solid stress

Solid stress is a compressive or tensile force exerted by non-fluid tissue components. Solid stress increases with tumour progression, likely a result of uncontrolled exponential cell proliferation and mechanical confinement by surrounding healthy tissue[40, 41]. Solid stress can vary depending on tumour size, tumour type and the properties of surrounding stroma[16, 41]. Solid stresses are contained within and transmitted by solid and elastic structural components, such as the ECM and cells[40, 41]. This is distinct from IFP which refers to fluids, but solid stress and IFP may be linked; for example, increased solid stress can compress blood and lymphatic vessels, reduce perfusion and contribute to hypoxia, the development of a necrotic core, and increase IFP[16, 89]. Insufficient blood and lymphatic flow results in non-uniform penetration of oxygen, drugs, and immune cells into the tumour mass. Poor blood flow and hypoxia have been linked to immunosuppression, inflammation, invasion, metastasis, and reduced efficacy of chemotherapy, radiotherapy and immunotherapy[90].

1.3.3 IFP

IFP is a hydrostatic pressure encompassing pressure from free fluid and HA-immobilised fluid[16]. Solid tumours typically have elevated IFP (~4 to 60 mmHg) compared to adjacent normal tissues (~0 mmHg) due to hyperpermeable, leaky blood vessels and lack of draining lymphatic vessels to remove plasma molecules and free fluid from the local environment[11, 40, 91]. Aberrant tumour ECM composition and elasticity have also been linked to increased IFP[91, 92]. Tumour IFP is fairly constant throughout the tumour core but may drop precipitously at the periphery[92, 93].

Clinically, high tumour IFP is associated with a high recurrence rate and poor patient prognosis[92, 94]. IFP can surpass microvascular pressure and surrounding fluid pressures which compresses blood vessels and promotes fluid release from the tumour mass[11, 40, 95]. Fluid release encourages drug and cancer cell exit from the tumour mass; reducing drug delivery and facilitating metastasis. Cancer cells may follow distorted chemical gradients, fluid build-up may activate cell mechanosensors, or the fluid may physically carry cancer cells to lymph nodes and blood vessels[96-98]. Decreasing tumour IFP can increase the efficacy of chemotherapy, radiotherapy and immunotherapy due to improved drug uptake, perfusion and immune cell infiltration[15]. Determination of IFP in the clinic may predict treatment resistance and help design more suitable treatment protocols[99].

IFP can be determined invasively by micropuncture, wick-in-needle or piezoelectric techniques. These invasive, tissue-damaging procedures are uncomfortable for patients, have high variability and may alter IFP from physiological levels[92]. In addition, random sampling of small tumour regions fails to highlight spatial distribution of IFP in different directions and locations[100]. Non-invasive evaluation of forces or stiffness in the TME could provide statistically powerful biomarkers of treatment response. Currently, there is no reliable non-invasive method to determine IFP.

Contrast enhanced (CE)-magnetic resonance imaging (MRI) has been suggested to non-invasively estimate IFP. This method requires slow infusion (~2 hours) of gadolinium-based contrast agent (GBCA), long imaging times to longitudinally monitor uptake, and at least two direct pressure measurements[91, 99]. A drop in IFP at the tumour periphery was identified in lung tumour models and the level of GBCA reaching the tumour centre was related to IFP (Figure 1.8)[99]. However, inference of an accurate quantitative relationship between GBCA concentration and IFP is difficult because fluid velocity through tumour blood vessels is extremely varied[101]. Weak or no correlations were found between CE-MRI-estimated tumour IFP and invasive IFP measurements in various tumour models[102-104]. More recently, the potential of magnetic resonance elastography (MRE) and convection MRI approaches to estimate IFP have been evaluated but are still in their infancy[93, 105, 106].

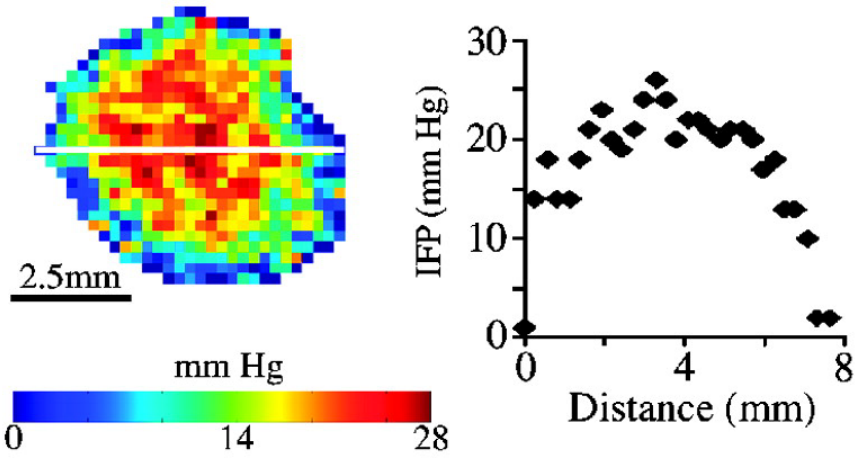

Figure 1.8: *IFP map and corresponding IFP values from a pre-clinical lung tumour measured using CE-MRI. IFP was lower at the tumour periphery. Figure from [99].*

1.4 Therapeutically targeting the tumour associated ECM

The link between ECM accumulation, elevation of local forces, tumour progression, and reduction of drug delivery suggests that patients would benefit from stromal-targeted therapy[16]. However, the utility of stromal-targeted therapy is not fully understood; it can both suppress tumour progression through enhancement of drug delivery and promote tumour progression by removing barriers to invasion and metastasis[41, 57, 107]. Stromal modulators should be rigorously tested, used with caution and identification of patients most likely to benefit is crucial. Current techniques used to target the tumour-associated stroma target ECM production, ECM remodelling, cell-ECM interactions or directly degrade ECM components.

1.4.1 Therapeutically targeting ECM production

Hedgehog paracrine signalling in the pancreatic TME promotes desmoplasia and plays a role in cancer EMT and stem cell maintenance[108, 109]. Pre-clinical inhibition of the hedgehog pathway produced a transient increase in tumour perfusion and delivery of gemcitabine[110]. Inhibition of sonic hedgehog (SHH), a ligand component of this pathway, was shown to deplete pancreatic ductal adenocarcinoma (PDAC) desmoplasia, improve the anti-tumour effects of gemcitabine, but tumours were sometimes more aggressive and proliferative[108, 111]. Clinical evaluation of hedgehog inhibitors has had similar heterogeneous responses, some trials report increased chemotherapy delivery through stromal depletion whilst another voluntarily closed as patients had a shorter median survival compared to placebo[112].

Angiotensin inhibition, for example with losartan, reduces collagen and HA synthesis through suppression of profibrotic TGF-β, connective tissue growth factor (CTGF), and angiotensin receptor type I (AT1R) signalling[113, 114]. Losartan can reduce collagen expression, increase drug delivery and improve survival in multiple murine tumour models[113, 115, 116]. Angiotensin inhibitors, often in combination with chemotherapy, are undergoing clinical

trials to treat a variety of solid tumours[11, 16]. Losartan is already FDA approved for treatment of hypertension and so, if successful, it would provide a relatively cheap method of sensitising solid tumours to chemotherapy.

1.4.2 Therapeutically targeting ECM remodelling

MMPs remodel and degrade components of the ECM and their dysregulated activity in cancer can contribute to angiogenesis, tumour growth and metastasis[117]. Cyclooxygenase-2 (COX-2) overactivation in cancer can increase MMP activity and has been implicated in angiogenesis, apoptosis and tumour invasiveness[118-120]. COX-2 inhibition with celecoxib reduced αSMA+ CAF and proinflammatory immune cell recruitment into the TME, decreased collagen deposition, and inhibited tumour growth and metastasis in a pre-clinical breast cancer model[121]. The clinical promise of COX-2 or MMP inhibition is currently restricted due to serious dose-limiting toxicities[117, 118].

Lysyl oxidase (LOX) is commonly overexpressed in stromal-dense tumours and promotes collagen and elastin crosslinking, the formation of pre-metastatic niches, and surface expression of epidermal growth factor receptor (EGFR) on cancer cells[122-124]. Pre-clinically LOX inhibition can reduce tumour size, focal adhesion formation, tumour aggression and metastasis[29, 125]. Currently, development of small molecule inhibitors which specifically target LOX is challenging because only the LOXL2 crystalline structure is known[125, 126].

1.4.3 Therapeutically targeting cell-ECM contacts

Inhibition of signalling downstream of focal adhesions can reduce stromal-dense tumour progression, particularly when used in combination with chemotherapy. Two promising targets are FAK and Rho-associated protein kinase (ROCK)[16]. FAK inhibition can halt breast tumour progression, reduce fibrosis and cell motility, increase apoptosis, and improve the

efficacy of chemotherapy and immunotherapy[127-129]. The latter were attributed to increased infiltration of drug and CD8+ T cells respectively[127]. Study results are pending for multiple clinical trials evaluating FAK inhibitors in various solid tumours[16, 130, 131]. ROCK inhibitors (e.g. Fasudil) remain largely in pre-clinical development, showing promising anti-tumour effects in pancreatic, breast, prostate and uterine cancer models[132, 133]. One ROCK inhibitor (AT13148) has reached phase I clinical trials and was well tolerated in patients with advanced solid tumours (NCT01585701)[133].

1.4.4 Therapeutically degrading ECM components

Collagen is the most abundant fibrous protein within the interstitial ECM and is thought to have the greatest effect on drug diffusion in stromal-dense tumours[8, 134]. Collagenases cleave at distinct sites along the collagen triple helix and can pre-clinically improve drug penetration into the tumour[135]. However, clinically there are issues concerning degradation of healthy tissue collagen, the potential increase in tumour metastasis, immunogenicity against the currently available bacterial collagenases, and the narrow therapeutic window[135, 136].

HA is another major component of the interstitial ECM which accumulates in 20-30% of human tumours: most notably breast, pancreatic, colon, and prostate cancers. This GAG forms a pressure creating gel that can sequester growth factors and inhibit fluid movement within the TME. Hyaluronidase enzymes degrade HA, reduce mechanical stress and improve tissue compliance through release of previously immobilised fluid[137, 138]. PH20 is a human hyaluronidase anchored to the external surface of cells by a glycosylphosphatidylinositol (GPI) and exhibits relatively high activity across a broad pH range[52]. Pegvorhyaluronidase alfa (PEGPH20, Halozyme Therapeutics), is a recombinant, PEGylated human PH20 lacking the GPI anchor region[139]. PEGPH20 has been shown to effectively degrade HA, reduce tumour IFP, decompress blood vessels, increase influx of CD8+ T cells, and improve treatment outcome in a range of ectopic, orthotopic and GEM models of cancer (Figure 1.9)[15,

[140-142]. PEGylation prolongs the circulatory half-life of the agent improving its suitability clinically; in mouse models this increased from 2.3 minutes to 10.3 hours[14].

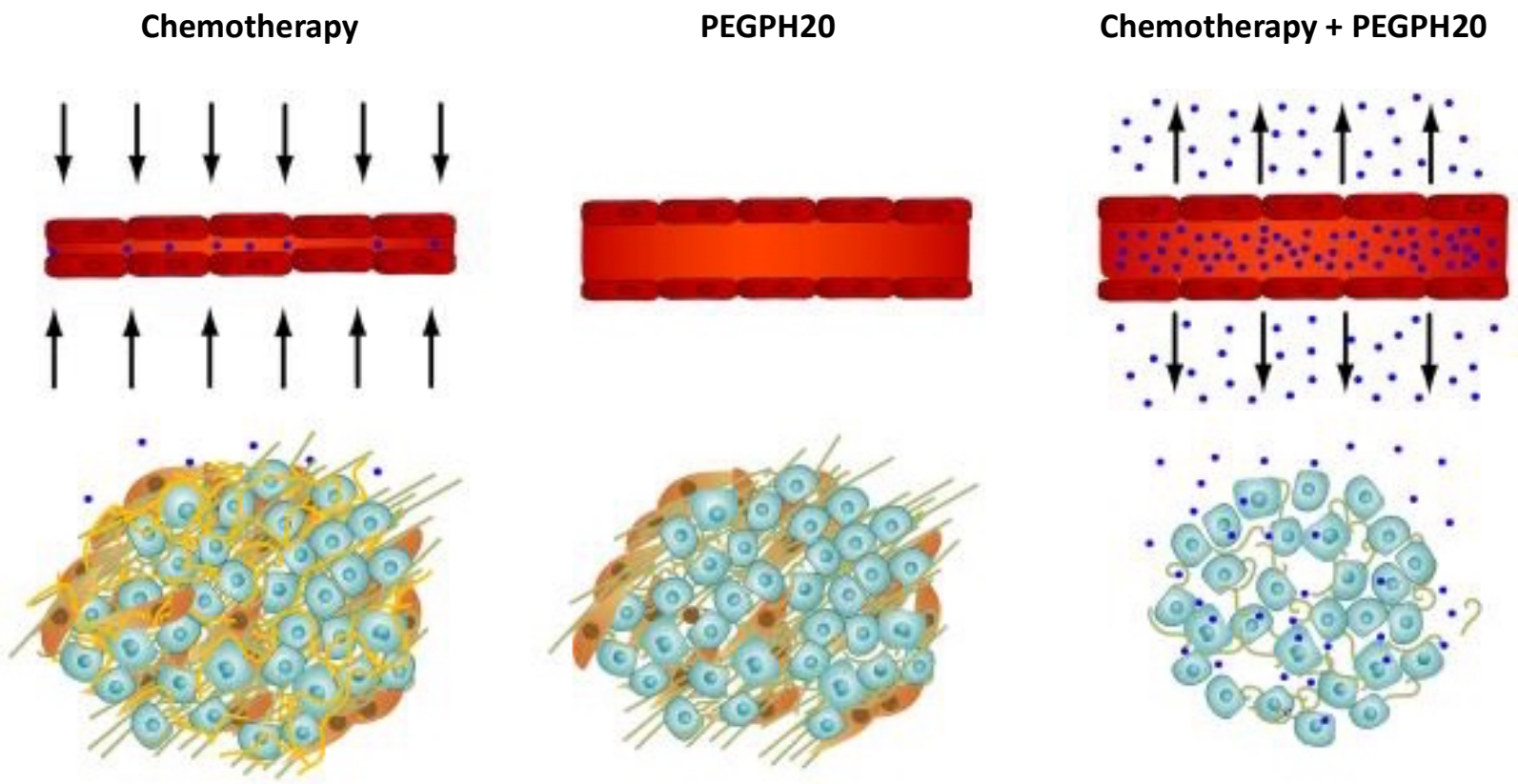

Figure 1.9: *A schematic of PEGPH20 treatment effects as a monotherapy and in combination with chemotherapy – adapted from [15]. Cancer and stromal cells are shown in blue and orange respectively. PEGPH20 can degrade HA (yellow), decompress blood vessels (red), and improve chemotherapy delivery (dark blue dots).*

PEGPH20 is delivered intravenously prior to traditional treatments, such as chemotherapy or immunotherapy, to improve their delivery and efficacy[15, 38, 140, 143]. A phase Ib trial of PEGPH20 combined with gemcitabine indicated that tumour HA levels may be predictive of response[38]. Approximately 35% patients had HA 'high' tumours; defined in these trials as HA staining of any intensity present in ≥50% of the tumour surface[144]. In a phase II trial, PEGPH20 in combination with standard of care treatment in 84 patients with HA 'high' PDAC tumours modestly improved overall survival (OS) from 7.8 months to 11.7 months. Treatment with PEGPH20 had no significant impact on survival of 162 patients with HA 'low' PDAC[144]. Despite promising preliminary data, the phase III trial (HALO-109-301) showed that PEGPH20 in combination with standard of care chemotherapy failed to improve overall survival of patients with previously untreated HA 'high' metastatic PDAC, and further clinical development of PEGPH20 was halted in late 2019[139, 145]. It is likely that PEGPH20 did improve the delivery of the chemotherapy to the tumour in these patients, however, increasing drug delivery was not enough to improve survival due to pancreatic tumour cell resistance to chemotherapy. Therefore, PEGPH20 may still be a useful tool to improve drug delivery, and another combination treatment strategy in a new cancer patient population could be explored to provide greater patient benefit. As a result, the work of this PhD to identify a non-invasive method to monitor PEGPH20 response remains of use and was continued despite the trial failure.

Degrading ECM components for therapeutic benefit is complex. Non-invasive imaging biomarkers which can inform on HA degradation at the individual patient level before, during and after therapy may improve understanding and help the success of similar therapeutic strategies in the future. Other methods to therapeutically degrade HA in cancer are still being evaluated today, such as a hyaluronidase-expressing oncolytic virus in pre-clinical models of glioblastoma[146]. It is likely that MRI biomarkers that are sensitive to HA degradation by PEGPH20 will also inform on response to these other more novel HA degradation methods.

1.5 Imaging biomarkers

Biomarkers, defined as 'characteristics measured objectively which are indicative of normal biology, pathology or pharmacology', can be prognostic and/or predict likely treatment responses at the individual patient level[147]. Biomarkers inferred invasively from biopsies are limited because they only capture a small sample of the tumour and cannot evaluate spatial heterogeneity or tumour biomechanical properties.

Advanced imaging techniques provide biomarkers which quantitatively and non-invasively assess spatial and temporal heterogeneity within a tumour[147]. Unlike histopathology, imaging biomarkers can be evaluated at multiple time points within the same patient which results in improved statistical power, more stringent pre-clinical evaluation with lower animal numbers, and smaller clinical trials.

There is an unmet and growing need for validated imaging technologies which can guide clinical decision making through quick and accurate detection, diagnosis and monitoring of cancer. Many imaging biomarkers have failed to translate into clinically useful tools as they are disconnected from relevant biology and/or fail to predict outcome[147]. Extensive validation, which relies upon close imaging-pathology correlations, is required to understand the underlying biology before imaging biomarkers can be incorporated into clinical trials[147-149]. Meaningful studies are often conducted in animal models; typically, the physiological tumour-stromal interactions seen in the human disease are best recapitulated by orthotopic, GEM and PDX models.

Pre-clinical imaging modalities include positron emission tomography (PET), computed tomography (CT), single photon emission computed tomography (SPECT), bioluminescence imaging (BLI), ultrasound (US) and MRI. These modalities differ in their depth penetration, spatial and temporal resolution, energy required for image generation, and availability of injectable and biocompatible molecular probes (Table 1.1)[147, 150, 151].

Table 1.1: *Comparison of pre-clinical imaging modalities.*

Imaging Modality	Energy	Spatial Resolution	Penetration Depth	Advantages	Limitations	Clinical Translation
Bioluminescence imaging (BLI)	Visible to infrared light	3-5mm	Several cm	High sensitivity	Limited penetration depth Higher concentration of contrast agent required	No
Positron emission tomography (PET)	Annihilation photons	1-2mm (microPET) 6-10mm (clinical PET)	No limit	High sensitivity Trace amounts (ng) of contrast agent needed Whole body imaging	Exposure to ionising radiation	Yes
Single photon emission computed tomography (SPECT)	Gamma rays	0.5-2mm (microSPECT) 7-15mm (clinical SPECT)	No limit	High sensitivity Trace amounts (ng) of contrast agent needed Whole body imaging	Exposure to ionising radiation	Yes
Magnetic resonance imaging (MRI)	RF waves	0.01-0.1mm (small animal MRI) 0.5-1.5mm (clinical MRI)	No limit	High spatial resolution Superior soft tissue contrast Non-contrast techniques available Whole body imaging Anatomic imaging	Higher concentration of contrast agent required	Yes
Ultrasound (US)	High frequency sound waves	0.04-0.1mm (small animal US) 0.1-1mm (clinical US)	Several cm	High sensitivity Real-time imaging Portable Anatomic imaging Therapeutic applications (HIFU)	Higher concentration of contrast agent required Operator dependency Cannot image around lung and bone	Yes

1.5.1 Basic principles of MRI

MRI relies on the principle that magnetic dipoles or nuclear spins, such as hydrogen protons (^{1}H), align parallel or antiparallel when placed in a strong, uniform magnetic field (B_0). Within the human body water molecules are the greatest source of ^{1}H and so MRI essentially probes tissue water content, organisation and mobility. Aligned dipoles precess around the direction B_0 at the Larmor frequency (ω_0) which is proportional to the strength of the magnetic field. A radiofrequency (RF) coil can produce a pulse which alters the alignment of spins. The relaxation time taken for the spins to return to baseline can be detected and translated into an MR signal[150]. The timing of pulse excitation and recording can be changed, resulting in different magnetic contrasts with the most common being T_1 (longitudinal relaxation time) and T_2 (transverse relaxation time).

MRI is sensitive to soft tissue differences and abnormalities such as a tumour; for example, tumour growth often results in increased cellularity which increases the MR signal on T_2-weighted images. Exogenous chemical agents, known as contrast agents, can be injected which change the MR signal intensity and enhance tissue differences to confirm an abnormality. Conjugation of a substrate to a contrast agent can assess protein expression and enzyme activity *in vivo*[152]. MRI has higher spatial resolution compared to radionuclide or optical probe techniques (μm compared to mm) and can produce anatomical information simultaneously. However, MRI is less sensitive and requires greater amount of contrast agent for detection[150].

1.5.2 MRI biomarkers used in oncology

Various MRI biomarkers exist and have the ability to inform upon tissue architecture, vascular morphology and function, hypoxia, and metabolism. Degradation of tumour HA by PEGPH20 is known to decompress blood vessels, improve drug delivery, collapse the extracellular space, and reduce water content, IFP, and hypoxia[14, 49, 153]. MRI biomarkers which

may be informative when evaluating response to PEGPH20 are summarised in Table 1.2. The imaging biomarkers evaluated throughout this thesis were selected because they did not require contrast agents, could be estimated using sequences that were already available and optimised on the 7T MRI system used, and could be translated into the clinic with relative ease.

Table 1.2: *Quantitative MRI biomarkers which may be of interest when assessing HA accumulation and its therapeutic degradation.*

MRI	Biomarker	Physiology	Reference
MRI relaxometry	T_1 (ms)	Ratio of free (long T_1) to bound (short T_1) water	[154]
	T_2 (ms)	Ratio of free (long T_2) to bound (short T_2) water	
Magnetisation transfer (MT)	MTR (%)	Proportion of water bound to macromolecules	[155]
Diffusion weighted MRI (DWI)	ADC ($mm^2.s^{-1}$)	Water diffusion	[156]
MR elastography (MRE)	G_d (kPa)	Elasticity	[157-159]
	G_l (kPa)	Viscosity	
	|G*| (kPa)	Stiffness	
	Y	Relative contribution of G_d and G_l to |G*|	
Dynamic contrast enhanced (DCE)-MRI (typically GBCAs)	Initial area under the gadolinium curve (IAUGC)	Vascular perfusion and permeability (model-free)	[160]
	K^{trans} (min^{-1})	Vascular perfusion and permeability	
	Vp	Blood plasma volume	
Susceptibility contrast (SC)-MRI (USPIO contrast agent)	ΔR_2 and ΔR_2* (s^{-1})	Perfusion and blood volume	[161-164]
	fBV (%)	Fractional tumour blood volume	
	VSI (μm)	Blood vessel calibre	
Intrinsic susceptibility (IS)-MRI	Baseline R_2 and R_2* (s^{-1})	Paramagnetic species	[165-167]

1.5.2.1 MRI relaxometry

T_1 and T_2 relaxation times will differ in different physiological environments. T_1 is dependent on nearby water molecules; fluid regions of widely-spaced freely-moving water molecules will have long T_1 values whilst restricted environments such as fat will have a shorter T_1. T_2 is influenced by interactions with neighbouring nuclear spins; freely moving water molecules have a greater incidence of spin-spin interactions and a loss of spin coherence with ω_0 leading to longer T_2 relaxation times. T_2 relaxation time is always shorter than T_1 in a given tissue. Assessment of native T_1 pre-clinically and in a small number of clinical trials suggests that a reduction in T_1 is indicative of treatment response in various solid tumour types[168-172].

1.5.2.2 Magnetisation transfer (MT) imaging

MT imaging can assess protons bound to macromolecules or structured hydration layers which are essentially invisible in T_2-weighted images. The bound 'pool' of protons can influence the free water pool through the exchange of energy. The bound pool has broad resonance and can be exclusively excited by a radiofrequency pulse applied kilohertz away from the free water pool frequency, with no effect on the free water protons. Saturated magnetisation from the 'invisible' bound pool can move to the free water pool and reduce the total MR signal. The small saturation effect on the free water pool, quantified as the MT ratio (MTR), is suggestive of the physiological levels of the macromolecule of interest[155]. MTR has been used to discriminate between malignant and benign lesions[171]. MTR is sensitive to ECM accumulation and has been shown to correlate with fibrosis in pancreatic cancer and collagen content in meningiomas[173-175].

Chemical exchange saturation transfer (CEST) imaging has been built on the concept of MT. CEST imaging uses one chosen off resonance frequency on both sides of the free water peak to excite a particular exogenous agent or endogenous macromolecule in the bound pool.

Examples of endogenous substances/processes within the tumour microenvironment which can be indirectly monitored by CEST include glucose, glutamate, protein aggregation, protein degradation and GAGs[176-180]. The most relevant of these is gagCEST, however, this thesis does not explore gagCEST in relation to PEGPH20 treatment because this method remains in its infancy, particularly with regard to oncological applications, and clinical translation is difficult due to negligible gagCEST signal seen at clinical magnetic field strengths even in high expressing tissues such as cartilage[178, 179]. Following further optimisation, this method may prove useful in relation to HA and its therapeutic degradation in the future.

1.5.2.3 Diffusion weighted imaging (DWI)

DWI uses the random Brownian motion of water molecules within tissues to non-invasively quantify and map the apparent diffusion coefficient (ADC). ADC is sensitive to the movement of water molecules, predominantly extracellular, and can inform upon various phenomena including the presence of macromolecules, permeability of membranes and equilibrium of intracellular and extracellular water[150]. Solid tumours commonly have restricted diffusion compared to normal tissues due to increased cellularity and reduction in extracellular space. Typically, cell shrinkage, fragmentation, loss of membrane integrity, and death following successful therapy increase ADC in various solid tumours[171, 181, 182].

Intravoxel incoherent motion (IVIM) MRI is a variation of DWI which is sensitive to blood flow in capillaries (i.e. perfusion) without the need of contrast agents as this phenomenon can mimic a diffusion process. The majority of the IVIM effect can be measured at small b values (e.g. below 200 s/mm^2) and therefore can be separated from tissue water diffusion and measures of ADC mentioned previously[183]. IVIM has been gaining popularity in oncology as an endogenous perfusion MRI method, particularly in areas of the body less affected by motion such as the brain. IVIM MRI may inform on blood vessel decompression following PEGPH20

treatment, however, this technique was not explored during this PhD project as IVIM parameters can be error prone and there was not an optimised sequence available on the 7T pre-clinical MRI system used[183].

1.5.2.4 Magnetic Resonance Elastography (MRE)

Periodic application of a force generates mechanical waves which propagate through tissues with a different speed that depends on the type of wave generated (e.g. shear or longitudinal), the corresponding elastic and viscous moduli (e.g. shear or bulk), the amplitude of the vibration, and the frequency of the vibration. In biological tissues the wave will be attenuated (dampened) as it propagates depending on the viscosity and the amount by which the wave energy is redirected by refraction, reflection and scattering. Elastography evaluates the propagation of mechanical waves, and imaging the resulting tissue deformation can non-invasively map and quantify, under certain simplifying assumptions, the viscoelastic properties[184-188]. Based on the imaging technique, elastography falls mainly into three types: MRE, ultrasound elastography and optical elastography[188-192]. This thesis focussed on the application of MRE only.

The aim of MRE is to measure and map the distribution of shear elastic and viscous moduli by measuring the local speed of shear waves of known frequency. The amplitude of the shear waves is assumed to be small enough that the results are not significantly dependent on the amplitude. MRE typically uses an external driver to generate vibrations of a single frequency which excite the tissue of interest; multiple frequency MRE is less common[193, 194]. The signal generated for these external driver devices is synchronised to the MR pulse sequence and amplified[186]. Motion-encoding gradient (MEG) pairs allow the local and instantaneous tissue displacements associated with propagating shear waves to be encoded in the phase of MR images creating snapshot images of wave movement throughout the tissue (Figure 1.10)[187].

MRE yields quantitative images called elastograms, which map the shear elastic modulus (G_d units of kPa), shear viscous modulus (G_l kPa), the absolute value of the complex shear modulus ($|G^*| = \sqrt{[G_d^2+G_l^2]}$ kPa), and the normalised phase angle ($Y = 2/\pi[\tan^{-1}[G_l/G_d]]$ dimensionless)[159]. G_d and G_l form the real and imaginary parts respectively of G* (a complex number), which describes the tissue stiffness. The phase angle (Y) describes the relative contributions of G_d and G_l to |G*|. Tissue properties range from pure elastic (Y = 0) to pure viscous (Y = 1)[159]. MRE has excellent reproducibility, repeatability, high inter-observer agreement, and reproducibility across different manufacturers[74].

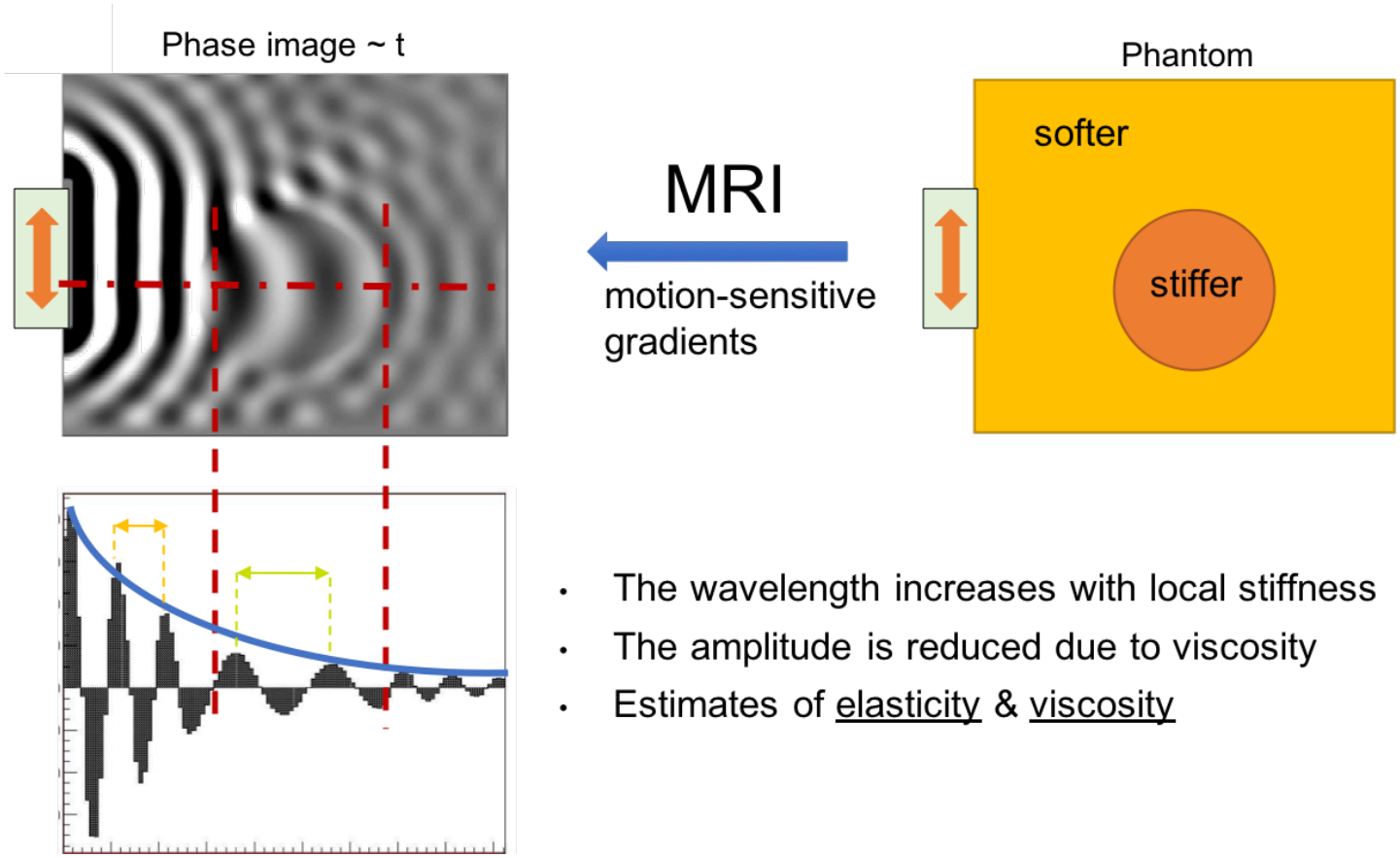

Figure 1.10: *Measurement of viscoelastic properties with magnetic resonance elastography (MRE). The characteristics of the propagating mechanical wave will change depending on the local stiffness and viscosity of the tissue or phantom. Imaging the wave propagation with MRE can give, under certain simplifying assumptions, an estimate of the viscoelastic properties. Wave images provided by Professor Ralph Sinkus.*

MRE can identify many malignant solid tumours, including breast, because they are often stiffer than the surrounding healthy tissue and benign lesions[74, 188, 195]. MRE investigations of high-grade malignant brain tumours, such as gliomas and glioblastomas, showed them to be softer than lower grade lesions and surrounding healthy brain tissue[83, 158, 196]. Pre-clinical studies have shown significant reductions in $|G^*|$, G_d and G_l in breast and pancreatic tumours following treatment with vascular disrupting agents[74, 157, 197, 198]. Alteration of viscoelastic properties following chemotherapy is less clear, with MRE-derived stiffness decreasing in some *in vivo* solid tumour models and increasing in others[199, 200]. MRE may be useful to monitor responses to stromal-targeted therapy given that the tumour-associated stroma is a major contributor to tissue stiffness[46, 152].

1.5.2.5 Intrinsic susceptibility (IS) MRI

IS-MRI measures the transverse relaxation rate R_2^* ($1/T_2^*$) which is sensitive to magnetic field inhomogeneities caused by paramagnetic species[165-167]. Susceptibility perturbations, which occur around blood vessels containing deoxyhaemoglobin, increase R_2^*[165]. IS-MRI, also commonly referred to as blood oxygen level dependent (BOLD) MRI, can inform on tissue oxygenation and haemodynamic function of surrounding vasculature. Tumours often exhibit relatively fast R_2^* compared to most normal tissues, a consequence of the high concentration of deoxygenated red blood cells (RBCs) within the typically chaotic and unstable microcirculation[201]. IS-MRI has thus been utilised to investigate tumour angiogenesis and response to vascular targeted therapies[169, 202]. A recent study showed that parametric maps of tumour R_2^* reflect the spatial variation in RBCs seen histologically[202].

1.5.2.6 Contrast-enhanced (CE) MRI

Imaging with exogenous contrast agents, for example gadolinium-based contrast agents (GBCAs) or ultrasmall superparamagnetic iron oxide (USPIO), can inform on the architecture and patency of the tumour microvasculature.

Dynamic contrast enhanced (DCE)-MRI normally involves rapid acquisition of T_1-weighted images before, during and following intravenous injection of a T_1-shortening GBCA. DCE-MRI measures GBCA extravasation from the blood plasma compartment to the extravascular extracellular compartment through the typically hyperpermeable tumour blood vessels, often expressed by the volume transfer constant K^{trans} (min^{-1}), and used to inform on tumour perfusion, vessel permeability and density, and overall blood volume[160]. An effective antivascular agent would be expected to elicit a reduction in K^{trans}[203]. GBCAs have a half-life of approximately 90 minutes and any residual gadolinium remaining in tissues will influence the MR signal in later images, particularly when repeat contrast agent dosing is used[204]. K^{trans} increased (50 - 56% on average) following PEGPH20 monotherapy and PEGPH20 in combination with gemcitabine in pre-clinical models of PDAC[205]. Moreover, in the phase 1b trial of PEGPH20, median K^{trans} increased (16 - 547%) in patients with pancreatic cancer following successful treatment[38, 143, 171]. Despite the promise of K^{trans} as a biomarker of successful PEGPH20 treatment, there are safety concerns around the use of GBCAs, for example GBCAs may cause nephrogenic systemic fibrosis or build-up in the brain. Therefore alternative CE, or endogenous contrast based MRI methods to monitor tumour response to PEGPH20 would be preferable and easier to translate into the clinic[206].

Susceptibility contrast (SC)-MRI evaluates changes in tumour R_2 ($1/T_2$) and R_2^* ($1/T_2^*$) following intravenous injection of USPIO particles which have a relatively long intravascular half-life compared to GBCAs[201]. USPIO particles are assumed to remain intravascular and at steady-state within the plasma for the entirety of the scan. Fractional blood volume (%)

and vessel size (μm) can be estimated using R_2 and R_2* values acquired before and after injection of USPIO particles[162, 163, 201, 207]. SC-MRI biomarkers decrease following effective tumour response to anti-angiogenic drugs[161, 208]. A recent study showed that SC-MRI-derived blood volume increased following PEGPH20 treatment in a pre-clinical model of pancreatic cancer[209].

1.6 Aims of this PhD thesis

Evaluation of tumour characteristics spatially and temporally with non-invasive imaging biomarkers may help improve biological understanding and personalisation of stromal-targeted therapies (e.g. PEGPH20).

The aims of this PhD thesis are to:

i) evaluate the sensitivity of endogenous MRI biomarkers to HA accumulation and its therapeutic degradation by PEGPH20 in pre-clinical models of breast cancer
ii) use histology to characterise and understand the biological determinants of the MRI biomarkers

1.6.1 Thesis structure

Chapter 2 summarises the materials and methods used throughout this thesis.

Chapter 3 demonstrates the ability of ADC to detect pre-clinical breast tumour response to HA degradation by PEGPH20, and compares this to T_1, T_2 and MTR.

Chapter 4 explores the effect of PEGPH20 on tumour viscoelastic properties measured by MRE.

Chapter 5 evaluates whether IS-MRI can inform on breast tumour vasculature response to PEGPH20.

Chapter 6 collates all the data from chapters 3, 4 and 5 to probe the biological determinants of the MRI biomarkers in more depth.

Chapter 7 provides a summary, conclusion and appraisal of potential avenues of future research.

Chapter 2: Materials & Methods

2.1 Gelatine Phantoms

Multiparametric MRI evaluation of gelatine phantoms with increasing concentration was performed to confirm that T_1, T_2, MTR, ADC, G_d, G_l, $|G^*|$, and Y are sensitive to increasing ECM accumulation at physiological levels. Gelatine-based phantoms were chosen as they are well studied in elastography, are simple and relatively straightforward to reproducibly manufacture, and mimic biological tissue[210]. However, gelatine phantoms are much less complex compared to biological tissues and consist of sparsely interlinked chains of denatured collagen, a major component of the ECM[211, 212].

Gelatine powder from porcine skin (Type A, Sigma, G2500) was dissolved in distilled water to create phantoms of various percentages (w/w). Once mixed, solutions were heated to at least 50°C in a microwave and degassed in a vacuum chamber before being poured into a 3D printed mould with a shape complementary to the MRE set up (Figure 2.1). Resulting gel phantoms were left to set overnight at room temperature (~22°C). Approximately 24 hours after preparation, phantoms underwent multiparametric MRI. Phantoms of different concentrations were scanned in separate, identical imaging sessions across different days.

A limitation of these gelatine phantoms is that they do not include HA. Attempts were made to make an HA phantom or inclusion; however, these were costly to prepare at a high concentration, fragile with a slippery surface which meant MRE was difficult to perform, and inclusions had problems with air bubbles and artefacts which made the data unusable. At the start of this PhD project the primary focus was the *in vivo* application of MRE and so rather than use a substantial amount of time on HA phantom manufacture, the project moved onto an *in vivo* pilot study in a tumour model with a high baseline HA accumulation.

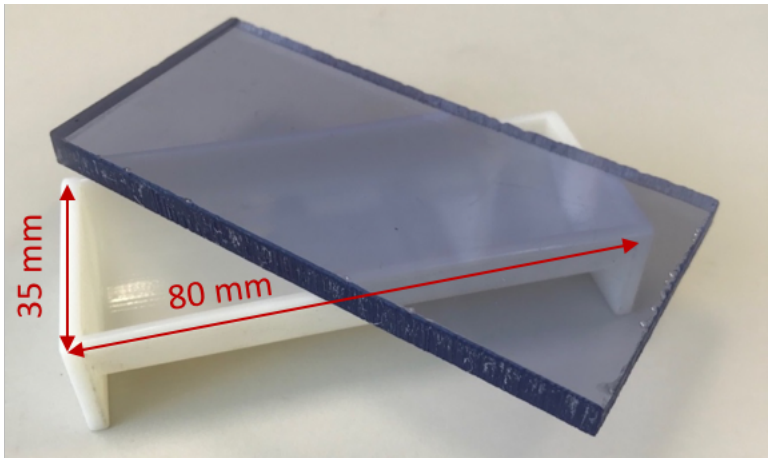

Figure 2.1: *Mould used to manufacture gelatine phantoms. The 3D printed design is identical in semi-cylindrical shape to the MRE set up (diameter 35 mm, length 80 mm).*

2.2 Cell lines

All cell lines tested negative for *Mycoplasma* infection and cell identity was authenticated by short tandem repeat (STR) profiling. luc-MDA-MB-231 LM2-4 highly malignant luciferase-expressing triple negative breast cancer cells isolated from a lung metastasis were provided by Dr R. Kerbel (University of Toronto, Canada) and were cultured in Dulbecco's modified eagle's medium (DMEM; Invitrogen, Life Technologies) supplemented with 10% (v/v) foetal bovine serum (FBS; Pan Biotech). 4T1 murine breast adenocarcinoma cells and 4T1/HAS3 murine breast adenocarcinoma cells which overexpress HA synthase 3 (HAS3) were provided by Halozyme Therapeutics (San Diego, USA). 4T1 cells were cultured in RPMI 1640 medium (Gibco, 72400) supplemented with 10% FBS. 4T1/HAS3 cells were cultured in RPMI 1640 medium (Gibco, 72400) supplemented with 10% FBS and 100 µg/ml hygromycin B (Invitrogen, 10687010) for HAS3 selection.

2.3 Animals and tumour models

All animal experiments were approved by the Institute of Cancer Research Animal Welfare and Ethical Review Body, performed in accordance with the UK Home Office Animals (Scientific Procedures) Act 1986, and the United Kingdom National Cancer Research Institute guidelines for the welfare of animals in cancer research, and reported according to the Animal Research: Reporting *In Vivo* Experiments (ARRIVE) guidelines[213, 214]. Mice were housed in specific pathogen-free rooms in autoclaved, aseptic microisolator cages with a maximum of 6 animals per cage. Mice were allowed access to food and water *ad libitum*. A total of 64 mice were enrolled in this work.

Murine 4T1 and 4T1/HAS3 breast tumours were propagated orthotopically by injecting $1x10^5$ 4T1 or 4T1/HAS3 cells in 100 µl of sterile serum-free medium into the third mammary fat pad of adult female BALB/c mice (4T1: one study n = 14; 4T1/HAS3: three studies total n = 24). Human luc-MDA-MB-231 LM2-4 breast tumours were propagated orthotopically in the third mammary fat pad of adult female athymic NCr-*Foxn1*^{nu} mice by injecting $2x10^6$ luc-MDA-MB-231 LM2-4 cells in 100 µl Matrigel (Corning) and serum-free medium suspension (1:1 ratio; two studies total n = 26). Tumour development was monitored at least twice weekly by calliper measurements and tumour volume was estimated using the formula for an ellipsoid:

$$Volume = \frac{\pi}{6}(length \times width \times depth)$$

Tumour doubling time (DT) was calculated using:

$$DT\ (days) = \ln(2) \times (1/coefficient\ of\ x\ on\ exponential\ trendline)$$

The *in vivo* workflow is shown in Figure 2.2.

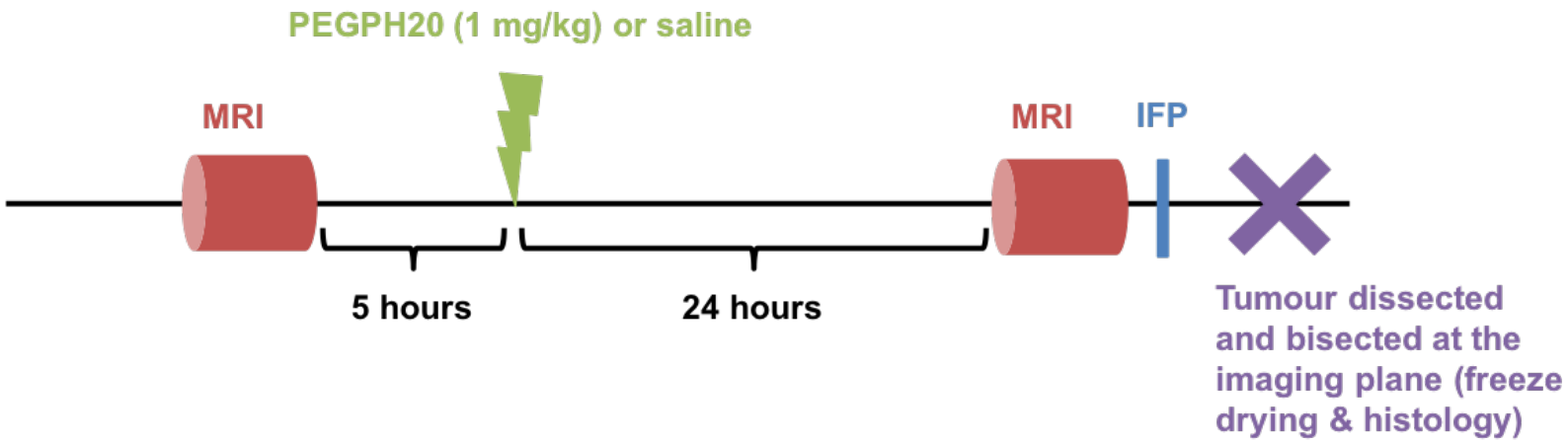

Figure 2.2: *Graphic describing the in vivo workflow used throughout this thesis. Pre-treatment MRI was performed when tumour reached sufficient size. Mice were then given 5 hours to recover from the anaesthesia before either saline or PEGPH20 (1 mg/kg) was administered intravenously. MRI was repeated 24 hours after treatment. After post-treatment MRI a terminal IFP measurement was taken, mice were killed (by cervical dislocation), and tumours were bisected at the MRI plane. One tumour half was embedded in formalin for histology and the other was weighed and freeze dried for estimation of tumour water content.*

2.4 Formulation, administration and dosing of PEGPH20

PEGPH20, a PEGylated, recombinant, human hyaluronidase (PH20), was provided by Halozyme Therapeutics and used to enzymatically degrade tumour HA[14]. A 24-hour timepoint and single 1 mg/kg dose were used[215]. PEGPH20 was diluted in saline and administered intravenously via a lateral tail vein. Control mice were treated intravenously with saline alone.

2.5 MRI data acquisition and analysis

For MRI, tumour-bearing mice were anaesthetised with a 7 ml/kg (4T1 and 4T1/HAS3) or 9 ml/kg (MDA-MB-231 LM2-4) intraperitoneal injection of Hypnorm™ (0.315 mg/ml fentanyl citrate plus 10 mg/ml fluanisone; Janssen Pharmaceuticals) and Hypnovel™ (5 mg/ml midazolam; Roche) and sterile water in a 1:1:2 ratio. This injectable anaesthesia combination was used as it has been previously shown to have minimal effects on tumour blood flow[216]. Body temperature was kept at approximately 37°C using a water heating pad. Pre-treatment MRI was performed when 4T1, 4T1/HAS3 and MDA-MB-231 LM2-4 tumours reached 453 ± 23 mm^3, 335 ± 23 mm^3 and 472 ± 24 mm^3 respectively (calculated using anatomical T_2-weighted MRI). Mice were given 5 hours to recover from anaesthesia before saline or 1 mg/kg PEGPH20 was injected intravenously. MRI was then repeated 24 hours after treatment.

MRI data were acquired on a 7T BioSpec 70/20 USR horizontal MRI system (Bruker Instruments, Ettlingen, Germany) using a purpose-built MRE platform and a volume coil (4 cm) positioned at the isocentre of the magnetic field (Figure 2.3)[157].

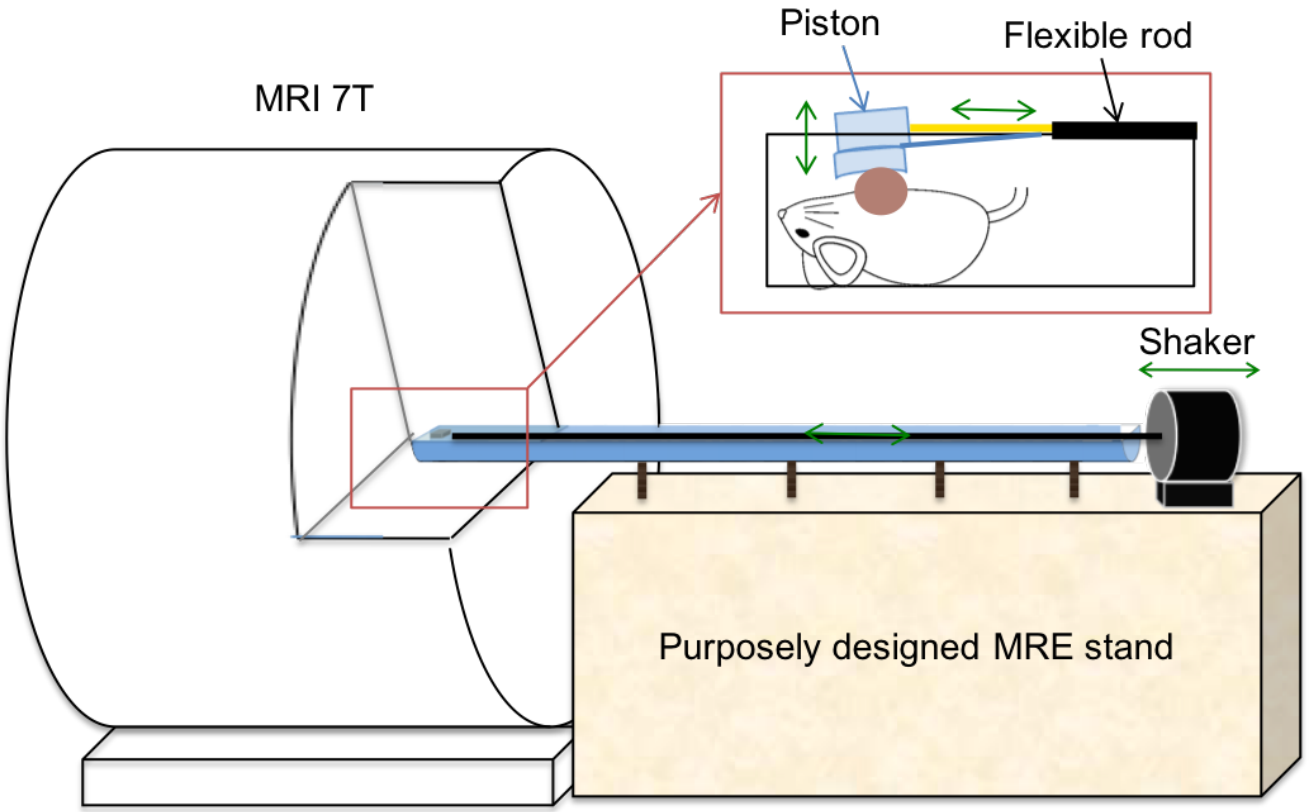

Figure 2.3: *Graphical representation of the purpose-built MRE platform used. Figure adapted from [157]. During MRE, a mechanical vibration is generated by an electromagnetic shaker, transmitted through a flexible nylon rod to a square piston which is in direct contact with the tumour or phantom. A cantilever allows conversion of the horizontal vibration of the shaker into vertical vibrations onto the tissue or phantom.*

Anatomical T_2-weighted images were first acquired using a rapid acquisition with refocused echoes (RARE) sequence (20 contiguous 1 mm thick axial slices) and were used to determine the tumour volume, plan the subsequent functional MRI acquisition, and optimise the local field (B_0) homogeneity over the tumour using the FASTMAP algorithm.

The subsequent functional MRI protocol included inversion recovery (IR)-TrueFISP for estimating T_1 and T_2 relaxation times, MT-RARE to derive the MTR, DWI for determination of the ADC, a multiple gradient echo (MGE) sequence to estimate R_2*, and finally MRE to quantify tumour viscoelastic properties. The details of each sequence used for phantoms and *in vivo* tumour models are shown in Tables 2.1 and 2.2 respectively. Total acquisition time was approximately 45 minutes, but this was variable *in vivo* due to the respiratory-gated DWI. R_2* was not measured in gelatine phantoms because they did not contain any paramagnetic material, and data would have been irrelevant to the *in vivo* setting.

Table 2.1: *Summary of MRI sequences used for gelatine phantom experiments.*

MR Imaging	Parameter	Slice Thickness (mm)	Field of View (mm)	Matrix Size	Echo Time (ms)	Repetition Time (ms)	Averages	Acquisition Time	Other
TurboRARE	Anatomical information	1	38.4 x 38.4	128 x 128	36	4500	2	2min 24sec	RARE factor of 8
IR-TrueFISP	T_1 (ms) T_2 (ms)	1	38.4 x 38.4	128 x 128	1.7	3.4	4	5min 20sec	50 inversion times (TI) between 72ms and 2737ms Flip angle 60°
MT-RARE	MTR (%)	1	38.4 x 38.4	128 x 128	19.22	1500	4	1min 36sec	8μT saturation strength 36 40ms pulses (gauss) Saturation at 100kHz ('off') and 7.5kHz ('on')
DWI	ADC ($mm^2.s^{-1}$)	1	38.4 x 38.4	128 x 128	37.88	1500	4	4min 24sec	B Values (s/mm^2): 200, 300, 500, 750, 1000
TurboRARE for MRE	Anatomical information	0.3	19.2 x 19.2	64 x 64	36	4500	8	4min 48sec	RARE factor of 8
MRE	G_d (kPa) G_l (kPa) |G*|(kPa) Y	0.3	19.2 x 19.2	64 x 64	30	504	2	12min 54sec	1kHz excitement Amplitude 7V 4 wave phases

Table 2.2: *Summary of MRI sequences used in vivo. *DWI acquisition time was variable because respiration triggering was used.*

MR Imaging	Parameter	Slice Thickness (mm)	Field of View (mm)	Matrix Size	Echo Time (ms)	Repetition Time (ms)	Averages	Acquisition Time	Other
TurboRARE	Anatomical information	1	30 x 30	128 x 128	36	4500	2	2min 24sec	RARE factor of 8
IR-TrueFISP	T_1 (ms) T_2 (ms)	1	30 x 30	128 x 128	1.7	3.4	4	5min 20sec	50 inversion times (TI) between 72ms and 2737ms Flip angle 60°
MT-RARE	MTR (%)	1	30 x 30	128 x 128	19.22	1500	4	1min 36sec	8μT saturation strength 36 40ms pulses (gauss) Saturation at 100kHz ('off') and 7.5kHz ('on')
DWI	ADC ($mm^2.s^{-1}$)	1	30 x 30	128 x 128	37.88	1500	4	4min 24sec*	Trigger (respiration) B Values (s/mm^2): 200, 300, 500, 750, 1000
MGE	R_2* (s^{-1})	1	30 x 30	128 x 128	3	200	8	3min 25sec	8 echo images 3ms echo spacing Flip angle 45°
TurboRARE for MRE	Anatomical information	0.3	19.2 x 19.2	64 x 64	36	4500	8	4min 48sec	RARE factor of 8
MRE	G_d (kPa) G_l (kPa) |G*|(kPa) Y	0.3	19.2 x 19.2	64 x 64	30	504	2	12min 54sec	1kHz excitement Amplitude 10V 4 wave phases

During MRE, a mechanical vibration was generated by an electromagnetic shaker (Brüel & Kjaer, Nærum, Denmark), transmitted through a flexible nylon rod to a square piston with either a semi-curved or flat end (Figure 2.4; 1.2cm x 1.2 cm, with various depth options between 2 mm and 7 mm). The piston was positioned in direct contact with the tumour or phantom. A cantilever allowed conversion of the horizontal vibration of the shaker into vertical vibrations onto the tissue or phantom.

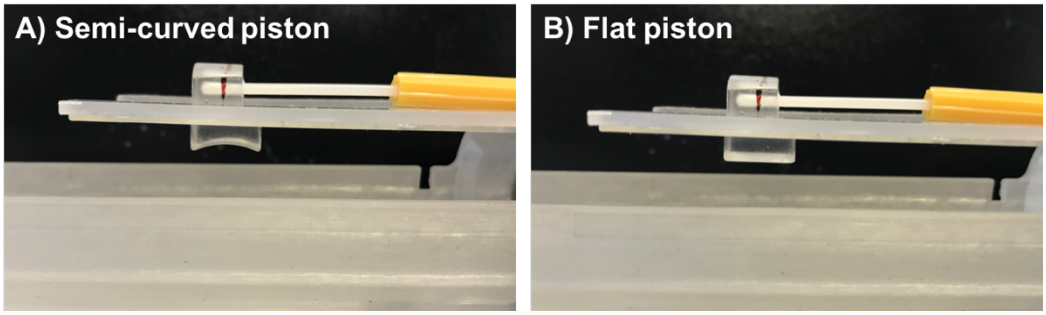

Figure 2.4: *Types of piston used for MRE. A semi-curved piston **(A)** was used for in vivo tumour studies and a flat piston **(B)** was used for gelatine phantoms. The depth of available pistons varied from 2 to 7 mm; the piston was changed to suit the size of the subject. Typically, a 5 mm semi-curved piston was used for 4T1 and 4T1/HAS3 tumours and a 3 mm semi-curved piston was used for MDA-MB-231 LM2-4 tumours.*

Parametric maps of T_1, T_2, MTR, ADC, and R_2* were reconstructed using in-house software from a 1 mm thick axial slice over a 38.4 x 38.4 mm (phantoms) or 30 x 30 mm (*in vivo*) FOV[217]. Parametric maps of G_d, G_l, |G*|, and Y were reconstructed isotropically from three 0.3 mm thick axial slices over a 19.2 x 19.2 FOV using software shared by Prof. Ralph Sinkus (King's College London)[218]. Median values for each tumour were calculated from a region of interest (ROI) which contained viable tumour tissue and excluded necrosis. Artefacts, such as those created by motion, were excluded from the ROI, and the median was used rather than the mean to further minimise their effect. Pre- and post-treatment ROIs were 'matched' by eye so that the tumour regions being compared were similar. This was important to improve data analysis in cases where necrosis was

present post-treatment that was not visible in the pre-treatment MRI, in these examples the same tumour regions were excluded despite there being less apparent necrosis in the pre-treatment MRI.

2.6 IFP measurement

Terminal invasive tumour IFP measurements were performed *in vivo* immediately after post-treatment MRI using a Millar Mikro-Tip® piezoelectric mouse pressure catheter (model SPR-1000, 0.33 mm diameter; Figure 2.5). To isolate IFP from total tissue pressure, the catheter was covered with modified polytetrafluoroethylene (PTFE) tubing (ID = 0.4 mm)[40]. The PTFE tubing was perforated (using a 27-gauge needle) to allow transmission of fluid pressure and minimise transmission of solid stress to the pressure sensor. Prior to each experiment, the catheter was placed in a water bath (~37 °C) until stabilisation and calibrated at 0 mmHg and 120 mmHg against a manometer. To insert the catheter into tumour tissue, a 23-gauge needle was firstly introduced into and removed from the tumour and then the covered catheter was quickly inserted into the pierced track. Care was taken to locate the pressure sensor at approximately the tumour centre. Data were collected for at least 5 minutes and the average pressure after stabilisation was calculated. Data were recorded and analysed using LabChart (ADInstuments).

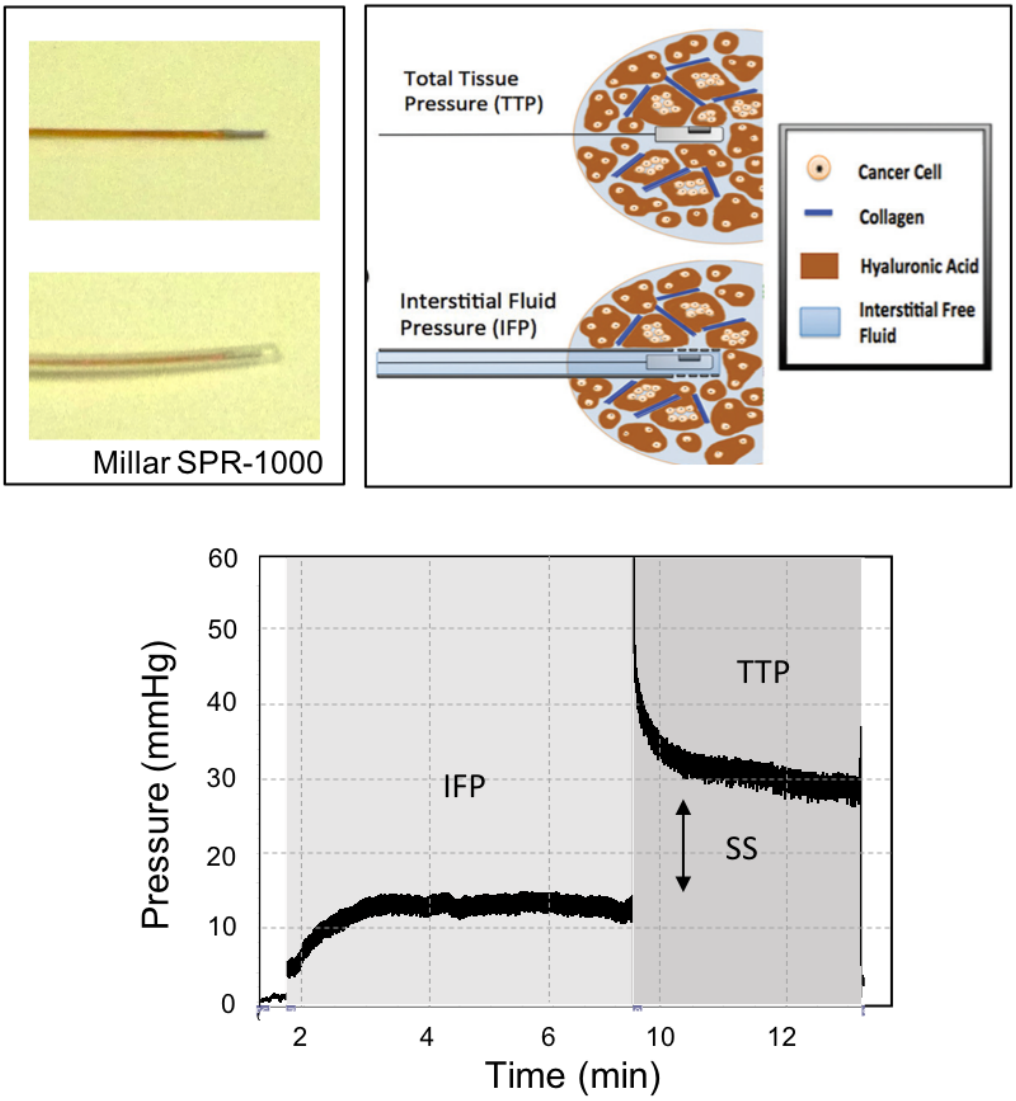

Figure 2.5: *Summary of the method used to separate total tissue pressure (TTP) into interstitial fluid pressure (IFP) and solid stress (SS) components. Images of the Millar SPR-1000 pressure catheter are shown. The probe was first covered with perforated tube to estimate the IFP, following which the tubing was removed to measure TTP. When both TTP and IFP are measured in the same region of the tumour the difference between them gives the SS. Figure created using [40].*

2.7 *Ex vivo* measurement of tumour water content

Guided by the post-treatment T_2-weighted MRI, tumours were carefully dissected and then bisected at the MRI plane. One tumour half was weighed, dried in a lyophiliser for 24 hours, and then reweighed. Tumour water content (%) was calculated using[14]:

$$Water\ content\ (\%) = \frac{wet\ weight - dry\ weight}{wet\ weight} \times 100$$

2.8 Histology and immunohistochemistry (IHC)

The other tumour half was fixed in formalin and embedded in paraffin. Serial FFPE tissue sections (5 μm) were cut using a microtome (Leica, RM2125RT). Sections were floated on a 45°C water bath (Raymond A Lamb), prior to mounting on positively charged microscope slides. Sections were air-dried at 22°C for approximately 1 hour, followed by baking overnight at 40°C (Windsor Incubator, Raymond A Lamb).

Haematoxylin and Eosin (H&E) staining was performed for the assessment of nuclear density, morphology and necrosis. HA was detected by an affinity histochemistry assay using a biotinylated, recombinant HA-binding protein (modified TSG-6 probe HTI-601, Halozyme Therapeutics; Figure 1.3)[70]. Collagen I & III were detected by picrosirius red staining[44]. Blood vessels were detected using CD31 immunohistochemistry. Staining protocols are summarised in Tables 2.3 (H&E), 2.4 (HA), 2.5 (collagen I & III) and 2.6 (CD31).

Table 2.3: *H&E staining protocol.*

Reagent	Time
Xylene	5 min
Xylene	2 min
100% ethanol	2 min
90% ethanol	2 min
70% ethanol	2 min
Rinse in running tap water	2 min
Gill's III haematoxylin	1.5 min
Rinse in running tap water	5 min
1% acid alcohol (1% HCl in 70% ethanol)	3 sec
Rinse in running tap water	4 min
Eosin	2 min
Rinse in running tap water	20 sec
70% ethanol	30 sec
90% ethanol	30 sec
100% ethanol	2 min
Xylene	2 min
Xylene	Until ready to mount in DPX

Table 2.4: *HA staining protocol using the modified TSG-6 probe HTI-601.*

Reagent	Time
Xylene	3 x 3 min
100% ethanol	3 min
95% ethanol	1 min
80% ethanol	1 min
Rinse in distilled water	2 min
3% H_2O_2	20 min
Rinse in washing buffer (0.05% Tween 20 in PBS)	3 x 3 min
Blocking buffer (2% w/v BSA + 2% v/v goat serum in PBS)	30 min
Rinse in washing buffer	3 x 3 min
Avidin block (Invitrogen 00-4303)	10 min
Rinse in washing buffer	3 x 3 min
Biotin block (Invitrogen 00-4303)	10 min
Rinse in washing buffer	3 x 3 min
HTI-601 (0.5 µg/ml) in blocking buffer	30 min
Rinse in washing buffer	3 x 3 min
HRP-streptavidin (BD biosciences 550946)	15 min
Rinse in washing buffer	3 x 3 min
Diaminobenzidine (DAB; Dako K3467)	4 min
Rinse in distilled water	2 min
Gill's III haematoxylin	1 min
Rinse in running tap water	5 min
1% acid alcohol (1% HCl in 70% ethanol)	3 sec
Rinse in running tap water	5 min
80% ethanol	30 sec
95% ethanol	30 sec
100% ethanol	2 min
Xylene	3 x 3 min
Xylene	Until ready to mount in DPX

Table 2.5: *Picrosirius red staining protocol.*

Reagent	Time
Xylene	5 min
Xylene	2 min
100% ethanol	2 min
90% ethanol	2 min
70% ethanol	2 min
Rinse in running tap water	2 min
Weigert's Haematoxylin (PRC/R/111 & 112)	8 min (5-15)
Running tap water	5 min
1% acid alcohol (1% HCl in 70% ethanol)	3 sec
Running tap water	5 min
Picrosirius Red (PRC/R/109)	1 hour
Acidified Water (0.5% acetic acid in distilled water)	2 changes of water
70% IMS/Ethanol	30 sec
90% IMS/Ethanol	30 sec
Absolute IMS/Ethanol	2 min
Xylene	2 min
Xylene	Until ready to mount in DPX

Table 2.6: *CD31 staining protocol to identify blood vessels.*

Reagent	Time
Xylene	5 min
Xylene	2 min
100% ethanol	2 min
90% ethanol	1 min
70% ethanol	1 min
Rinse in distilled water	5 min
Citrate buffer (Vector labs, H3300)	5 min in pressure cooker
Rinse in running tap water	5 min
TBS-tween (0.025% Tween 20 in TBS)	3 x 3 min
Peroxidase block (Dako, S200380)	10 min
TBS-tween	3 x 3 min
CD31 (Dianova DIA-310) 1:30 in Ab diluent (Dako S080981)	1 hour
TBS-tween	3 x 3 min
Rat histofine max PO (Nichirei bioscience, 414311F)	30 min
TBS-tween	3 x 3 min
Diaminobenzidine (DAB; Dako K3467)	6 min
TBS-tween	3 x 3 min
Gill's III haematoxylin	1 min
Rinse in running tap water	4 min
1% acid alcohol (1% HCl in 70% ethanol)	3 sec
Rinse in running tap water	5 min
70% ethanol	30 sec
90% ethanol	30 sec
100% ethanol	2 min
Xylene	2 x 2 min
Xylene	Until ready to mount in DPX

Whole-slide images were digitised using a Nanozoomer XR scanner (40x magnification, Hamamatsu). Nuclear density, HA (%) and blood vessel density were quantified from H&E, HTI-601, and CD31 staining respectively using Definiens Tissue Studio®. Collagen I & III (%), fractal dimension and entropy were quantified from picrosirius red staining by Dr Konstantinos Zormpas-Petridis as described previously[46]. Fractal dimension and entropy describe 2D collagen organisation[219].

2.9 Statistical analyses

Statistical analyses were performed using Prism 9 (GraphPad) and data are presented as mean ± 1 standard error of the mean (SEM). The mean was utilised as the summary statistic for cohort data as it was representative of the data and enabled use of an unpaired Student's *t*-test or a one-way ANOVA with multiple comparisons to identify significant differences with a significance level of 5%. Correlations were evaluated using the Pearson correlation coefficient (r) with a significance level of 5% and correlation matrices were created using Prism 9. In this thesis, p values were not corrected to minimise risk of type 1 error (incorrectly rejecting a true null hypothesis) because the sample sizes were relatively small, and making p value corrections, such as Bonferroni, will increase the chance of type II error (incorrectly accepting a false null hypothesis).

The within-subject test-retest coefficient of variation (CV_{WS}) for T_1, T_2, MTR, ADC, R_2*, G_d, G_l, |G*|, and Y was calculated from repeated 4T1, 4T1/HAS3 and MDA-MB-231 LM2-4 tumour MRI prior to and 24 hours after saline using:

$$CV_{WS}\,(\%) = 100 \times \sqrt{\frac{\Sigma\,(\Delta/m)^2}{2n}}$$

Where m is the mean of all the pre-saline and post-saline MRI, Δ is the difference between the paired repeats, and n is the number of pairs[220].

Chapter 3: Evaluating whether MRI relaxometry, magnetisation transfer (MT) imaging, and diffusion weighted imaging (DWI) can inform on breast tumour response to PEGPH20

3.1 Introduction:

The development of stromal modulatory therapies, such as PEGPH20, may be accelerated by imaging biomarkers which inform on therapeutic efficacy. HA degradation by PEGPH20 has been associated with a collapse of the extracellular space and a decrease in tumour water content[14, 49]. This reorganisation of previously HA-bound water molecules within the tumour microenvironment provides a strong rationale for using MRI, which exploits the magnetic moment of protons in tissue water, to assess response to PEGPH20 *in vivo*.

MR image acquisition can be sensitised to numerous independent contrast mechanisms, from which parametric maps can be calculated and used to inform on tumour structure and function *in situ*. This chapter summarises multiparametric MRI data, incorporating quantitation of tumour T_1, T_2, MTR, and ADC. Each of these MR characteristics is sensitive to tissue water content, organisation or mobility in a different way; T_1 to the proximity of nuclear spins to neighbouring molecules, T_2 to the distance between nuclear spins which *in vivo* predominantly come from water, MTR to the proportion of water bound to macromolecules and ADC to water diffusivity.

Firstly, the sensitivity of MRI biomarkers to ECM density was tested using gelatine phantoms of varying concentrations, used to replicate biological tissue with different degrees of stroma. Following this, multiparametric MRI was performed *in vivo* using pre-clinical breast tumours with different baseline HA accumulation which were predicted to exhibit different responses to PEGPH20. The aims were to gain mechanistic insight on PEGPH20 treatment, determine whether MRI can afford useful biomarkers

of tumour response to PEGPH20, and to understand if the MRI biomarkers are complementary in the information that they provide.

3.2 Results:

3.2.1 Multiparametric MRI of gelatine phantoms:

Multiparametric MRI examination of gelatine phantoms revealed decreased T_1, T_2, and ADC, and increased MTR, with increasing gelatine concentration. Representative anatomical T_2-weighted images and parameter maps from 6, 8, 10 and 12% gelatine phantoms are shown in Figure 3.1. Median values of T_1, T_2, MTR and ADC were calculated from a ROI drawn within the shimmed region of each homogeneous gelatine phantom. Median values of each parameter are presented in Figure 3.2; linear relationships were identified.

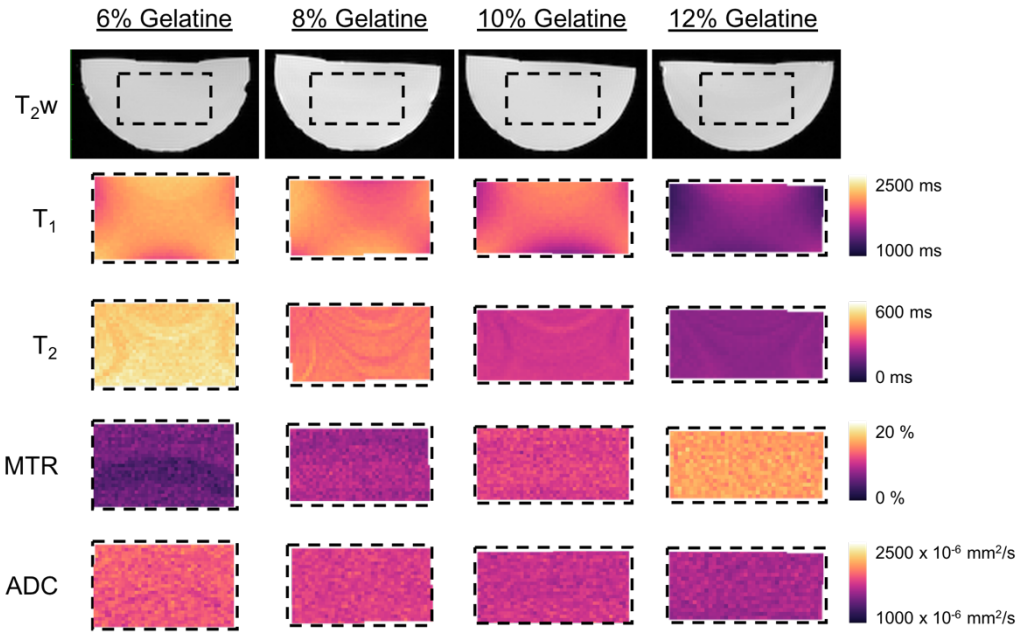

Figure 3.1: *Multiparametric MRI of gelatine phantoms. Representative T_1, T_2, MTR and ADC maps are shown, alongside anatomical T_2-weighted (T_2w) images, for gelatine phantoms with concentrations of 6, 8, 10 and 12% (w/w). For each phantom, a region of interest (ROI; black dashed rectangle) was drawn within the shimmed region to calculate median T_1, T_2, MTR and ADC values.*

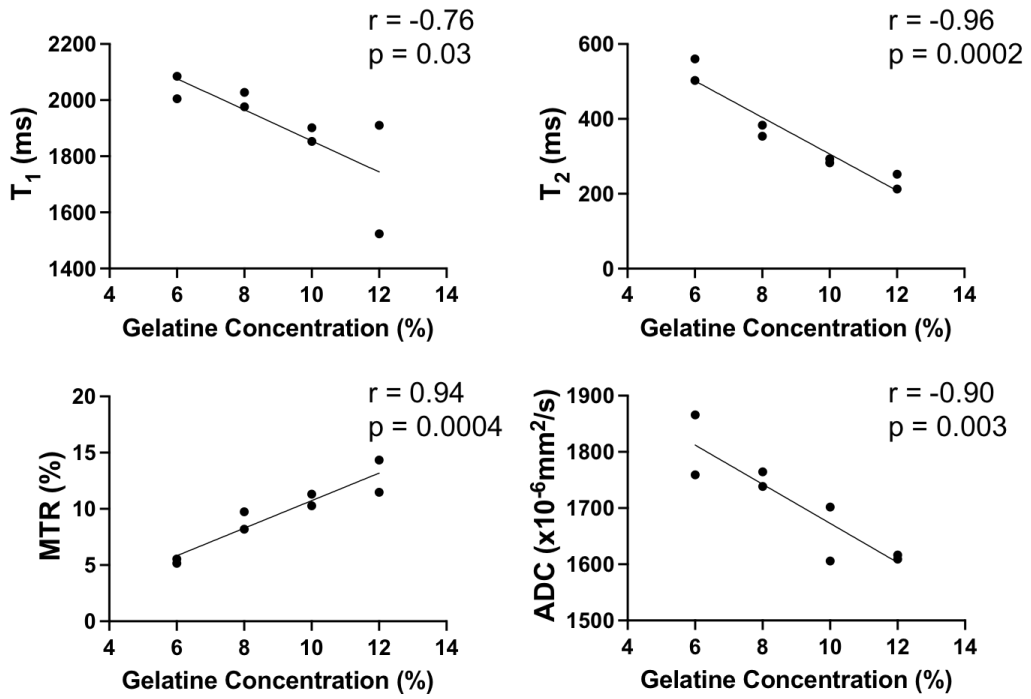

Figure 3.2: *Plots of T_1 (Pearson's correlation coefficient r = -0.76, p = 0.03), T_2 (r = -0.96, p = 0.0002), MTR (r = 0.94, p = 0.0004) and ADC (r = -0.90, p = 0.003) against gelatine phantom concentration (weight/weight percentage). Median values from each individual phantom are plotted (n = 2 for each concentration tested).*

3.2.2 Multiparametric MRI investigation of HA degradation by PEGPH20 in mouse models of breast cancer:

4T1, 4T1/HAS3 and MDA-MB-231 LM2-4 tumours grew rapidly, with an average doubling time of 2.6 days, 2.4 days and 4.3 days respectively (Figure 3.3). All 4T1 and 4T1/HAS3 tumours were measurable 9 days after injection of cells into the mammary fat pad. MDA-MB-231 LM2-4 tumours were slightly more variable in the time taken to become established, with tumours measurable between day 5 and 16 after injection.

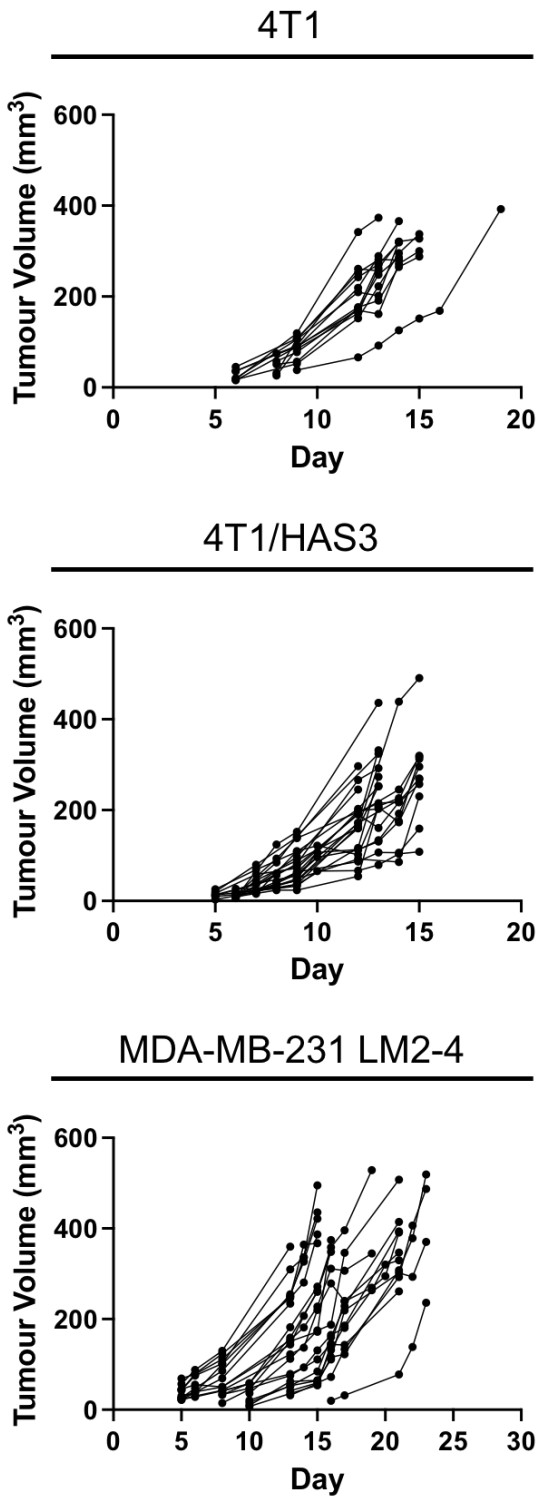

Figure 3.3: *4T1, 4T1/HAS3 and MDA-MB-231 LM2-4 tumour growth. Here tumour volume was measured using callipers. Each black line connects the data points from each individual tumour (4T1 n = 13, 4T1/HAS3 n = 23, and MDA-MB-231 LM2-4 n = 23). Tumour volume is shown up until the day of pre-treatment MRI. The doubling times for 4T1, 4T1/HAS3 and MDA-MB-231 LM2-4 tumours were 2.6 days, 2.4 days and 4.3 days respectively.*

Multiparametric MRI examination of 4T1, 4T1/HAS3 and MDA-MB-231 LM2-4 tumours yielded anatomical T_2-weighted images and T_1, T_2, MTR and ADC parameter maps. Representative MRI for 4T1, 4T1/HAS3 and MDA-MB-231 LM2-4 tumours treated with either saline or PEGPH20 are shown in Figures 3.4 and 3.5 respectively; one tumour (pre and post-saline or PEGPH20) is shown per tumour model. Parametric maps of T_1, T_2, MTR and ADC revealed that PEGPH20-induced changes occurred homogeneously across viable tumour regions.

Within-subject test-retest coefficients of variation (albeit, with a change in tumour volume), determined from the pre- and 24 hours post-saline data for all 4T1, 4T1/HAS3 and MDA-MB-231 LM2-4 tumours, were 2.2, 6.6, 5.0, and 15.7% for T_1, T_2, MTR and ADC respectively.

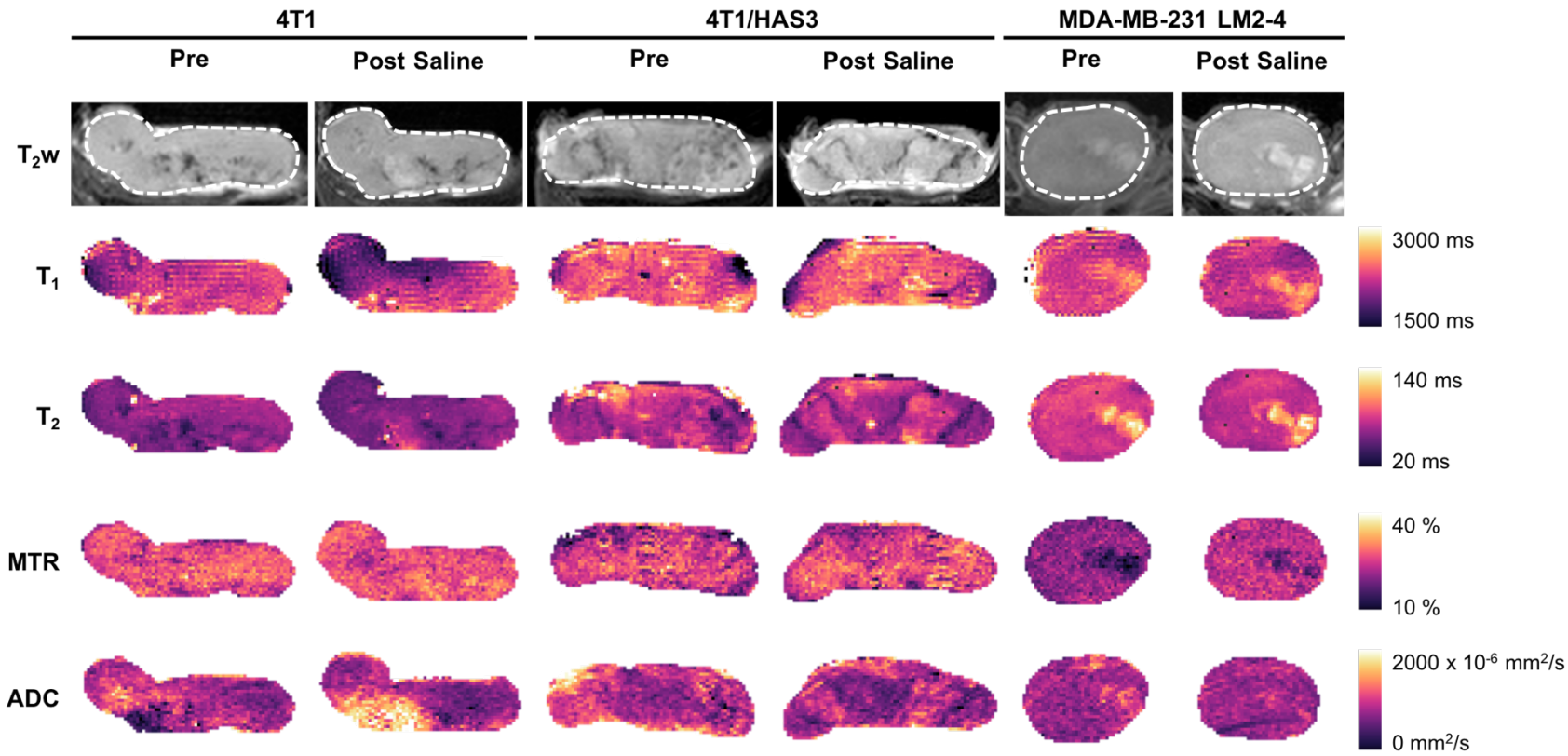

Figure 3.4: *Anatomical T_2-weighted (T_2w) MRI and parameter maps of T_1, T_2, MTR and ADC, for a representative 4T1, 4T1/HAS3 and MDA-MB-231 LM2-4 tumour prior to and 24 hours after saline. The tumour ROI from which necrosis was excluded is shown by a white dashed line on the T_2-weighted images. The artefact on the 4T1 tumour ADC parametric maps was excluded from quantitative analyses.*

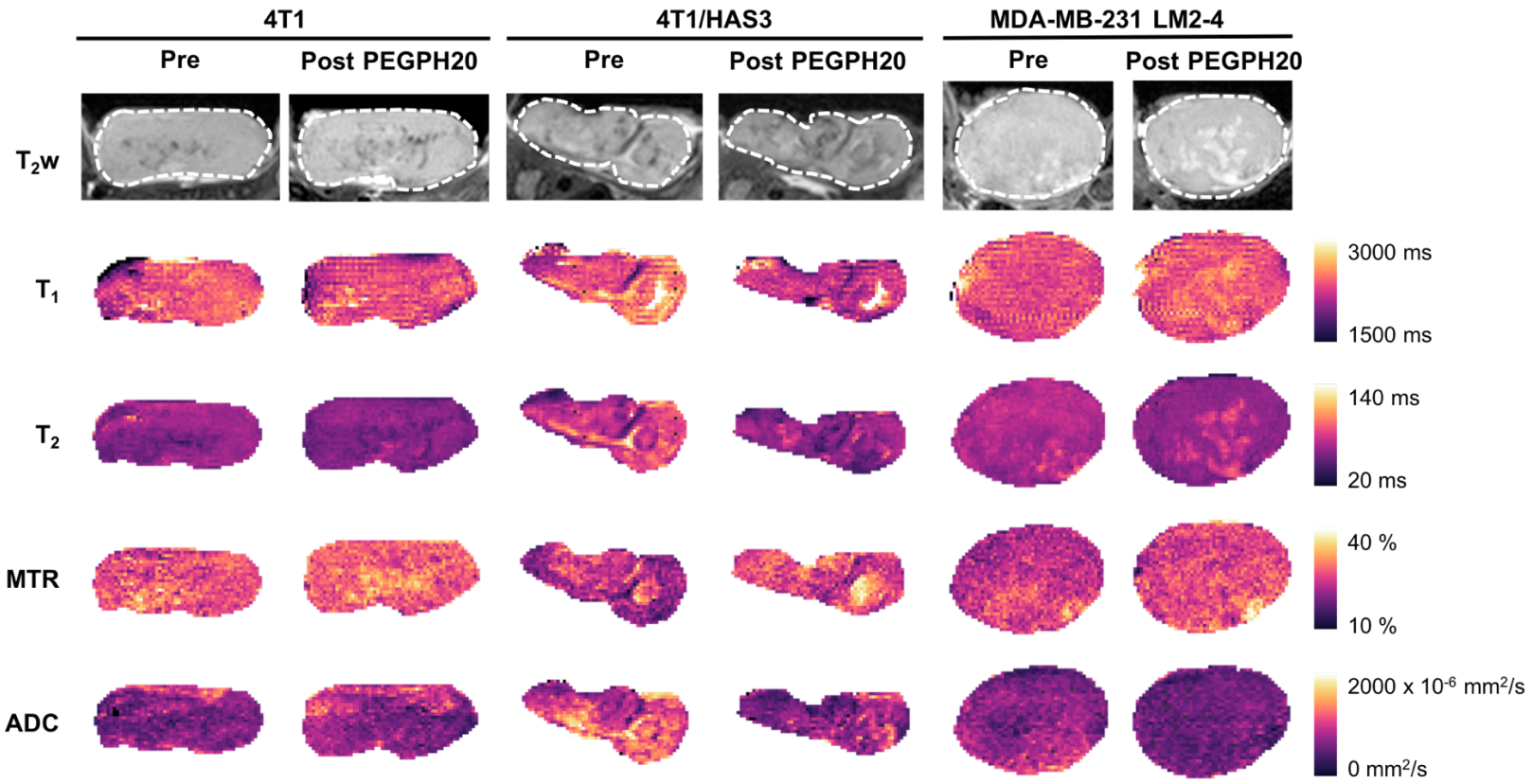

Figure 3.5: *Anatomical T_2-weighted (T_2w) MRI and parameter maps of T_1, T_2, MTR and ADC, for a representative 4T1, 4T1/HAS3 and MDA-MB-231 LM2-4 tumour prior to and 24 hours after PEGPH20 treatment (1 mg/kg). The tumour ROI from which necrosis was excluded is shown by a white dashed line on the T_2-weighted images.*

MRI-derived tumour volume and median values of T_1, T_2, ADC and MTR are plotted in Figure 3.6. Percentage change values for MRI-derived tumour volume, T_1, T_2, ADC and MTR following saline or PEGPH20 treatment are shown in Figure 3.7.

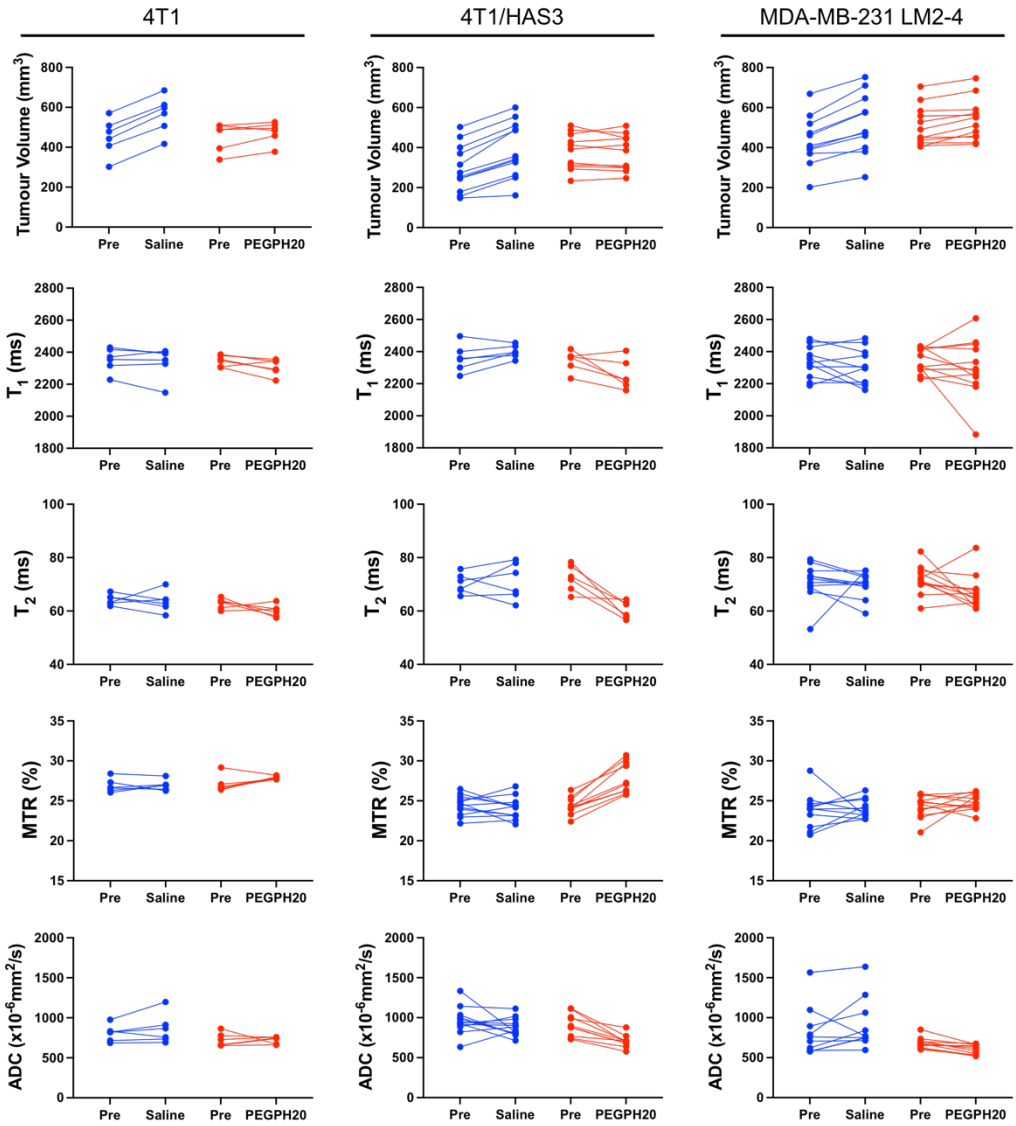

Figure 3.6: *MRI-derived tumour volume and median T_1, T_2, MTR and ADC for 4T1, 4T1/HAS3 and MDA-MB-231 LM2-4 tumours pre-saline, post-saline, pre-PEGPH20 and post-PEGPH20 (1 mg/kg). Data from each individual tumour are plotted, with saline controls in blue and PEGPH20 treated tumours in red. Sample sizes for 4T1, 4T1/HAS3 and MDA-MB-231 LM2-4 tumours were: n = 6 saline and n = 6 PEGPH20; n = 12 saline and n = 11 PEGPH20; and n = 11 saline and n = 12 PEGPH20 respectively.*

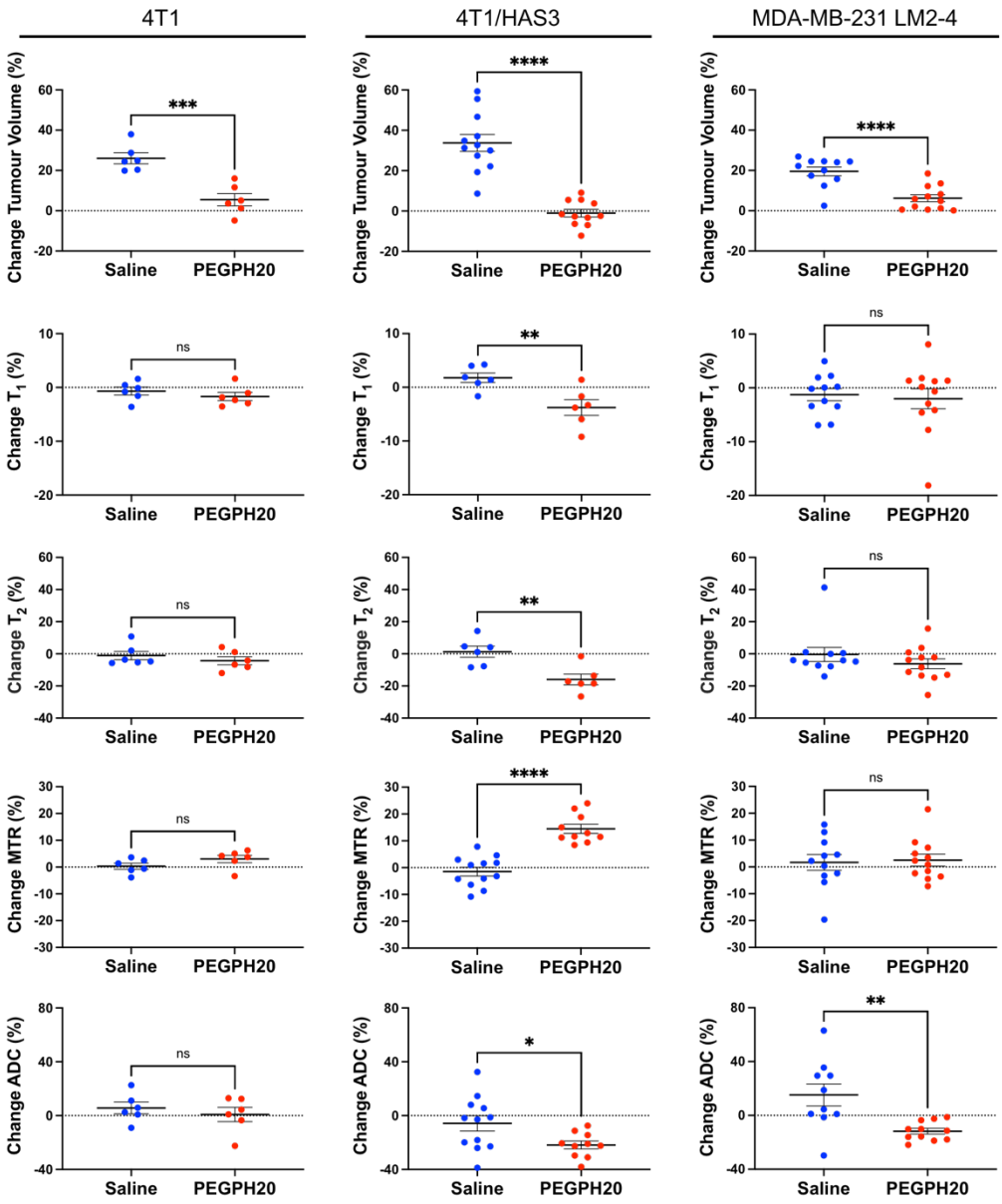

Figure 3.7: *Percentage change in MRI-derived tumour volume, T_1, T_2, MTR, and ADC between pre- and post-treatment MRI for saline and PEGPH20 treated mice bearing 4T1, 4T1/HAS3 or MDA-MB-231 LM2-4 tumours. PEGPH20 reduced the growth of 4T1 (***p=0.0005, unpaired Student's t-test), 4T1/HAS3 (****p<0.0001) and MDA-MB-231 LM2-4 (****p<0.0001) tumours. PEGPH20 treatment did not significantly change T_1, T_2, MTR and ADC in 4T1 tumours (ns; p>0.05). PEGPH20 reduced T_1 (**p=0.01), T_2 (**p=0.005), and ADC (*p=0.03), and increased MTR (****p<0.0001) in 4T1/HAS3 tumours. PEGPH20 treatment of MDA-MB-231 LM2-4 tumours decreased ADC (**p=0.003) but no significant change was seen in T_1, T_2 or MTR (ns; p>0.05). Data points are each individual tumour and are summarised by the cohort mean ± 1 SEM.*

PEGPH20 treatment significantly reduced the growth of 4T1, 4T1/HAS3 and MDA-MB-231 LM2-4 orthotopic breast tumours (Figures 3.6 & 3.7). 4T1/HAS3 tumours had the fastest growth rate with saline control tumour volume, measured using T_2-weighted MRI, increasing 34% from 296 ± 33 mm^3 to 390 ± 39 mm^3 in 24 hours. PEGPH20 treated 4T1/HAS3 tumour volume decreased by 1% from 379 ± 27 mm^3 to 374 ± 27 mm^3. Saline control 4T1 tumour volume increased 26% from 452 ± 38 mm^3 to 565 ± 38 mm^3, whilst PEGPH20 treated 4T1 tumour volume increased 5% from 454 ± 29 mm^3 to 476 ± 22 mm^3. MDA-MB-231 LM2-4 tumours exhibited the slowest growth rate, with saline control tumour volume increasing by 20% from 434 ± 36 mm^3 to 518 ± 45 mm^3. PEGPH20 treated MDA-MB-231 LM2-4 tumour volume increased by 6% from 507 ± 28 mm^3 to 537 ± 29 mm^3.

PEGPH20 treatment significantly increased MTR, and significantly reduced T_1, T_2, and ADC in 4T1/HAS3 tumours (Figures 3.5, 3.6 & 3.7). PEGPH20 treatment of MDA-MB-231 LM2-4 tumours significantly decreased ADC. Although not significant, similar trends of decreased T_1 and T_2, and increased MTR, were seen in PEGPH20 treated MDA-MB-231 LM2-4 tumours. PEGPH20 treatment did not significantly change T_1, T_2, MTR and ADC in 4T1 tumours, however the trends of increased MTR and reduced T_1, T_2, and ADC were consistent with the other breast tumour models.

3.2.3 Effect of PEGPH20 on tumour pressure (*in vivo*) and water content (*ex vivo*):

The interstitial fluid pressure (IFP), solid stress (SS) and total tissue pressure (TTP) of PEGPH20 treated tumours were not significantly different to saline controls in any tumour model (Figure 3.8). However, there was a trend to lower IFP in PEGPH20 treated 4T1/HAS3 and MDA-MB-231 LM2-4 tumours. 4T1/HAS3 tumours treated with PEGPH20 had lower IFP (5.2 ± 2.0 mmHg) compared to saline controls (9.4 ± 1.3 mmHg; $p = 0.08$). MDA-MB-231 LM2-4 tumours had the highest IFP, with an average saline control tumour IFP of 11.5 ± 1.8 mmHg. PEGPH20 treated MDA-MB-231 LM2-4 tumour IFP was lower (7.4 ± 1.0 mmHg; $p = 0.06$). There was also a trend to lower TTP in PEGPH20 treated 4T1 and 4T1/HAS3 tumours ($p = 0.06$ and $p = 0.09$ respectively).

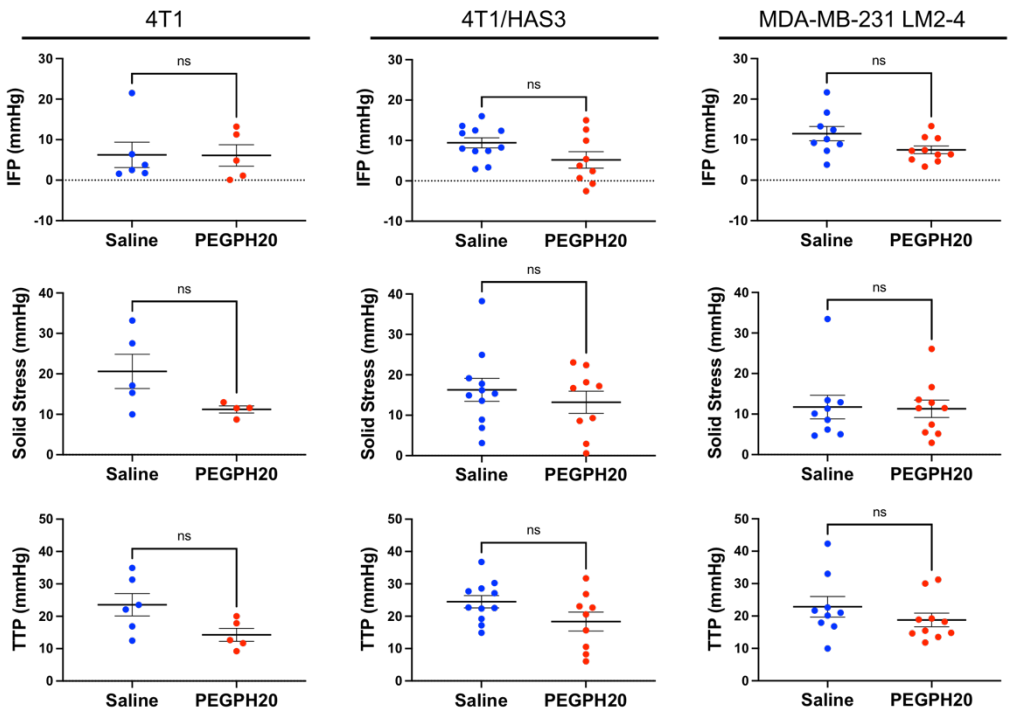

Figure 3.8: *Measurements of IFP, SS and TTP in 4T1, 4T1/HAS3 and MDA-MB-231 LM2-4 tumours 24 hours after treatment with either saline (blue) or PEGPH20 (red). These invasive pressure measurements were taken following the post-treatment MRI from one region within the centre of each tumour. PEGPH20 treated tumours did not have significantly different IFP, SS or TTP compared to saline controls in any of the three breast tumour models (ns; p>0.05). A trend to lower IFP in PEGPH20 treated 4T1/HAS3 and MDA-MB-231 LM2-4 tumours was apparent (p = 0.08 and p = 0.06 respectively). There was also a trend to lower TTP in PEGPH20 treated 4T1 and 4T1/HAS3 tumours (p = 0.06 and p = 0.09 respectively). Each data point is from an individual tumour and these are summarised by the cohort mean ± 1 SEM.*

MDA-MB-231 LM2-4 tumours treated with PEGPH20 had significantly lower water content (82.6 ± 0.2 %) compared to saline controls (84.1 ± 0.3 %; p = 0.001; Figure 3.9). The same trend towards decreased water content in PEGPH20 treated tumours was apparent in 4T1 and 4T1/HAS3 tumours but was not statistically significant. 4T1 tumour water content was 81.6 ± 0.5% in saline controls compared to 80.3 ± 0.6% in PEGPH20 treated tumours (p = 0.12). 4T1/HAS3 tumour water content was 81.2 ± 0.9% for saline controls and 80.0 ± 0.5% following PEGPH20 treatment (p = 0.27).

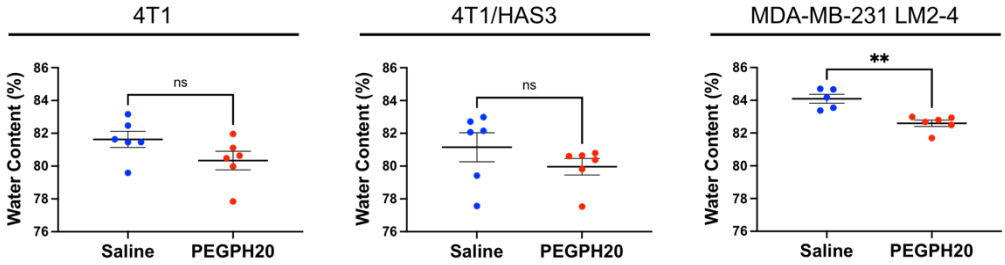

Figure 3.9: *Water content of 4T1, 4T1/HAS3 and MDA-MB-231 LM2-4 tumours 24 hours after treatment with either saline (blue) or PEGPH20 (red). Water content was measured ex vivo from one half of each tumour following post-treatment MRI and tumour pressure measurements. PEGPH20 treated MDA-MB-231 LM2-4 tumours had lower water content than saline control tumours (**p = 0.001). A trend to decreased water content in PEGPH20 treated 4T1 and 4T1/HAS3 tumours was apparent (p = 0.12 and p = 0.27 respectively). Each point is from an individual tumour and data are summarised by the cohort mean ± 1 SEM.*

3.2.4 Histological evaluation of pre-clinical breast tumours treated with PEGPH20:

Representative post-treatment anatomical T_2-weighted images and digitised images of aligned H&E, HTI-601 (HA) and picrosirius red stained sections are shown in Figure 3.10. There is clear spatial correspondence between the MRI and histology despite the difficulties associated with, and inaccuracies inherent in, the simple *in vivo* imaging to histology registration methods employed. Figure 3.11 shows the quantification of the histological staining. There was a non-significant increase in nuclear density, quantified from H&E staining, in 4T1, 4T1/HAS3 and MDA-MB-231 LM2-4 tumours treated with PEGPH20 compared to saline controls ($p > 0.05$, one-way ANOVA with multiple comparisons). HTI-601 staining of saline control tumours showed that 4T1/HAS3 tumours had the greatest HA accumulation (55 ± 2 %) compared to 4T1 (39 ± 1 %) and MDA-MB-231 LM2-4 (31 ± 3 %) tumours. In all three models, HA accumulation was markedly lower in PEGPH20 treated tumours (all $p < 0.0001$; 4T1 0.3 ± 0.1 %, 4T1/HAS3 1.2 ± 0.3 % and MDA-MB-231 LM2-4 0.8 ± 0.2 %). Saline control data suggested that MDA-MB-231 LM2-4 tumours had lower collagen accumulation than 4T1 ($p = 0.003$) and 4T1/HAS3 ($p = 0.02$) tumours. A few PEGPH20 treated tumours from each model had greater collagen accumulation than saline controls, particularly in the MDA-MB-231 LM2-4 cohort, however this was not significant overall ($p > 0.05$ in all comparisons).

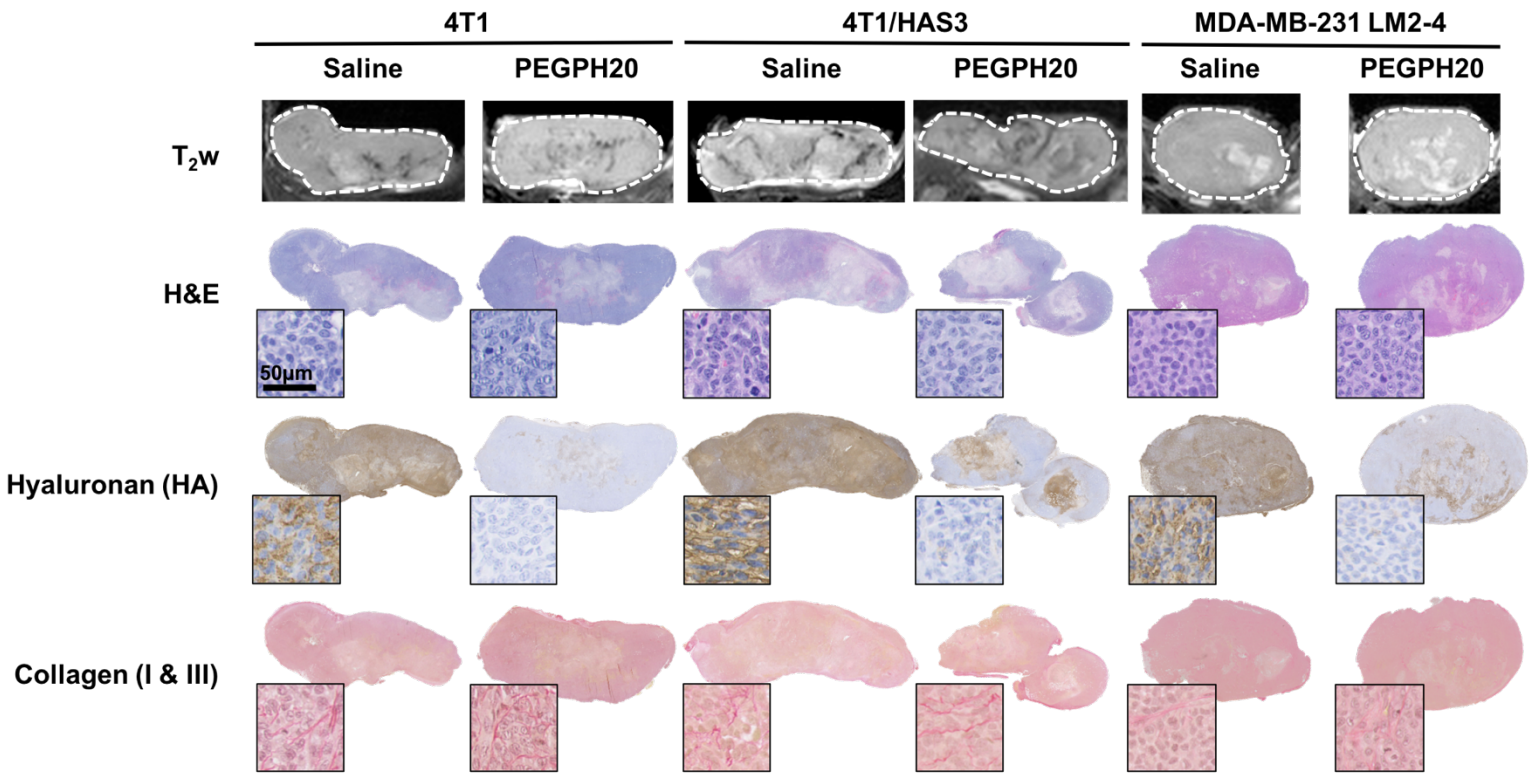

Figure 3.10: *T_2-weighted (T_2w) MRI alongside aligned 4T1, 4T1/HAS3 and MDA-MB-231 LM2-4 tumour tissue sections (5 μm) stained with H&E, HTI-601 (HA), or picrosirius red (collagen I & III). Representative magnified images (20x) are presented alongside whole tumour section images for one saline control and one PEGPH20 treated tumour per in vivo model. Histology sections were closely spatially matched to the MRI.*

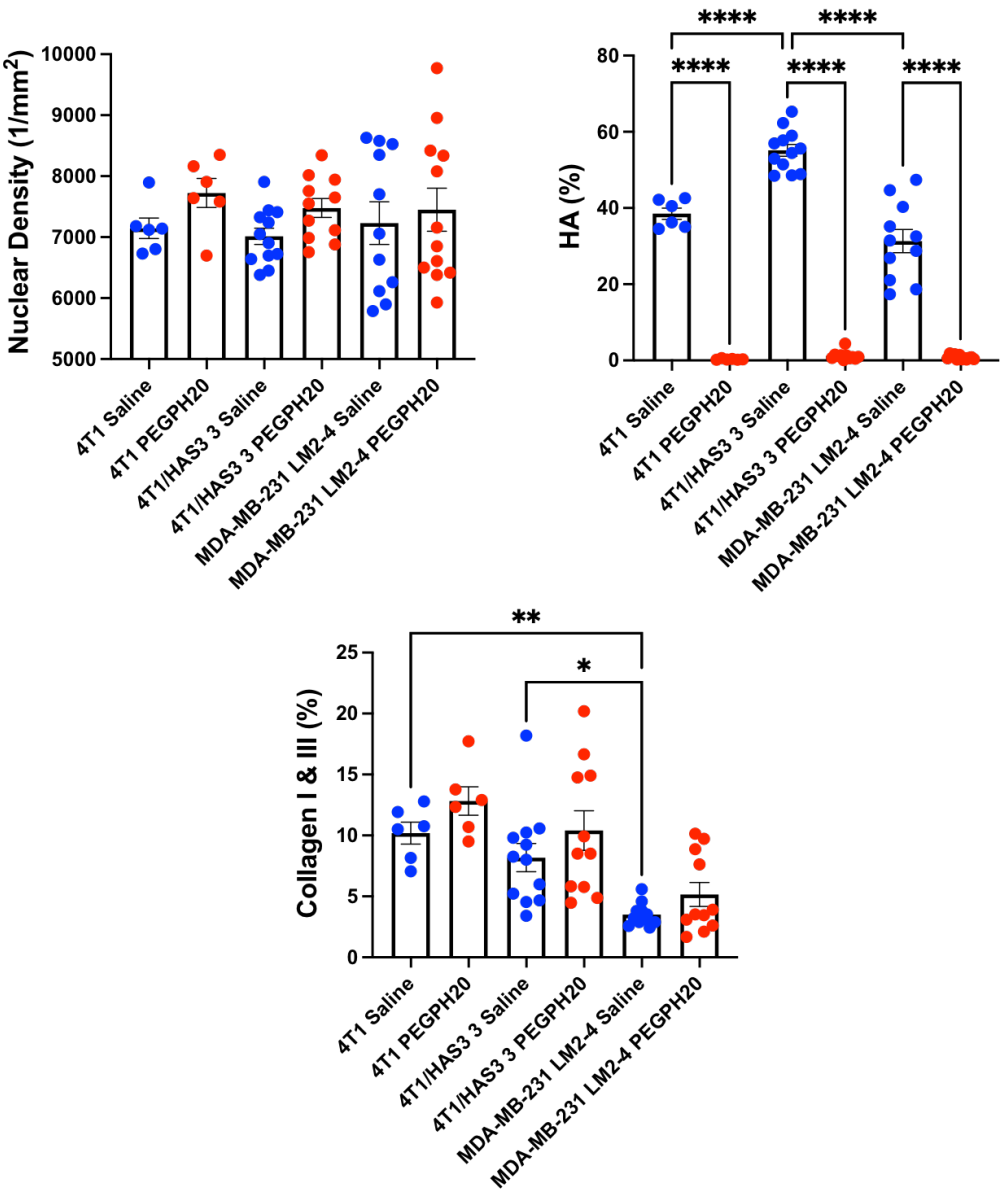

Figure 3.11: *Quantification of nuclear density, HA (%) and collagen I & III (%) from H&E, HTI-601 and picrosirius red staining. Quantification of HTI-601 staining revealed different baseline HA accumulation in 4T1, 4T1/HAS3 and MDA-MB-231 LM2-4 tumours and marked HA reduction in all models with PEGPH20 treatment (****p < 0.0001). Saline treated MDA-MB-231 LM2-4 tumours had significantly less collagen deposition compared to 4T1 (**p = 0.003) and 4T1/HAS3 (*p = 0.02) tumours.*

3.3 Discussion:

Multiparametric MRI assessment of gelatine phantoms of differing concentrations demonstrated the sensitivity of T_1, T_2, MTR, and ADC to ECM density. The increased MTR and decrease in T_1, T_2, and ADC, suggest more bound water and restricted diffusion with increasing gelatine concentration. Previous studies have also shown a lower ADC and higher MTR with increasing gelatine concentration[221, 222]. Some artefacts were apparent, firstly, darker regions coming in from the sides and bottom of the rectangular ROI resulted from areas of phantom just outside the ROI which were not able to be shimmed, and secondly, some horizonal line artefacts particularly visible in the MTR of the 6% gelatine phantom occurred due to a slight compression of the phantom by the MRE piston positioned above. Use of the median value minimised the effect of these artefacts.

Having established this, the ability of multiparametric MRI to inform on PEGPH20 response was assessed *in vivo*. PEGPH20 treatment inhibited the growth of 4T1, 4T1/HAS3 and MDA-MB-231 LM2-4 tumours, consistent with previous pre-clinical tumour data from prostate, lung and pancreatic cancer models[14, 223, 224]. This is likely to have resulted from collapse of the HA-assembled gel-fluid matrix, breakdown of surrounding tumour architecture, and depletion of soluble growth factors in the extracellular space[14, 224]. In future, assessing the impact of PEGPH20 treatment on Ki67 staining or dynamic ^{18}F-Fluorothymidine (FLT)-positron emission tomography (PET) imaging would clarify whether the reduced tumour growth is also associated with inhibition of tumour cell proliferation[225].

Assessment of T_1 both pre-clinically and in a small number of clinical trials suggests that a reduction in T_1 is indicative of effective treatment response in various tumour types[168-172, 226, 227]. Here, PEGPH20 reduced T_1 and T_2 in 4T1/HAS3 tumours. A non-significant decrease in T_1 and T_2 was also seen in 4T1 and MDA-MB-231 LM2-4 tumours. A reduction in T_1 and T_2 is consistent with HA degradation, leading to reorganisation of water

molecules, and loss of water from the tumour mass seen herein, and reported in other tumour models[14, 49].

MTR informs on the proportion of water bound to macromolecules. MTR is sensitive to ECM composition, as evidenced by correlations with fibrosis in pre-clinical models of pancreatic cancer, and collagen content in patient meningiomas[173-175]. PEGPH20 treatment increased MTR in 4T1/HAS3 tumours. A non-significant increase in MTR was seen in 4T1 and MDA-MB-231 LM2-4 tumours. HA-mediated fluid retention and expansion of the extracellular space with increasing HA accumulation may suppress the effects of MT-inducing components such as collagen. Once HA is degraded by PEGPH20, the effects of MT-inducing components are no longer attenuated, likely resulting in a higher MTR value.

ADC is sensitive to the mobility of water molecules, and can inform upon various phenomena including the presence of macromolecules, permeability of cell membranes, the characteristic sizes of water-filled extracellular spaces, and the equilibrium between intracellular and extracellular water[150]. Solid tumours commonly have restricted diffusion compared to normal tissues due to increased cellularity and reduction in extracellular space[156]. An increase in ADC typically indicates treatment response in solid tumours and is often associated with tumour cell death[171, 181, 182, 228]. Following PEGPH20 treatment, ADC decreased in 4T1/HAS3 and MDA-MB-231 LM2-4 tumours. A small, non-significant decrease in ADC was seen in 4T1 tumours following PEGPH20. A decrease in ADC following PEGPH20 could have resulted from a loss of water from the tumour mass and restriction of water diffusion via collapse of the extracellular space. Another study in normal brain showed that a small change in tissue water content (~1%) is sufficient to alter ADC by approximately 10%[229].

A dense ECM can increase solid stress, elevate IFP, impede drug delivery and promote breast tumour progression and metastasis[2, 18, 72]. Previous studies have reported that degradation of HA with PEGPH20 can reduce

IFP, and suggest this is associated with improved drug delivery and tumour response to therapy[14, 15, 49, 215, 230]. In our study, there was a non-significant trend of lower IFP and TTP in PEGPH20 treated 4T1/HAS3 and MDA-MB-231 LM2-4 tumours compared to saline controls. No such difference was seen in 4T1 tumours. My ability to detect a significant change in IFP may have been limited because the invasiveness of the measurement method made it undesirable to acquire pre-treatment data and differences between groups were difficult to detect given the small sample sizes and the relatively high variability of the IFP measurement.

HA avidly binds water and its degradation by PEGPH20 has previously been shown to decrease tumour water content[14, 49]. In this study, PEGPH20 treated tumours had lower water content compared to saline control tumours, although this was only significant in MDA-MB-231 LM2-4 tumours. As shown throughout this chapter, MRI can provide biomarkers that can detect PEGPH20 response, particularly in tumours like 4T1/HAS3 with high baseline HA accumulation. The change in tumour water content, structure and mobility following PEGPH20 likely underpins why the response to PEGPH20 can be visualised with MRI[14, 49]. Whilst tumour IFP and blood vessel lumen area return to pre-treatment values relatively quickly (~48 hours) following PEGPH20 treatment *in vivo*, the significant reduction in tumour water content is sustained for at least 120 hours[14]. Therefore, probing characteristics of tumour water may provide the most long-lasting information when evaluating PEGPH20 response in the clinic.

Histologically stained tissue sections, matched approximately to the MRI slice, confirmed that PEGPH20 effectively degraded HA in 4T1, 4T1/HAS3 and MDA-MB-231 LM2-4 tumours. 4T1/HAS3 tumours had a higher baseline HA accumulation compared to 4T1 and MDA-MB-231 LM2-4 tumours, suggesting that degrading 4T1 and MDA-MB-231 LM2-4 tumour HA with PEGPH20 may induce reorganisation of fewer water molecules, a smaller decrease in tumour water content, and collapse of a smaller volume of the extracellular space, than for 4T1/HAS3 tumours. This may explain why fewer MRI biomarkers changed significantly following

PEGPH20 treatment in 4T1 and MDA-MB-231 LM2-4 tumours. ADC was able to detect the subtle response to PEGPH20 in MDA-MB-231 LM2-4 tumours, suggesting that DWI affords the most sensitive biomarker of PEGPH20 response. Further work should evaluate if a decrease in ADC remains when PEGPH20 is combined with chemo-, radio- or immunotherapy, treatments that typically result in tumour cell death and hence an increase in ADC.

Chapter 4: MR elastography (MRE) reveals that HA degradation by PEGPH20 can increase breast tumour viscoelastic properties

4.1 Introduction:

Malignant solid tumours, particularly those like breast with a dense stromal component, are often stiffer than the surrounding healthy tissue and benign lesions[74, 188, 195]. Increased stiffness is associated with inefficient drug delivery, tumour progression and metastasis[16, 231, 232].

MRE can non-invasively map and quantify tumour viscoelastic properties *in vivo*[187, 188]. Periodic application of an appropriate force generates shear waves which propagate through tissue with a speed that depends on the shear elastic modulus of the tissue and are attenuated at a rate that depends on the shear viscous modulus of the tissue. Imaging the resulting tissue shear deformation as a function of time and position can infer, under certain simplifying assumptions, the viscoelastic properties of the tissue[184, 185]. MRE yields quantitative images called elastograms, which map the shear elasticity modulus (G_d kPa) and shear viscosity modulus (G_l kPa), from which one can calculate the absolute value of the complex shear modulus ($|G^*| = \sqrt{[G_d^2+G_l^2]}$ kPa) and normalised phase angle ($Y = 2/\pi[\tan^{-1}[G_l/G_d]]$)[159].

MRE has been used in diagnosis to differentiate between benign and malignant lesions, and help define the boundary between solid tumour and surrounding healthy tissue[74, 188, 195]. In addition, MRE can inform on tumour response to therapy, with effective treatment and tumour cell death often resulting in a decrease in tumour stiffness[74, 157, 198].

As mentioned previously, ECM components including HA and collagen often accumulate in the breast tumour microenvironment. MRE has been shown to inform on breast tumour response to collagen degradation, with

a decrease in stiffness seen after treatment with collagenase[46]. HA degradation by PEGPH20 is associated with a collapse of the extracellular space[14, 49]. This biomechanical response may impact tumour viscoelasticity, providing a strong rationale to use MRE to assess tumour response to PEGPH20. MRE was performed alongside the MRI biomarkers described in Chapter 3 (T_1, T_2, ADC and MTR) and Chapter 5 (R_2*), before and after treatment with either saline or PEGPH20, in 4T1, 4T1/HAS3 and MDA-MB-231 LM2-4 breast tumours. This chapter summarises the results from MRE in isolation and compares the *in vivo* data with collagen content and organisation quantified from histology.

4.2 Results:

4.2.1. MRE of gelatine phantoms

MRE examination of gelatine phantoms revealed increased G_d, G_l, |G*|, and Y with increasing gelatine concentration. Representative anatomical T_2-weighted images and parameter maps from 6%, 8%, 10% and 12% gelatine phantoms are shown in Figure 4.1. Median values of G_d, G_l, |G*| and Y were calculated from a ROI drawn within the shimmed region of each homogeneous gelatine phantom. Median values of each parameter are presented in Figure 4.2 and the linear relationships that fit the data best were established.

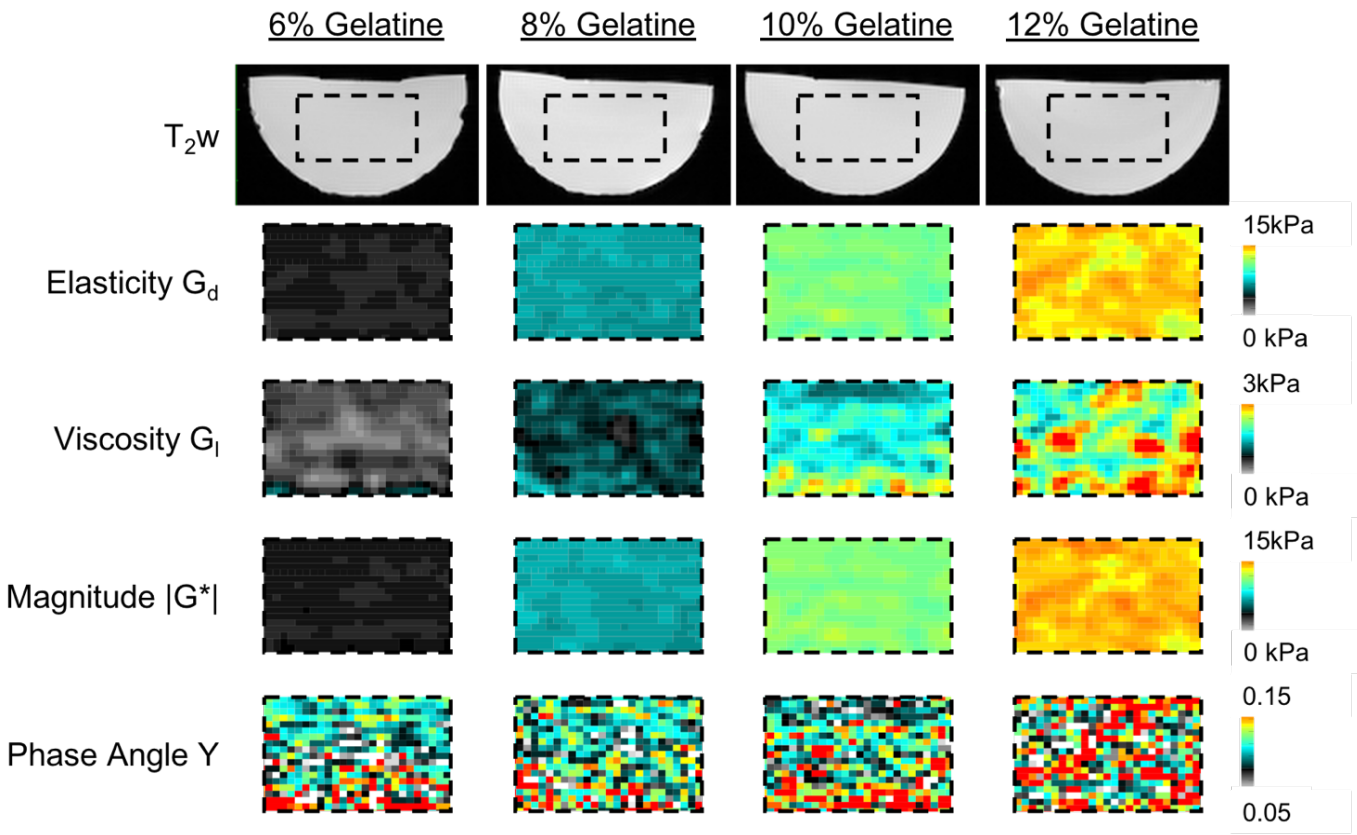

Figure 4.1: *Evaluation of gelatine phantoms with MRE. Representative G_d, G_l, $|G^*|$, and Y maps are shown, alongside anatomical T_2-weighted (T_2w) images, for gelatine phantoms with concentrations of 6, 8, 10 and 12% (w/w). For each phantom, a ROI (black dashed rectangle) was drawn within the shimmed region to calculate median values of G_d, G_l, $|G^*|$, and Y.*

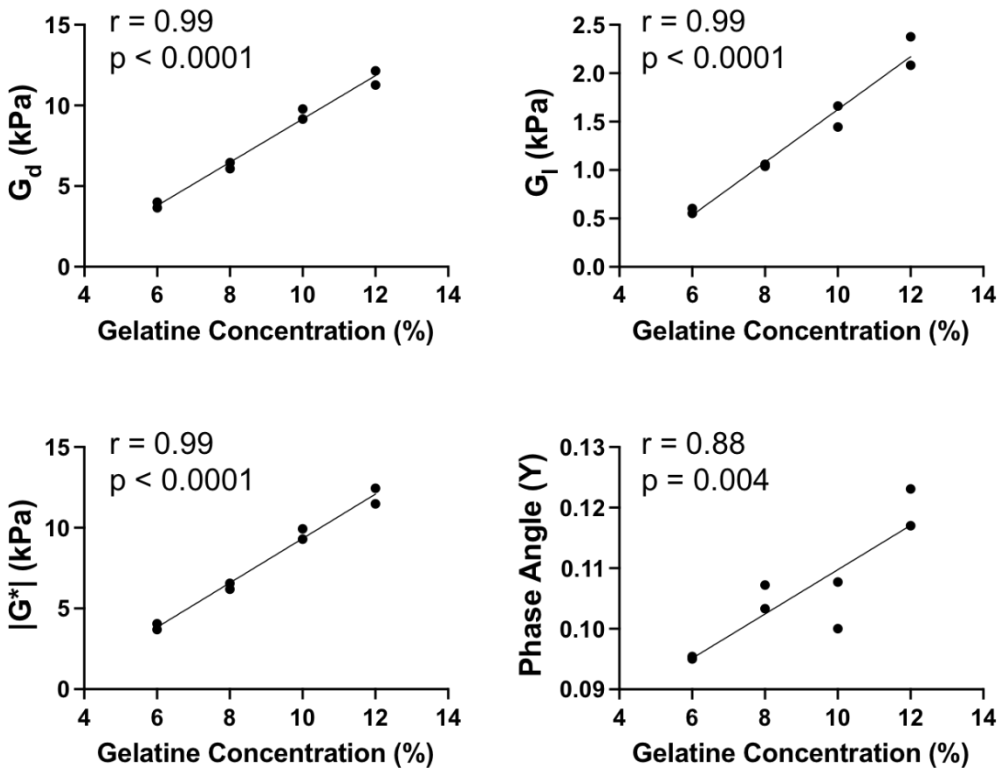

Figure 4.2: *Plots of elasticity (G_d; Pearson's correlation coefficient r = 0.99, p < 0.0001), viscosity (G_l; r = 0.99, p < 0.0001), the absolute value of the complex shear modulus (|G*|; r = 0.99, p < 0.0001) and phase angle (Y; r = 0.88, p = 0.004) against gelatine phantom concentration (weight/weight percentage). Median values from each individual phantom are plotted (n = 2 for each gelatine concentration tested).*

4.2.2 Evaluating the impact of HA degradation on breast tumour viscoelasticity using MRE

MRE was performed alongside the multiparametric MRI described in Chapters 3 and 5 on the same 4T1, 4T1/HAS3 and MDA-MB-231 LM2-4 tumours. MRE yielded parametric maps of G_d, G_l, $|G^*|$, and Y. Representative images for one 4T1, 4T1/HAS3, and MDA-MB-231 LM2-4 tumour before and 24 hours after treatment with either saline or PEGPH20 are shown in Figures 4.3 and 4.4 respectively.

At baseline, G_d, G_l, $|G^*|$ and Y were all heterogeneously distributed within 4T1, 4T1/HAS3 and MDA-MB-231 LM2-4 tumours. There was no change in G_d, G_l, $|G^*|$ and Y following saline in any of the tumour models (Figure 4.3). Following HA degradation by PEGPH20, G_d, G_l and $|G^*|$ increased in a fairly homogeneous manner in MDA-MB-231 LM2-4 tumours, with the only exception being no apparent change in necrotic regions where tumour viscoelastic properties remained low (Figure 4.4). There was no visible PEGPH20-induced change in G_d, G_l, or $|G^*|$ in 4T1 and 4T1/HAS3 tumours, nor in Y for any tumour model.

Median values of G_d, G_l, $|G^*|$, and Y are plotted in Figures 4.5 and 4.6, with the former comparing pre-treatment values between the different tumour models and the latter showing all values before and after treatment with either saline or PEGPH20. Percentage change values for G_d, G_l, $|G^*|$, and Y following saline or PEGPH20 treatment are shown in Figure 4.7.

Within-subject test-retest coefficients of variation, determined from the pre- and post-saline data for all 4T1, 4T1/HAS3 and MDA-MB-231 LM2-4 tumours, were 13.0%, 16.1%, 13.5% and 9.5% for G_d, G_l, $|G^*|$, and Y respectively.

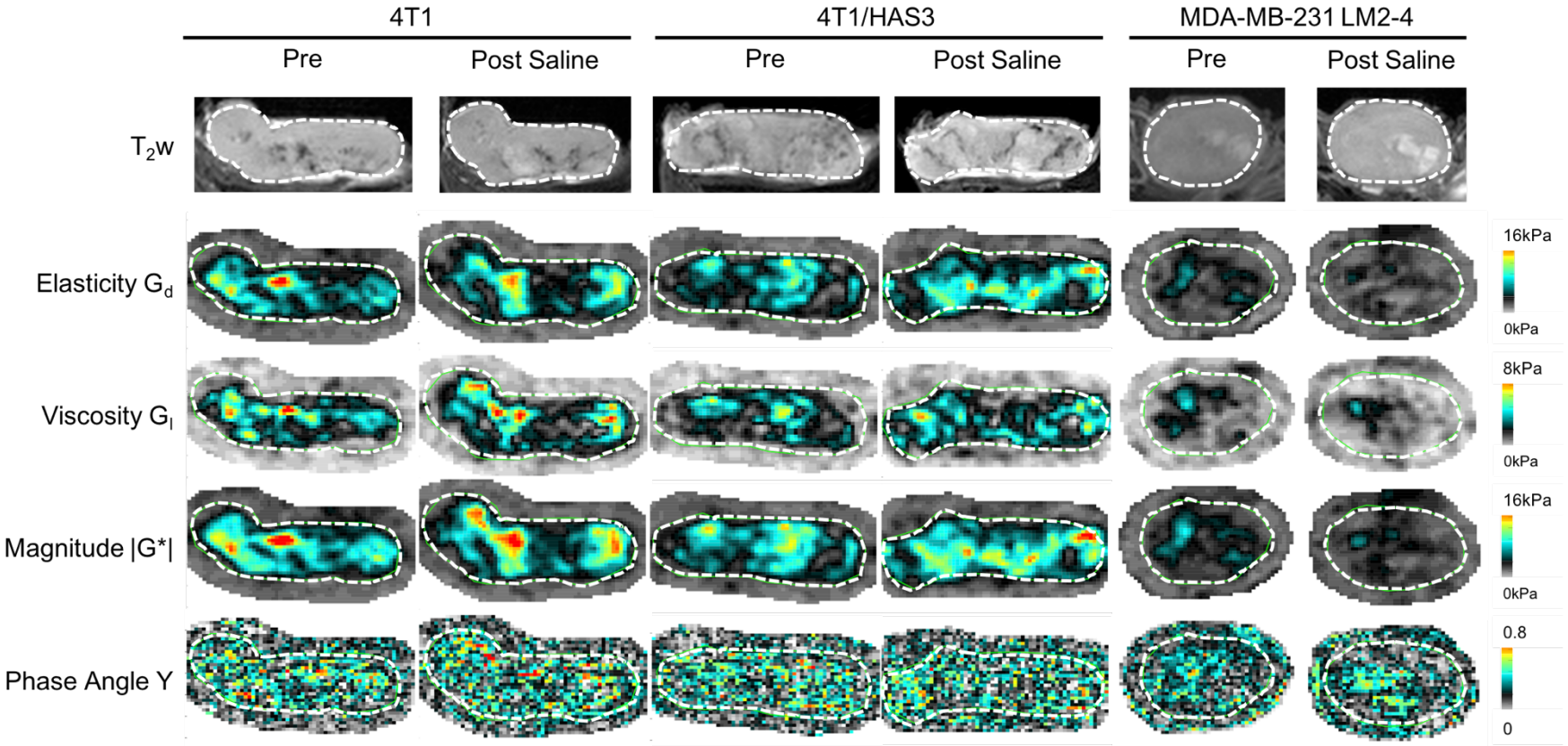

Figure 4.3: *Anatomical T_2-weighted (T_2w) MRI and parameter maps of G_d, G_l, |G*| and Y, generated using MRE for a representative 4T1, 4T1/HAS3 and MDA-MB-231 LM2-4 tumour prior to and 24 hours after saline. The tumour ROI from which necrosis was excluded is shown by a white dashed line.*

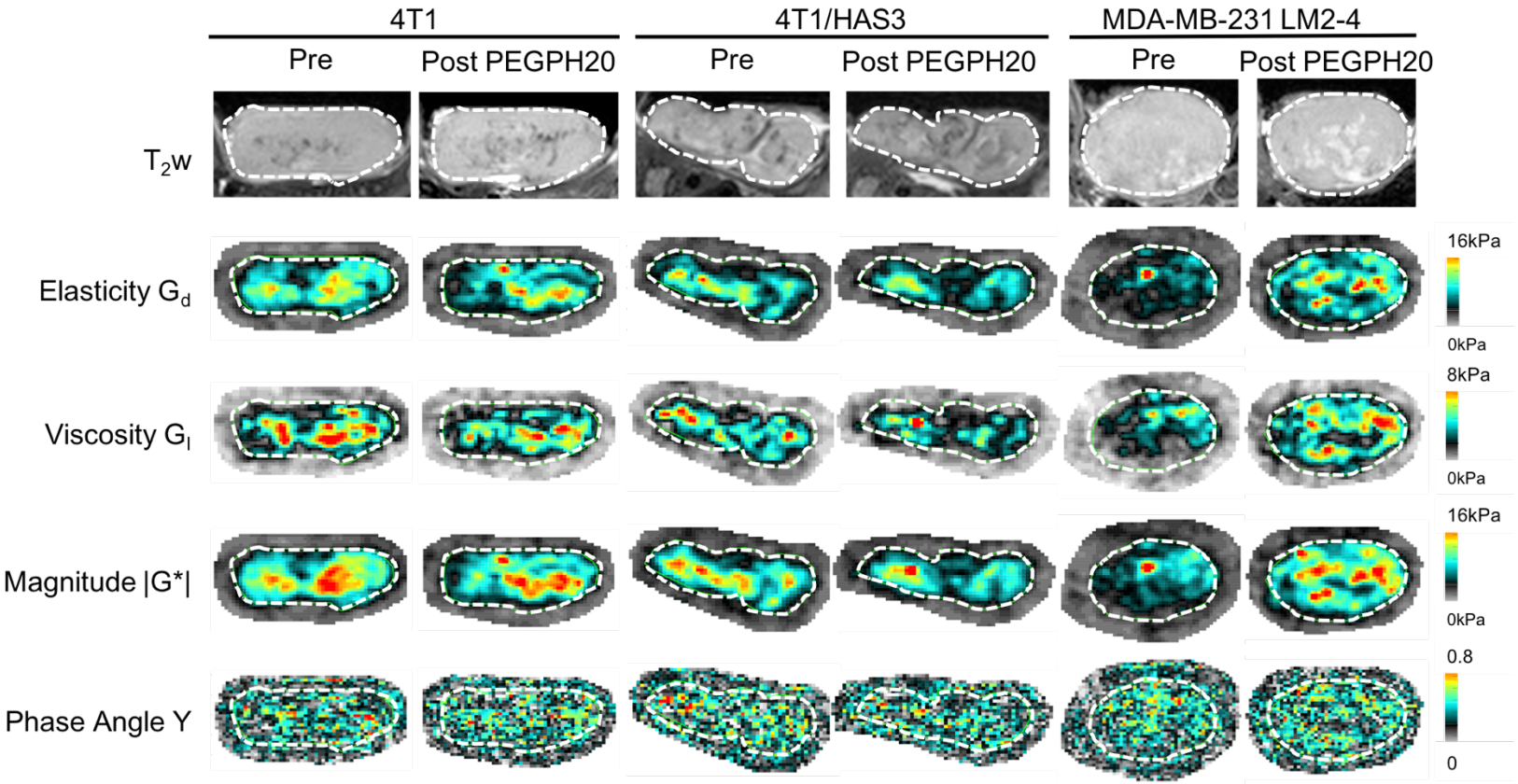

Figure 4.4: *Anatomical T_2-weighted (T_2w) MRI and parameter maps of G_d, G_l, |G*| and Y, generated using MRE for a representative 4T1, 4T1/HAS3 and MDA-MB-231 LM2-4 tumour prior to and 24 hours after PEGPH20 treatment (1 mg/kg). The tumour ROI from which necrosis was excluded is shown by a white dashed line.*

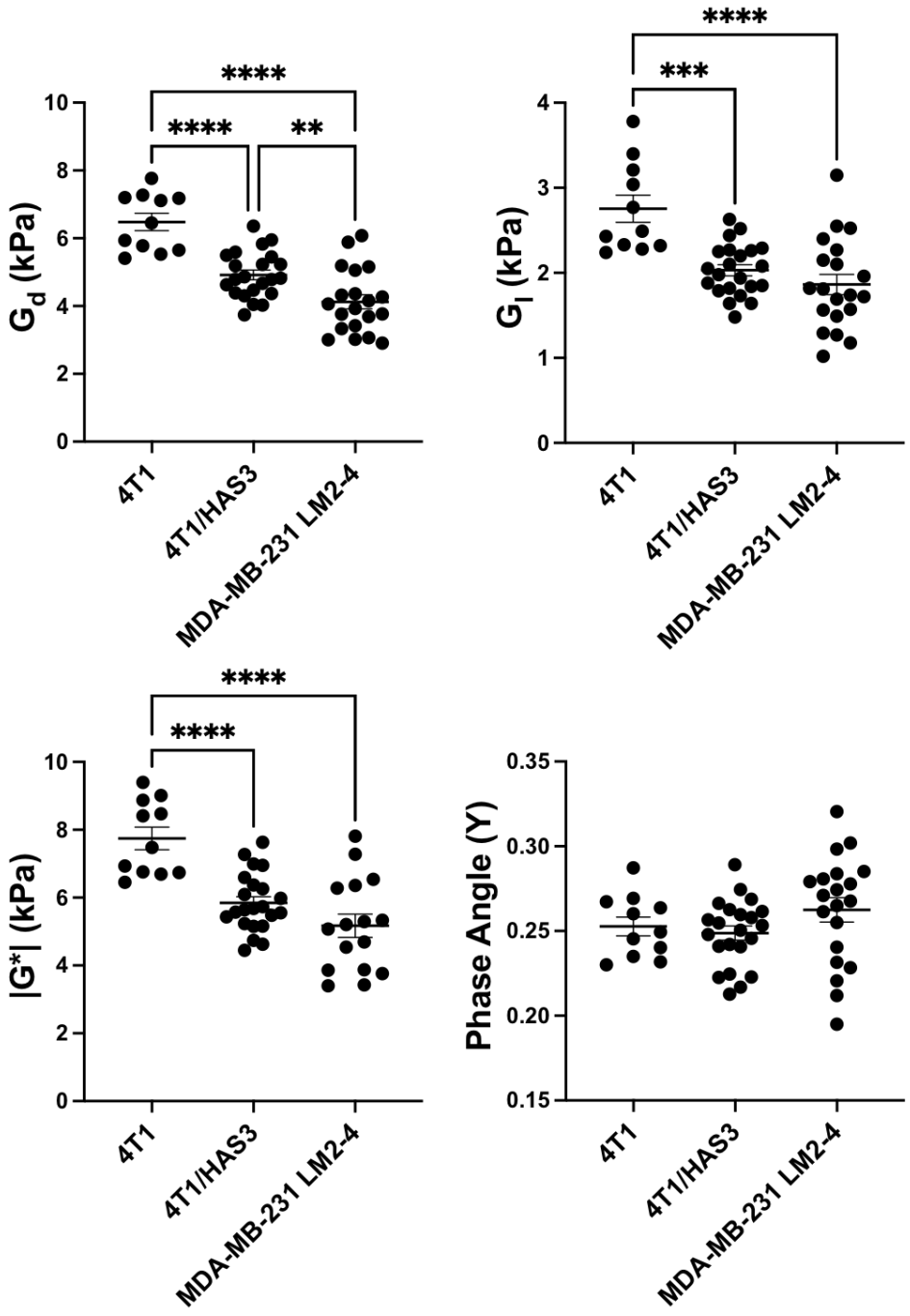

Figure 4.5: *Median G_d, G_l, |G*|, and Y values for 4T1, 4T1/HAS3 and MDA-MB-231 LM2-4 breast tumours before either saline or PEGPH20 treatment. 4T1 tumours exhibited significantly higher G_d, G_l, and |G*| at baseline compared to 4T1/HAS3 and MDA-MB-231 LM2-4 tumours (one-way ANOVA; ***p=0.0002, ****p<0.0001). 4T1/HAS3 tumours had significantly higher G_d (**p=0.008), but similar G_l and |G*| (p>0.05), compared to MDA-MB-231 LM2-4 tumours. Y was similar across all tumour models (p>0.05). Data are summarised by the cohort mean ± 1 SEM.*

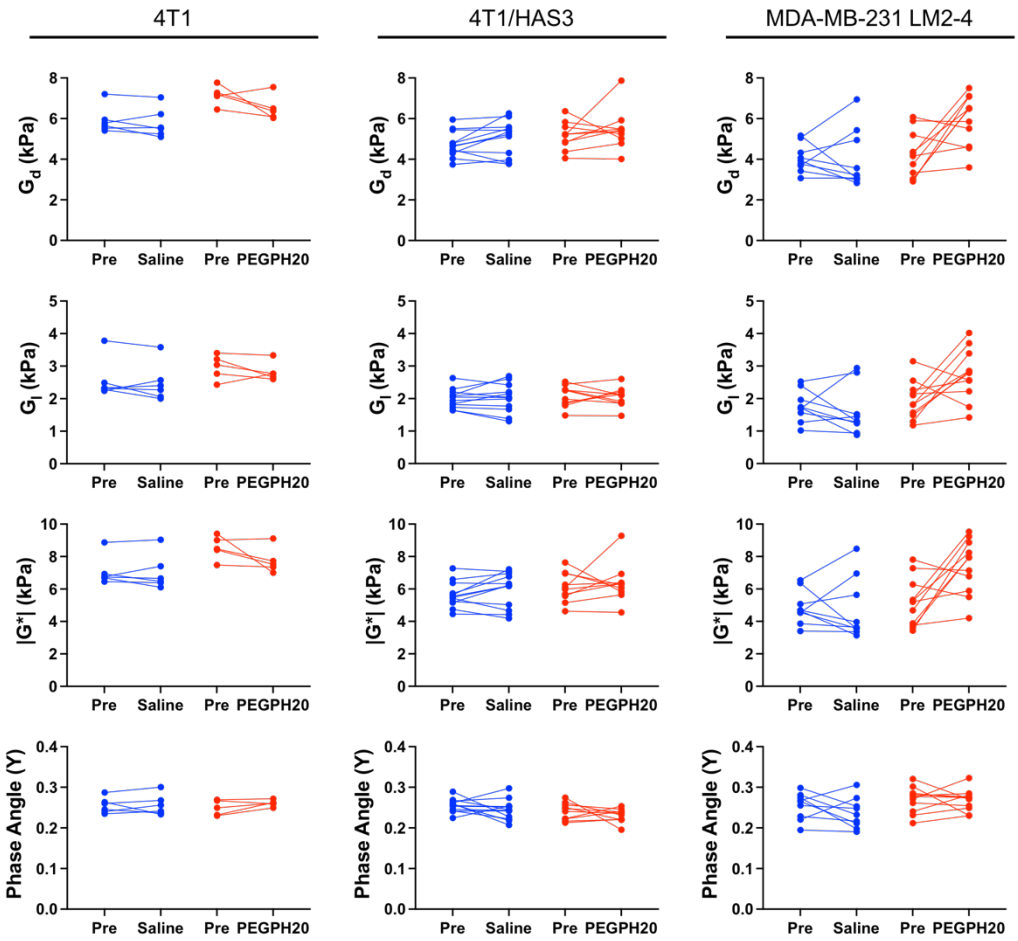

Figure 4.6: *Ladder plots showing individual median values of G_d, G_l, $|G^*|$, and Y for 4T1, 4T1/HAS3 and MDA-MB-231 LM2-4 tumours prior to and post-treatment with either saline (blue) or PEGPH20 (red). Sample sizes for 4T1, 4T1/HAS3 and MDA-MB-231 LM2-4 tumours were n = 6 saline and n = 5 PEGPH20; n = 12 saline and n = 10 PEGPH20; and n = 9 saline and n = 11 PEGPH20 respectively.*

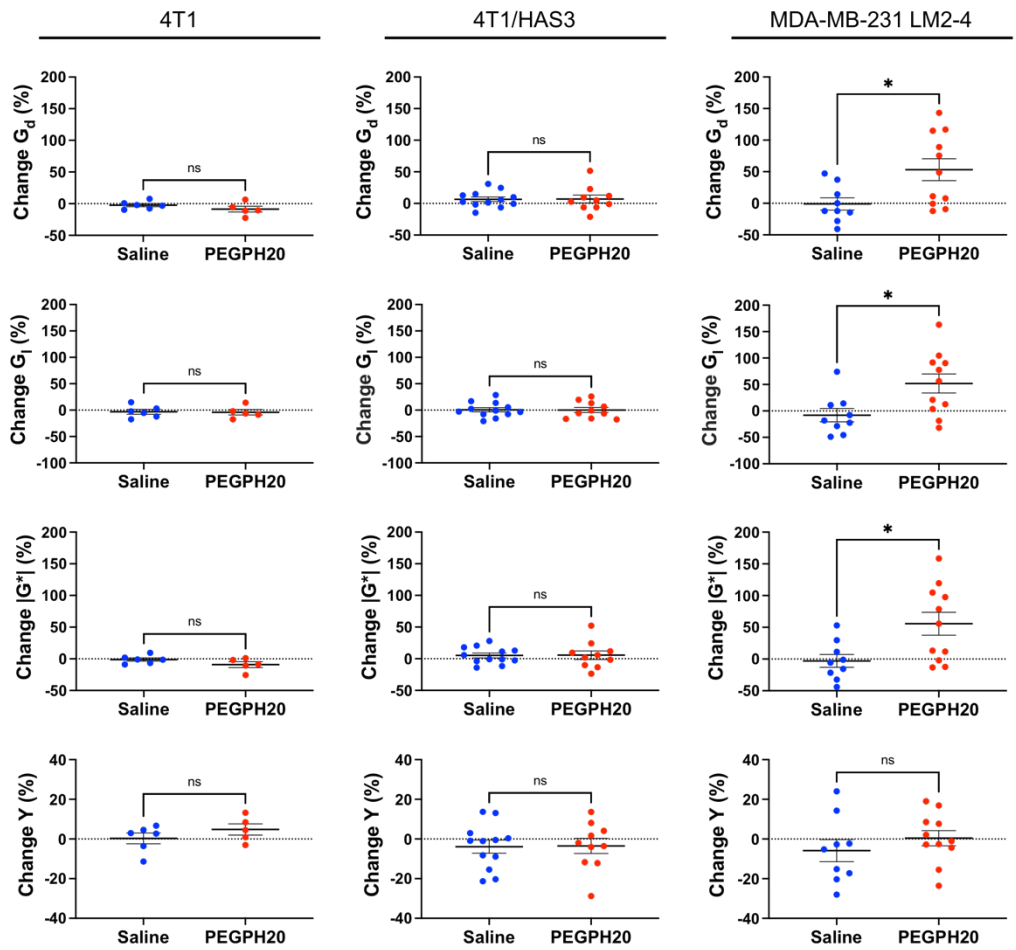

Figure 4.7: *Percentage change in G_d, G_l, |G*|, and Y between pre- and post-treatment MRI for saline and PEGPH20 treated mice bearing 4T1, 4T1/HAS3 or MDA-MB-231 LM2-4 tumours. PEGPH20 treatment did not significantly change G_d, G_l, or |G*| in 4T1 or 4T1/HAS3 tumours (ns; p>0.05, unpaired Student's t-test). PEGPH20 significantly increased G_d (*p=0.02), G_l (*p=0.02) and |G*| (*p=0.02) in MDA-MB231 LM2-4 tumours. No significant change in Y was seen in any of the breast tumour models (ns; p>0.05). Data points are median values from each individual tumour and are summarised by the cohort mean ± 1 SEM.*

At baseline, G_d was significantly higher in 4T1 tumours (6.5 ± 0.3 kPa), followed by 4T1/HAS3 tumours (4.9 ± 0.1 kPa), and lowest in MDA-MB-231 LM2-4 tumours (4.1 ± 0.2 kPa; Figure 4.5). Pre-treatment G_l and |G*| were higher in 4T1 tumours (2.8 ± 0.2 kPa and 7.7 ± 0.3 kPa respectively), compared to 4T1/HAS3 (2.0 ± 0.1 kPa and 5.8 ± 0.2 kPa) and MDA-MB-231 LM2-4 (1.9 ± 0.1 kPa and 5.2 ± 0.3 kPa) tumours. Y was similar across all tumour models.

Whilst there was no change in G_d, G_l and |G*| following PEGPH20 in the 4T1 and 4T1/HAS3 tumours, a significant increase in G_d (53 ± 17 %), G_l (52 ± 18 %) and |G*| (56 ± 18 %) was determined in MDA-MB-231 LM2-4 tumours in response to PEGPH20 (Figures 4.6 & 4.7). No PEGPH20-induced change in Y was apparent. The increase in G_d, G_l, and |G*| following PEGPH20 occurred in 6 of the 11 MDA-MB-231 LM2-4 tumours evaluated. These 6 tumours had an increase between 49 and 163%. The 5 remaining MDA-MB-231 LM2-4 tumours showed less change from baseline (ranging from a 32% decrease to a 13% increase in biomechanical properties).

The MRI-aligned picrosirius red stained tumour sections shown in Chapter 3 (Figure 3.10) were further quantified to describe the 2D distribution of collagen. As shown in Figures 3.11 and 4.8, saline control MDA-MB-231 LM2-4 tumours had significantly less collagen I & III than 4T1 ($p = 0.003$) and 4T1/HAS3 ($p = 0.02$) tumours. The distribution of collagen in saline control MDA-MB-231 LM2-4 tumours had lower fractal dimension and higher entropy compared to saline control 4T1 ($p = 0.0004$ and $p < 0.0001$ respectively) and 4T1/HAS3 ($p < 0.0001$) tumours. Three of the six MDA-MB-231 LM2-4 tumours which showed large increases in G_d, G_l and |G*| following PEGPH20 treatment had higher collagen content (~9%) and fractal dimension (~1.65), and lower entropy (~1) compared to saline controls. The remaining MDA-MB-231 LM2-4 tumour with high collagen deposition and fractal dimension, and low entropy had relatively high G_d (5.2 kPa), G_l (2.6 kPa), and |G*| (6.3 kPa) at baseline which did not increase following PEGPH20 treatment.

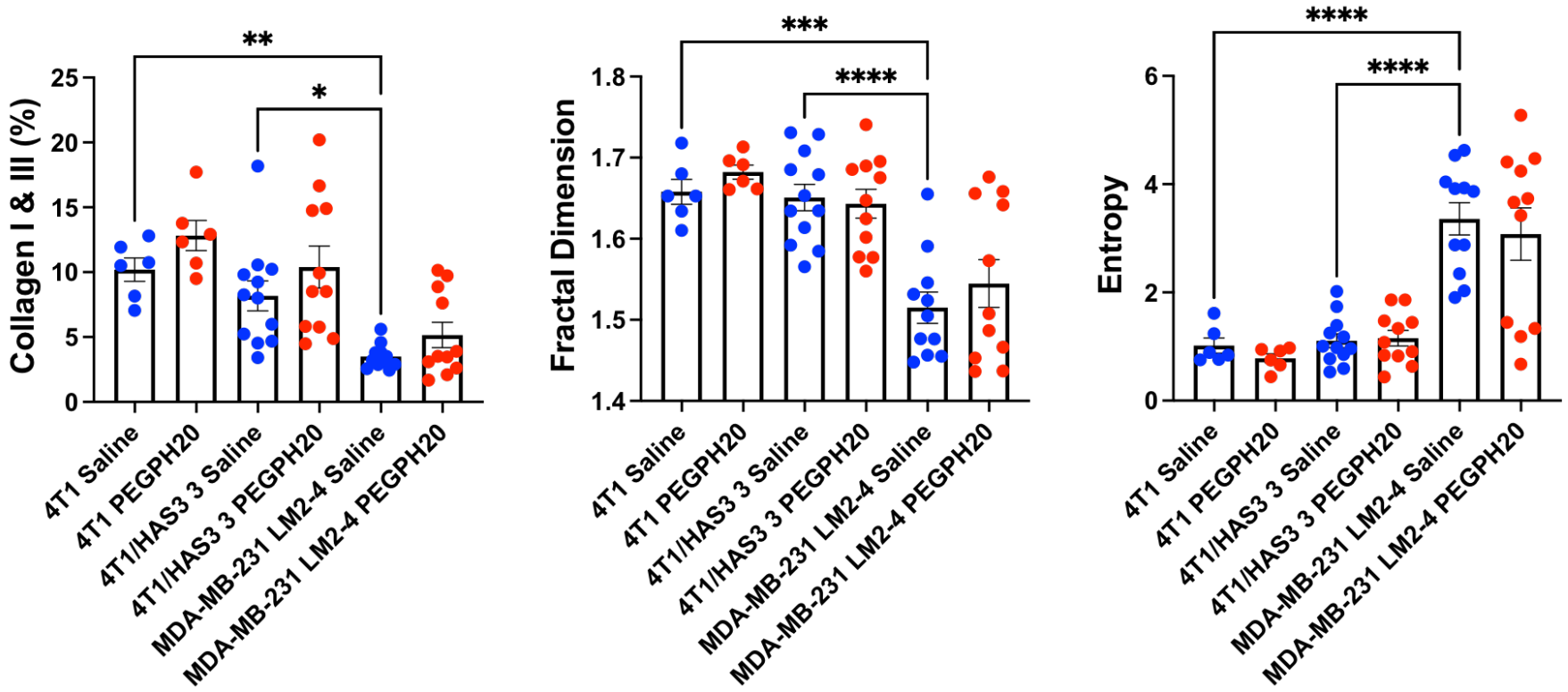

Figure 4.8: *Collagen content (%), fractal dimension, and entropy quantified from picrosirius red stained 4T1, 4T1/HAS3 and MDA-MB-231 LM2-4 tumour sections. The graph of collagen content is also shown in Chapter 3 (Figure 3.11). Significant differences between saline controls, and between saline and PEGPH20 treated tumours within the same tumour model are shown (one-way ANOVA; *p<0.05, **p<0.01, ***p<0.001, ****p<0.0001).*

4.3 Discussion:

The elasticity modulus (G_d) has been shown previously to positively correlate with gelatine concentration[233]; the data herein confirms this and suggests that it is also the case for G_l, |G*| and Y. Gelatine phantoms of higher concentration contain more protein, including collagen, providing structure and improving the ability of the phantom to resist deformation, resulting in a higher G_d, G_l, and |G*|. The phase angle (Y) is a measure of the relative contributions of G_d and G_l to |G*|[159]. Y is related to energy loss, for example shear wave absorption or scattering by tissue structure, and so was also expected to rise with increasing gelatine concentration[212, 234].

The relative stiffness of 4T1, 4T1/HAS3, and MDA-MB-231 LM2-4 tumours measured herein was slightly lower than previous MRE studies which estimated orthotopic BT474 and MDA-MB-231 LM2-4 breast tumour G_d to be 5.9 and 7.9 kPa respectively[46]. The MRE set-up, wave propagation, and data analysis were similar in both studies, however the MRE sequence in the previous study was almost three times longer and used more wave phases to estimate viscoelastic properties which may explain the differences. In addition, the lower stiffness seen herein may result from different tumour biology such as less deposition or different organisation of collagen fibres, a key determinant of tissue viscoelastic properties[46, 235].

MRE revealed that 4T1/HAS3 tumours had lower G_d, G_l and |G*| compared to 4T1 tumours. The only difference between these two tumour models is the overexpression of HAS3, and so these data suggest that HA accumulation contributes to a lowering of the elastic and viscous moduli. Despite this, HA degradation by PEGPH20 induced no change in G_d, G_l, or |G*| of 4T1 and 4T1/HAS3 tumours. It may be that HA accumulation during tumour development is associated with a softer and less viscous phenotype, but the extent of HA itself does not directly contribute to tumour viscoelastic properties.

PEGPH20 induced an ~80% increase in G_d, G_l, and |G*| in MDA-MB-231 LM2-4 tumours. Given that there was no change in 4T1 and 4T1/HAS3 tumour viscoelastic properties following PEGPH20, the MDA-MB-231 LM2-4 tumour response is presumably not due to HA degradation alone and is more likely a consequence of other biomechanical-related changes. The phase angle (Y) did not change following PEGPH20 in any of the tumour models and therefore is not sensitive to HA accumulation and its therapeutic degradation.

Collagen is a determinant of tumour viscoelastic properties[46]. Quantitative histology suggests a higher collagen content, coupled with increased collagen complexity (fractal dimension) and a more ordered collagen distribution (lower entropy) in three of the six MDA-MB-231 LM2-4 tumours with elevated G_d, G_l, and |G*| following PEGPH20 treatment. This is consistent with a more organised collagen network and may contribute to, but does not fully explain, the marked increase in tumour stiffness following PEGPH20.

Stromal modulatory therapies have the potential to suppress tumour progression through enhancement of drug delivery and promote tumour progression by removing barriers to invasion and metastasis[41, 57, 107]. The elevated tumour stiffness observed in PEGPH20 treated MDA-MB-231 LM2-4 tumours may thus be indicative of tumour progression. Future work should evaluate whether PEGPH20 treatment can have a detrimental effect and assess how this would translate to patients treated with ECM targeted therapies.

Many oncological MRE studies have typically reported tumour softening associated with cell death following effective treatment[157, 159]. Although MRE is unlikely to provide a direct biomarker of PEGPH20 response, the data herein clearly demonstrate the sensitivity of MRE to inform on pharmacologically-induced increases in tumour stiffness, and support further evaluation of G_d, G_l and |G*| as binary imaging biomarkers of tumour treatment response.

In conclusion, HA accumulation is sometimes associated with lower viscoelastic properties, although this is likely to be dependent on how HA is interacting with its surrounding microenvironment. PEGPH20 elicited different, model-specific, effects on tumour viscoelasticity. Without a tumour-specific calibration of the effects of HA accumulation on viscoelastic properties and a reliable independent method for classifying tumours according to type, it is unlikely MRE will provide a robust biomarker of HA degradation by PEGPH20.

Chapter 6 collates all the data from Chapters 3, 4, and 5 and compares relationships between MRI biomarkers and histology. It also provides greater insight into the relationship of HA with tumour viscoelastic properties.

Chapter 5: Intrinsic susceptibility (IS)-MRI can provide a biomarker of blood vessel decompression following PEGPH20 treatment

5.1 Introduction

The dense fibrotic stroma typically associated with breast cancer compresses tumour blood vessels, thereby impairing efficient drug delivery[25]. Degradation of HA by PEGPH20 has been shown, in pre-clinical models including breast tumours, to decompress tumour blood vessels and improve drug delivery[14, 15, 49, 215]. Non-invasive monitoring of this process may identify appropriate timepoints for optimal drug delivery.

The transverse relaxation rate (R_2*), quantified using intrinsic susceptibility (IS)-MRI, is sensitive to the concentration of paramagnetic deoxyhaemoglobin within tissue vasculature[201]. Tumours often exhibit relatively fast R_2* compared to most normal tissues, a consequence of the high concentration of deoxygenated red blood cells (RBCs) within the typically chaotic and unstable microcirculation. IS-MRI has thus been utilised to investigate tumour angiogenesis and response to vascular targeted therapies[169, 202]. A recent study showed that parametric maps of tumour R_2* reflect the spatial variation in RBCs seen histologically[202]. Given that blood vessel decompression is likely to increase the number of RBCs in the vasculature, we hypothesised that quantitation of R_2* may inform on breast tumour response to PEGPH20.

The ability of IS-MRI to inform on paramagnetic species has been validated by other members of the team (unpublished) hence no phantom experiments were required before IS-MRI was used *in vivo*. IS-MRI was performed prior to and after treatment with either saline or PEGPH20 in 4T1, 4T1/HAS3, and MDA-MB-231 LM2-4 breast tumours. MRI-aligned tumour tissue sections were stained for CD31 to quantify blood vessels.

5.2 Results:

T_2-weighted MRI and parametric maps of R_2*, acquired from IS-MRI, are shown for a representative 4T1, 4T1/HAS3, and MDA-MB-231 LM2-4 tumour before and after treatment with either saline (Figure 5.1) or PEGPH20 (Figure 5.2). There was no apparent change in R_2* following saline in any of the tumour models. There was an increase in 4T1/HAS3 tumour R_2* following PEGPH20 treatment, this increase occurred across the majority of the tumour but there were some regions which had low R_2* before treatment and did not appear to change following PEGPH20. There was no apparent PEGPH20-induced change in R_2* of 4T1 and MDA-MB-231 LM2-4 tumours.

Median R_2* values prior to and after treatment with either saline or PEGPH20 are shown in Figure 5.3 and the percentage change values are shown in Figure 5.4. The sample size for 4T1/HAS3 tumours is smaller here than in Chapters 3 and 4 because the decision to include IS-MRI in the multiparametric MRI protocol was made after the initial pilot 4T1/HAS3 experiments had been conducted. The within-subject test-retest coefficient of variation for R_2* was 16% when using pre- and post-saline data for both tumour models.

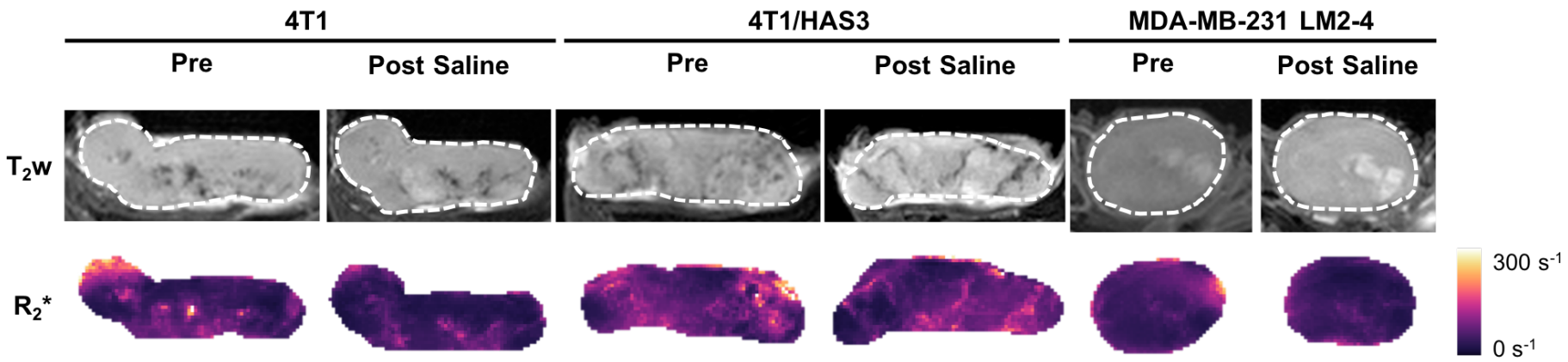

Figure 5.1: *Anatomical T_2-weighted (T_2w) MRI and parameter maps of R_2*, generated using IS-MRI, for a representative 4T1, 4T1/HAS3 and MDA-MB-231 LM2-4 tumour prior to and 24 hours after saline. The tumour ROI from which necrosis was excluded is shown by a white dashed line.*

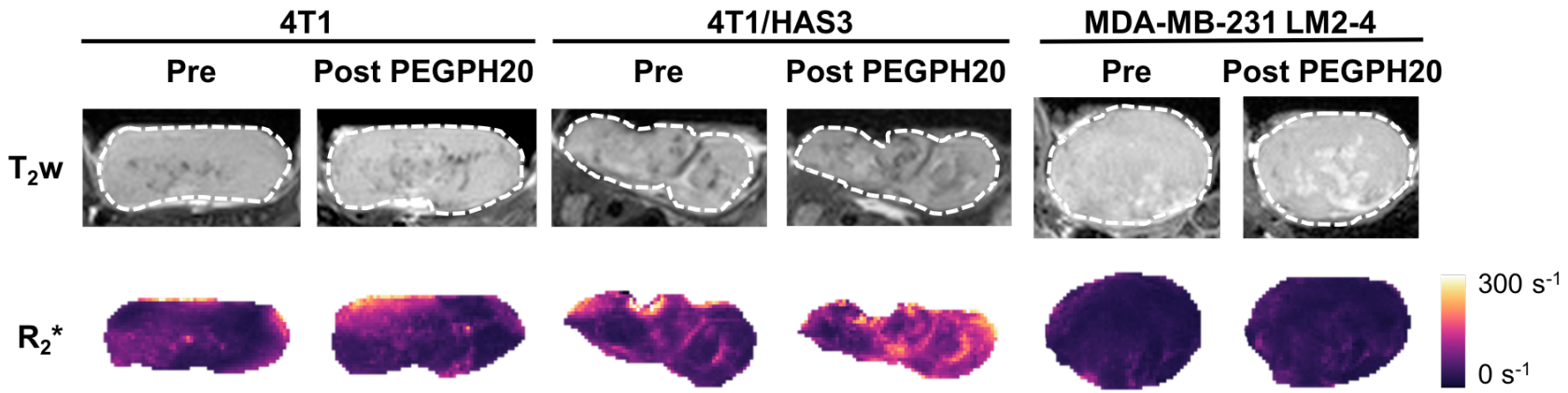

Figure 5.2: *Anatomical T_2-weighted (T_2w) MRI and parameter maps of R_2*, generated using IS-MRI, for a representative 4T1, 4T1/HAS3 and MDA-MB-231 LM2-4 tumour prior to and 24 hours after PEGPH20 treatment (1 mg/kg). The tumour ROI from which necrosis was excluded is shown by a white dashed line.*

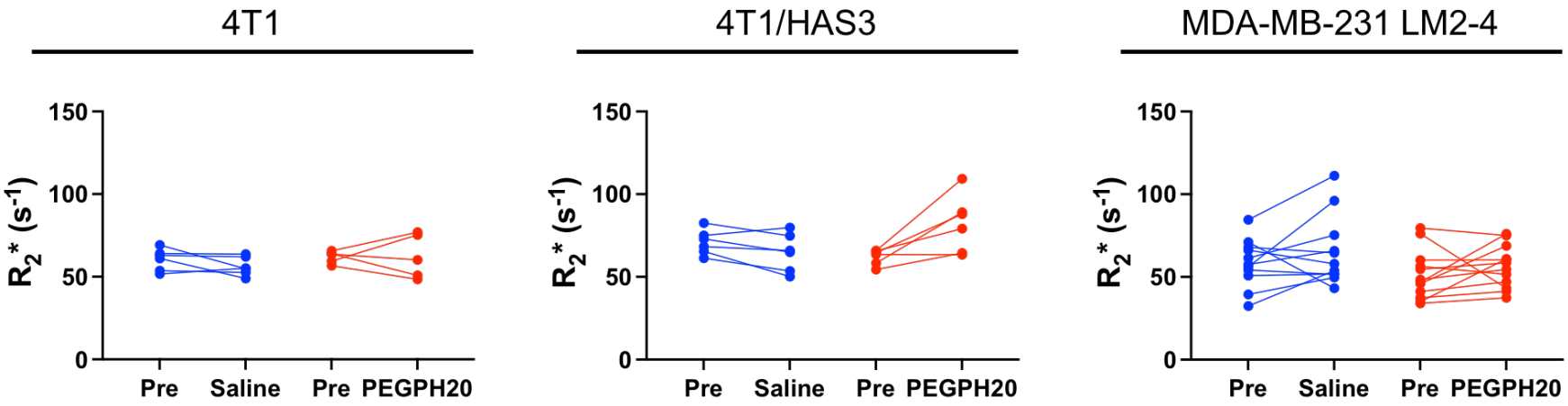

Figure 5.3: *Median R_2* for 4T1, 4T1/HAS3 and MDA-MB-231 LM2-4 tumours pre-saline, post-saline, pre-PEGPH20 and post-PEGPH20. Data from each individual tumour are plotted, with saline controls in blue and PEGPH20 treated tumours in red. Sample sizes for 4T1, 4T1/HAS3 and MDA-MB-231 LM2-4 tumours were: n = 6 saline and n = 5 PEGPH20; n = 6 saline and n = 6 PEGPH20; and n = 11 saline and n = 12 PEGPH20 respectively.*

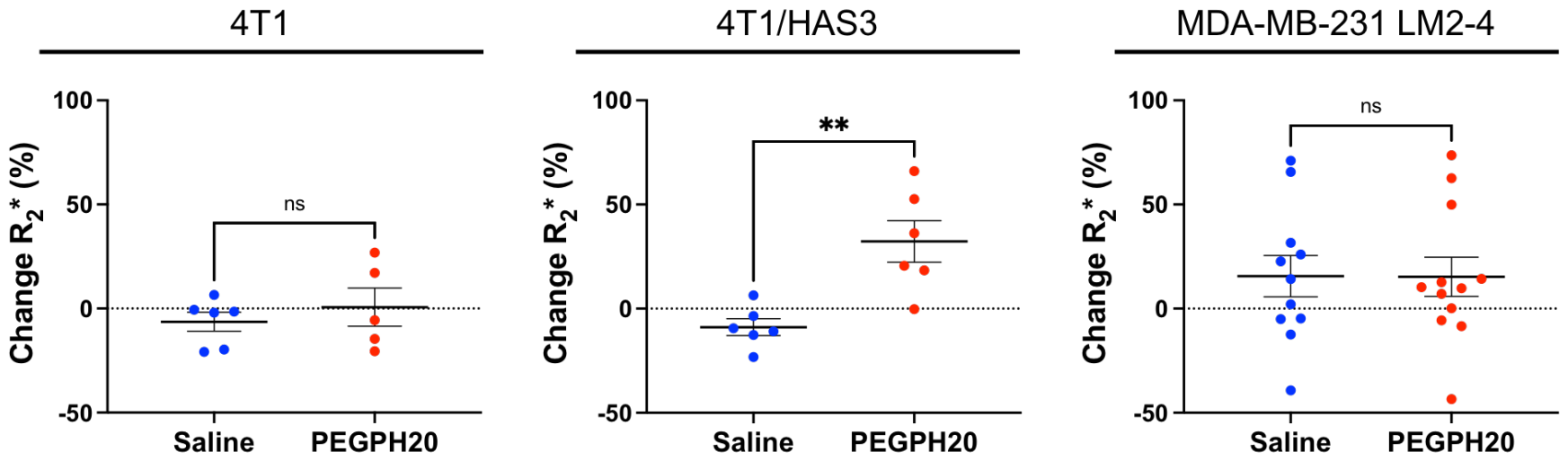

Figure 5.4: *Percentage change in R_2* between pre- and post-treatment MRI for saline and PEGPH20 treated mice bearing 4T1, 4T1/HAS3 or MDA-MB-231 LM2-4 tumours. PEGPH20 treatment did not significantly change R_2* in 4T1 or MDA-MB-231 LM2-4 tumours (ns; p>0.05, unpaired Student's t-test). PEGPH20 increased R_2* (**p=0.003) in 4T1/HAS3 tumours. Data points are percentage differences (post minus pre) of median values from each individual tumour and are summarised by the cohort mean ± 1 SEM.*

R_2* was significantly faster in 4T1/HAS3 tumours following PEGPH20 treatment (Figures 5.3 & 5.4). R_2* increased 32% from 62 ± 2 s^{-1} to 82 ± 7 s^{-1} following PEGPH20 in 4T1/HAS3 tumours whilst R_2* decreased 9% from 71 ± 3 s^{-1} to 65 ± 5 s^{-1} in saline controls. PEGPH20 treatment did not significantly change R_2* in 4T1 or MDA-MB-231 LM2-4 tumours.

CD31 staining of MRI-aligned tumour tissue sections revealed that blood vessel density was highest in 4T1/HAS3 saline control tumours (370 ± 19 blood vessels per mm^2 tissue), followed by 4T1 tumours (246 ± 16 per mm^2), and lowest in MDA-MB-231 LM2-4 tumours (95 ± 4 per mm^2; Figures 5.5 & 5.6). PEGPH20 treatment did not have a significant effect on blood vessel density, quantified from CD31 staining, in any of the tumour models ($p>0.05$; Figure 5.6).

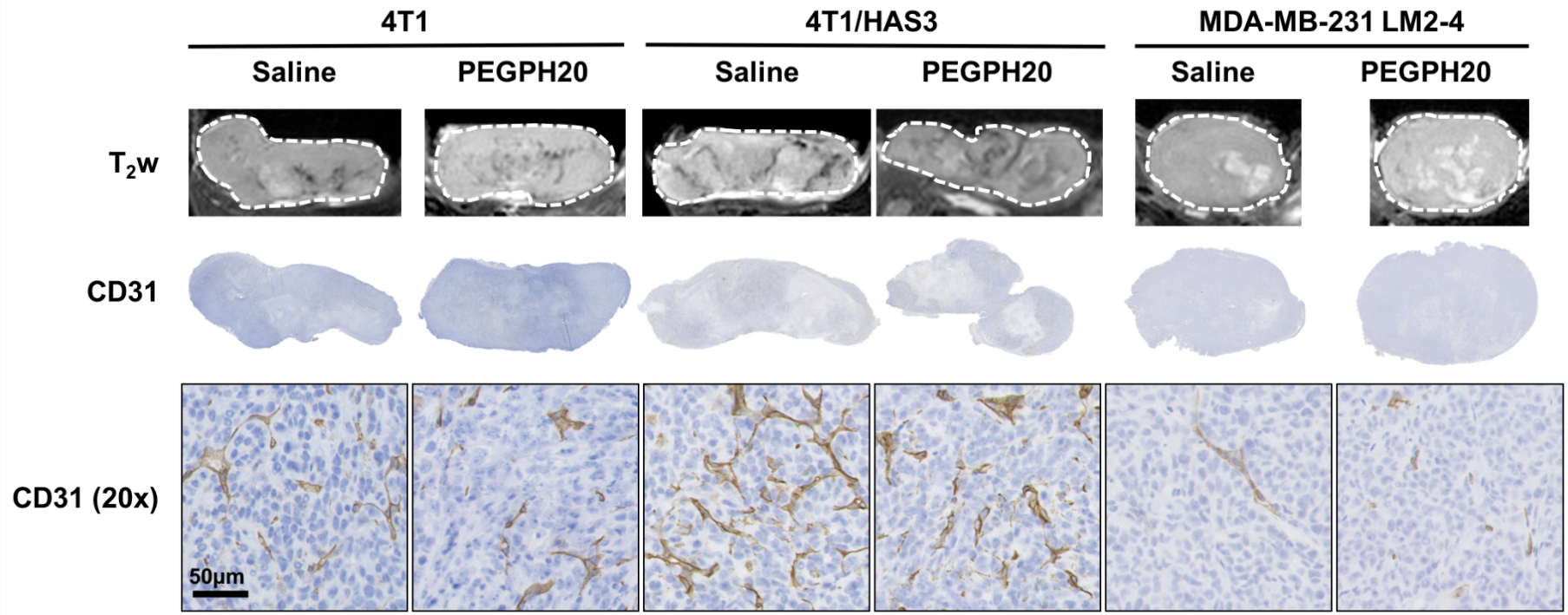

Figure 5.5: *T_2-weighted (T_2w) MRI alongside representative aligned 4T1, 4T1/HAS3 and MDA-MB-231 LM2-4 tumour tissue sections (5 μm) stained for CD31 (blood vessels). Representative magnified images (20x) are presented alongside whole tumour section images for one saline control and one PEGPH20 treated tumour per tumour model.*

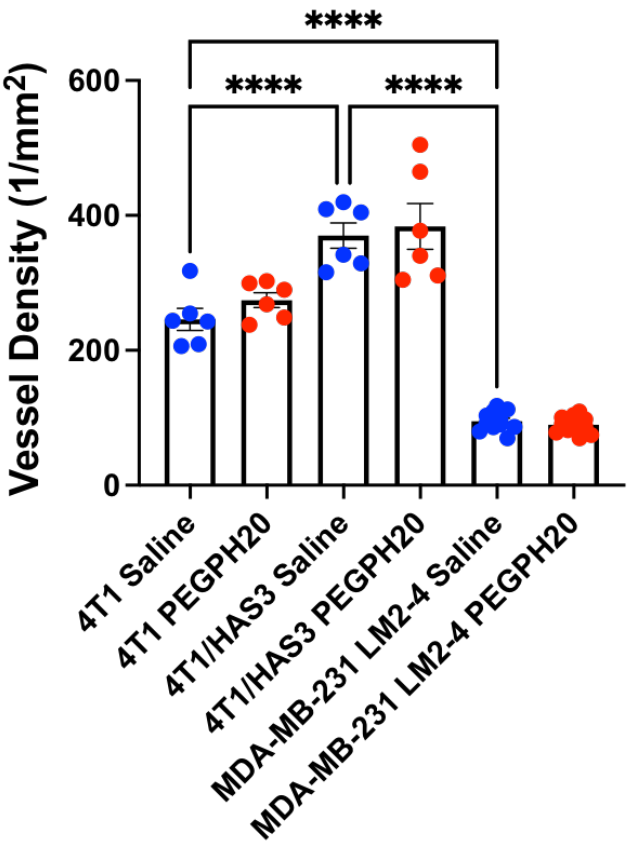

Figure 5.6: *Blood vessel density (number per mm^2 tumour tissue) quantified from CD31 stained 4T1, 4T1/HAS3 and MDA-MB-231 LM2-4 tumour tissue sections. Blood vessel density was highest in 4T1/HAS3 tumours, followed by 4T1 tumours, and lowest in MDA-MB-231 LM2-4 tumours (one-way ANOVA with multiple comparisons; ****p<0.0001). PEGPH20 treated tumours had similar blood vessel density to saline controls in all three tumour models (p>0.05).*

5.3 Discussion:

4T1/HAS3 tumours exhibited a faster baseline R_2* than 4T1 and MDA-MB-231 LM2-4 tumours, suggesting that 4T1/HAS3 tumours have more haemodynamic vasculature. R_2* significantly increased following PEGPH20 treatment in 4T1/HAS3 tumours, however, IS-MRI was unable to detect a similar response to PEGPH20 in 4T1 and MDA-MB-231 LM2-4 tumours.

4T1/HAS3 tumours had more HA accumulation and higher blood vessel density, measured by HTI-601 and CD31 histological staining respectively, compared to 4T1 and MDA-MB-231 LM2-4 tumours. The increase in R_2* following PEGPH20 treatment in 4T1/HAS3 tumours is consistent with decompression of blood vessels and increased accessibility of RBCs within the tumour microenvironment. The lack of change in R_2* after PEGPH20 treatment in 4T1 and MDA-MB-231 LM2-4 tumours may suggest that i) PEGPH20 treatment did not decompress blood vessels in these tumour models, ii) blood vessel decompression is not always correlated with an increase in RBCs, or iii) decompression of a smaller number of blood vessels does not create a large enough change in susceptibility to be detected by R_2*[201].

The blood vessel density of tumours at baseline may determine whether R_2* is a useful biomarker of PEGPH20 response. 4T1/HAS3 tumour R_2* increased 32% following PEGPH20 treatment. 4T1 and MDA-MB-231 LM2-4 tumours had approximately half and quarter of the blood vessel density of the 4T1/HAS3 tumours. Based on the linear relationship between R_2* and RBCs demonstrated in a previous study[202], you could expect that the change in R_2* would be halved and quartered in 4T1 and MDA-MB-231 LM2-4 tumours respectively which would be at or below the 16% test-retest coefficient of variation for R_2*. Moreover, the lower HA accumulation at baseline in 4T1 and MDA-MB-231 LM2-4 tumours may further reduce the amount of vascular decompression occurring after PEGPH20 treatment.

Endogenous R_2* is sensitive to deoxygenated haemoglobin and so can also be affected by hypoxia, a common phenomenon in the tumour microenvironment[236]. This may limit the ability of IS-MRI to detect tumour blood vessel decompression. DCE-MRI and SC-MRI use intravenous contrast agents, such as gadolinium or USPIO respectively, to measure perfusion in patent vasculature and so are not affected by hypoxia. The volume transfer constant (K^{trans}), quantitated from DCE-MRI, has been shown to increase following PEGPH20 treatment in pre-clinical and human pancreatic ductal adenocarcinomas (PDAC)[38, 205]. Tumour blood volume, estimated using SC-MRI, also increased following PEGPH20 treatment in pre-clinical models of PDAC[209]. We did not include contrast agents in our multiparametric MRI experiments due to the potential high-risk of failure associated with three intravenous injections within 24 hours, and the potential effect of the contrast agents on the other biomarkers described in Chapters 3 and 4, especially given that there is only 24 hours between pre- and post-treatment MRI.

In conclusion, R_2* is a sensitive biomarker of PEGPH20 response in well vascularised 4T1/HAS3 tumours with high HA accumulation. Alternative vascular biomarkers, such as those derived from SC-MRI, may provide greater sensitivity and specificity to PEGPH20 vascular response in more hypovascular tumours with less HA accumulation at baseline.

The next chapter brings together all the MRI and histology data discussed in Chapters 3, 4, and 5, and provides further clarity on the biological determinants of the MRI biomarkers and how these change in the presence and absence of HA.

Chapter 6: Investigating the contribution of HA to the breast tumour microenvironment using multiparametric MRI and histology

6.1 Introduction:

In Chapter 3, ADC was shown to be a sensitive biomarker of pre-clinical breast tumour response to PEGPH20, likely due to a decrease in tumour water content and reduction of the extracellular space following HA degradation. Additional MRI biomarkers (T_1, T_2, MTR, R_2*, G_d, G_l, |G*|, and Y) were evaluated in Chapters 3, 4 and 5 but failed to provide as robust an indication of tumour response to PEGPH20.

More can still be learnt about the impact of HA on the tumour characteristics as measured by MRI. In this chapter, all the data discussed in Chapters 3, 4 and 5 have been collated to consider and evaluate relationships between MRI biomarkers (T_1, T_2, MTR, ADC, R_2*, G_d, G_l, |G*|, and Y) and histology in saline (HA present) and PEGPH20 treated (HA degraded) 4T1, 4T1/HAS3, and MDA-MB-231 LM2-4 breast tumours.

6.2 Results & Discussion:

Multiparametric MRI and histology images for one representative saline control MDA-MB-231 LM2-4 breast tumour are shown in Figure 6.1. Clear spatial correspondence between the MRI and histology is apparent, enabling an assessment of the pathological determinant(s) of the MRI biomarkers.

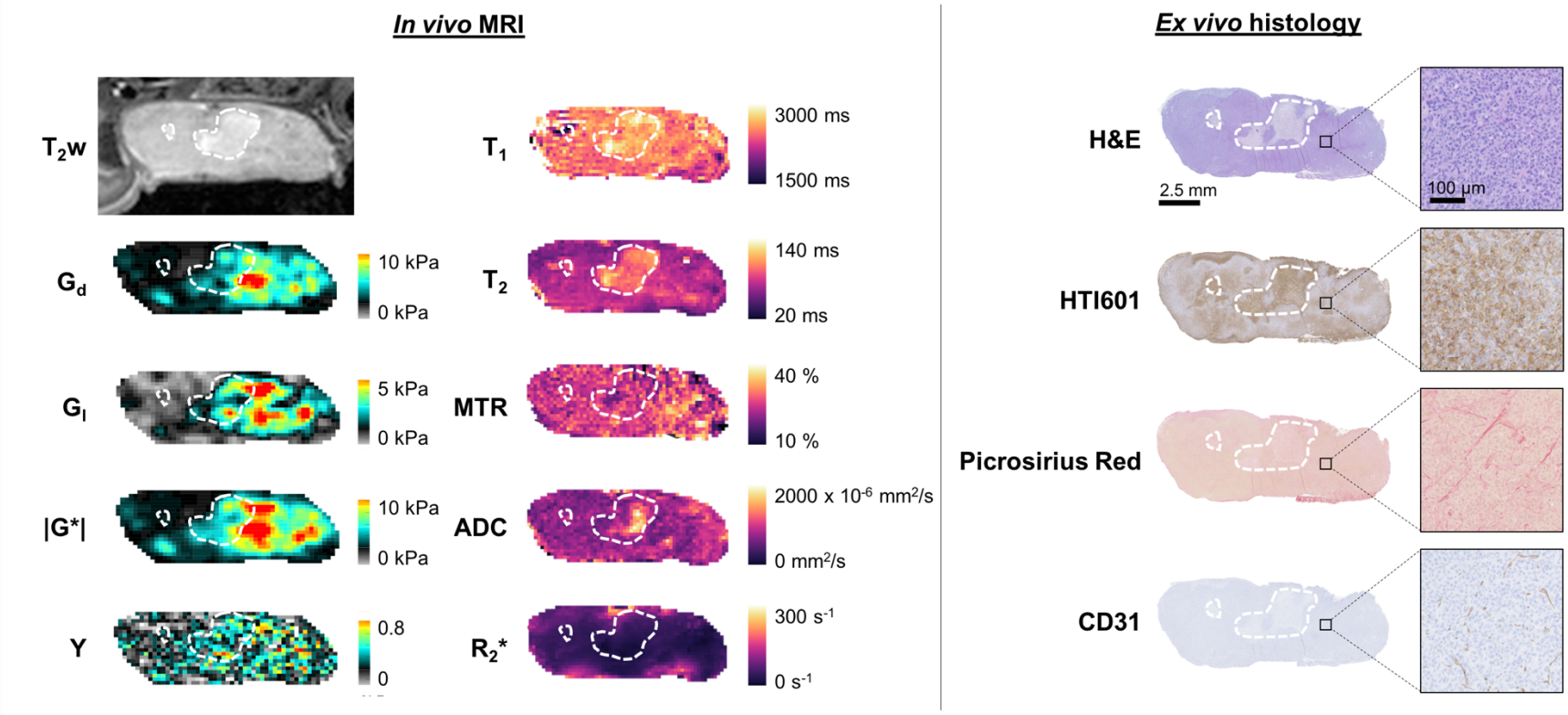

Figure 6.1: *Representative MRI and matched histology images (whole section and 10x magnification images) from a representative MDA-MB-231 LM2-4 tumour post-treatment with saline. Necrosis, which was excluded from quantitative analyses, is indicated by a white dashed line. MRI-aligned tumour tissue sections were stained using H&E (morphology), HTI-601 (HA), picrosirius red (collagen I & III), and CD31 (blood vessels).*

The correlation matrix for all the post-treatment (saline & PEGPH20) measurements is shown in Figure 6.2a. To further investigate the contribution of HA, the data were separated into saline control (Figure 6.2b) and PEGPH20 treated tumours (Figure 6.2c). I could then evaluate whether the relationships between MRI biomarkers and histology were different in the presence (saline) or absence (PEGPH20) of HA. Sample sizes (n) and p-values (p) for each correlation are shown in Figure 6.3.

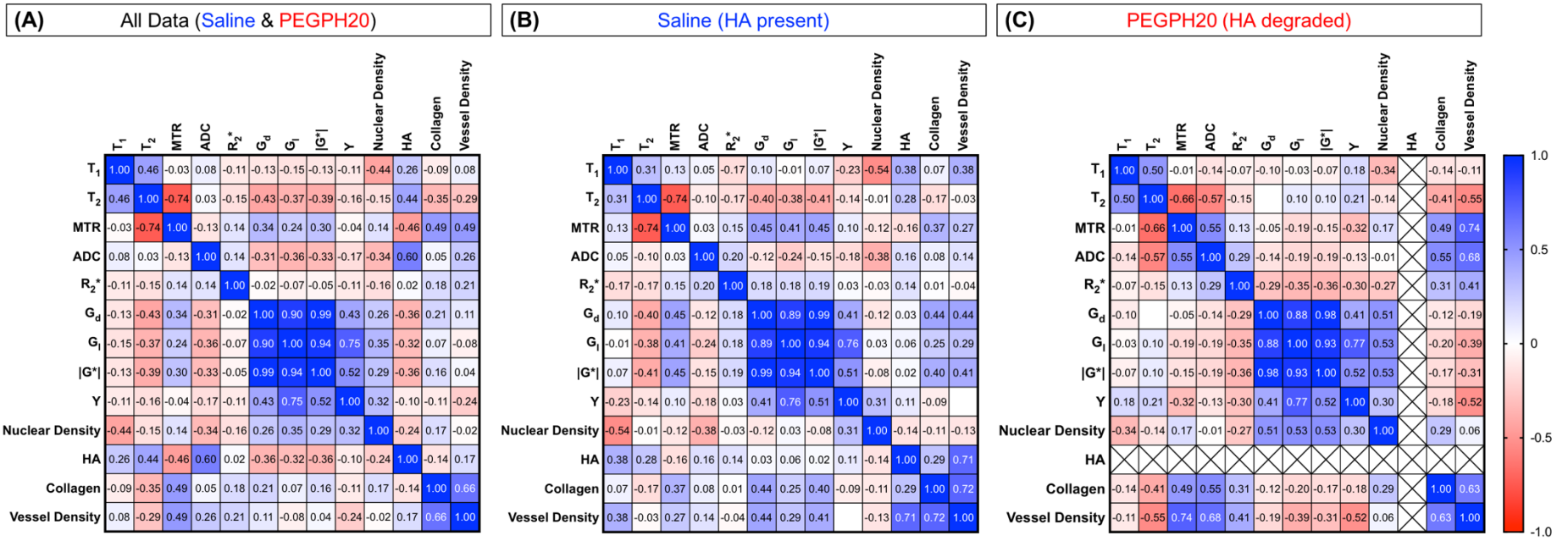

Figure 6.2: *Correlation matrices of MRI biomarkers and matched histological staining. The correlation matrices show Pearson's correlation coefficient (r) for each pairing. Relationships were evaluated with all data pooled together* ***(A)****, and with saline* ***(B)*** *and PEGPH20 treated* ***(C)*** *tumour data kept separate. Nuclear density, percentage HA, percentage collagen (I & III), and vessel density were calculated from H&E, HTI-601, picrosirius red, and CD31 staining respectively. Negligible levels of HA (< 2%) were detectable in the PEGPH20 treated tumours, hence percent HA was excluded from the correlation analysis in this group (crossed-out squares). For blank squares r < 0.01.*

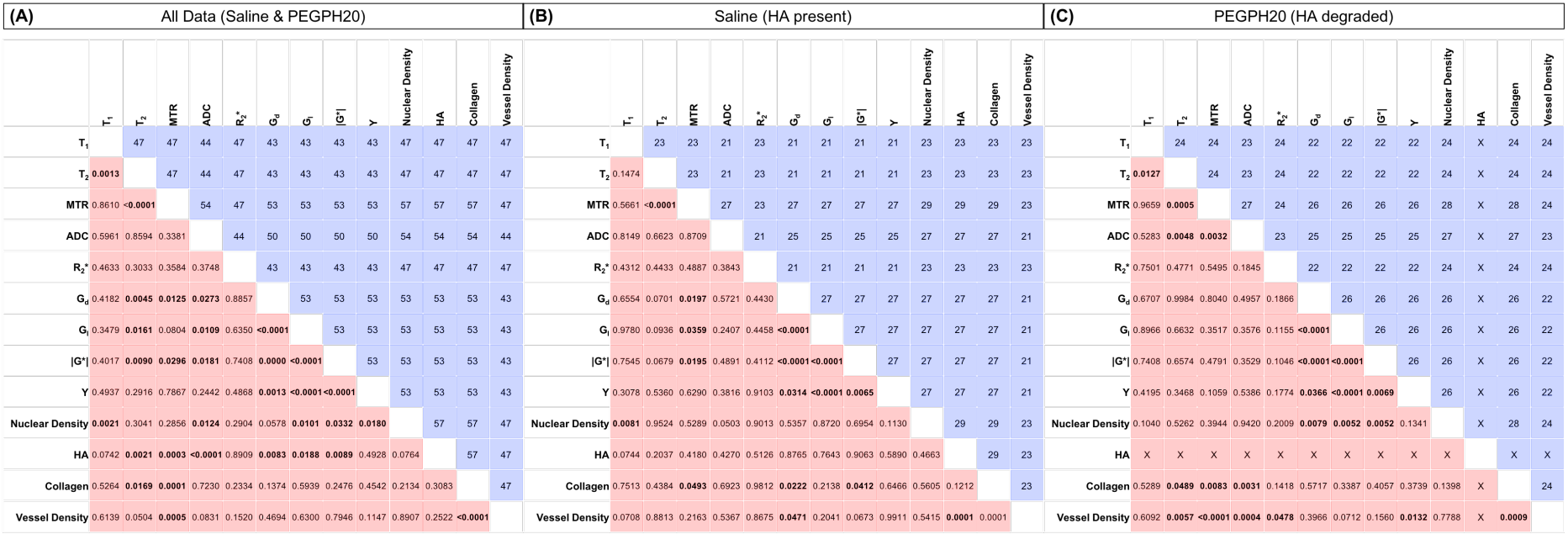

(A) All Data (Saline & PEGPH20)

	T_1	T_2	MTR	ADC	R_2*	G_d	G_l	|G*|	Y	Nuclear Density	HA	Collagen	Vessel Density
T_1		47	47	44	47	43	43	43	43	47	47	47	47
T_2	**0.0013**		47	44	47	43	43	43	43	47	47	47	47
MTR	0.8610	**<0.0001**		54	47	53	53	53	53	57	57	57	47
ADC	0.5961	0.8594	0.3381		44	50	50	50	50	54	54	54	44
R_2*	0.4633	0.3033	0.3584	0.3748		43	43	43	43	47	47	47	47
G_d	0.4182	**0.0045**	**0.0125**	**0.0273**	0.8857		53	53	53	53	53	53	43
G_l	0.3479	**0.0161**	0.0804	**0.0109**	0.6350	**<0.0001**		53	53	53	53	53	43
|G*|	0.4017	**0.0090**	**0.0296**	**0.0181**	0.7408	**0.0000**	**<0.0001**		53	53	53	53	43
Y	0.4937	0.2916	0.7867	0.2442	0.4868	**0.0013**	**<0.0001**	**<0.0001**		53	53	53	43
Nuclear Density	**0.0021**	0.3041	0.2856	**0.0124**	0.2904	0.0578	**0.0101**	**0.0332**	**0.0180**		57	57	47
HA	0.0742	**0.0021**	**0.0003**	**<0.0001**	0.8909	**0.0083**	**0.0188**	**0.0089**	0.4928	0.0764		57	47
Collagen	0.5264	**0.0169**	**0.0001**	0.7230	0.2334	0.1374	0.5939	0.2476	0.4542	0.2134	0.3083		47
Vessel Density	0.6139	0.0504	**0.0005**	0.0831	0.1520	0.4694	0.6300	0.7946	0.1147	0.8907	0.2522	**<0.0001**	

(B) Saline (HA present)

	T_1	T_2	MTR	ADC	R_2*	G_d	G_l	|G*|	Y	Nuclear Density	HA	Collagen	Vessel Density
T_1		23	23	21	23	21	21	21	21	23	23	23	23
T_2	0.1474		23	21	23	21	21	21	21	23	23	23	23
MTR	0.5661	**<0.0001**		27	23	27	27	27	27	29	29	29	23
ADC	0.8149	0.6623	0.8709		21	25	25	25	25	27	27	27	21
R_2*	0.4312	0.4433	0.4887	0.3843		21	21	21	21	23	23	23	23
G_d	0.6554	0.0701	**0.0197**	0.5721	0.4430		27	27	27	27	27	27	21
G_l	0.9780	0.0936	**0.0359**	0.2407	0.4458	**<0.0001**		27	27	27	27	27	21
|G*|	0.7545	0.0679	**0.0195**	0.4891	0.4112	**<0.0001**	**<0.0001**		27	27	27	27	21
Y	0.3078	0.5360	0.6290	0.3816	0.9103	**0.0314**	**<0.0001**	**0.0065**		27	27	27	21
Nuclear Density	**0.0081**	0.9524	0.5289	0.0503	0.9013	0.5357	0.8720	0.6954	0.1130		29	29	23
HA	0.0744	0.2037	0.4180	0.4270	0.5126	0.8765	0.7643	0.9063	0.5890	0.4663		29	23
Collagen	0.7513	0.4384	**0.0493**	0.6923	0.9812	**0.0222**	0.2138	**0.0412**	0.6466	0.5605	0.1212		23
Vessel Density	0.0708	0.8813	0.2163	0.5367	0.8675	**0.0471**	0.2041	0.0673	0.9911	0.5415	**0.0001**	0.0001	

(C) PEGPH20 (HA degraded)

	T_1	T_2	MTR	ADC	R_2*	G_d	G_l	|G*|	Y	Nuclear Density	HA	Collagen	Vessel Density
T_1		24	24	23	24	22	22	22	22	24	X	24	24
T_2	**0.0127**		24	23	24	22	22	22	22	24	X	24	24
MTR	0.9659	**0.0005**		27	24	26	26	26	26	28	X	28	24
ADC	0.5283	**0.0048**	**0.0032**		23	25	25	25	25	27	X	27	23
R_2*	0.7501	0.4771	0.5495	0.1845		22	22	22	22	24	X	24	24
G_d	0.6707	0.9984	0.8040	0.4957	0.1866		26	26	26	26	X	26	22
G_l	0.8966	0.6632	0.3517	0.3576	0.1155	**<0.0001**		26	26	26	X	26	22
|G*|	0.7408	0.6574	0.4791	0.3529	0.1046	**<0.0001**	**<0.0001**		26	26	X	26	22
Y	0.4195	0.3468	0.1059	0.5386	0.1774	**0.0366**	**<0.0001**	**0.0069**		26	X	26	22
Nuclear Density	0.1040	0.5262	0.3944	0.9420	0.2009	**0.0079**	**0.0052**	**0.0052**	0.1341		X	28	24
HA	X	X	X	X	X	X	X	X	X	X		X	X
Collagen	0.5289	**0.0489**	**0.0083**	**0.0031**	0.1418	0.5717	0.3387	0.4057	0.3739	0.1398	X		24
Vessel Density	0.6092	**0.0057**	**<0.0001**	**0.0004**	**0.0478**	0.3966	0.0712	0.1560	**0.0132**	0.7788	X	**0.0009**	

Figure 6.3: *Sample sizes (blue) and p-values (red) for the correlation matrices of MRI biomarkers (T_1, T_2, MTR, ADC, R_2*, G_d, G_l, \|G*\|, and Y) and matched histological staining shown in Figure 6.2. Relationships were evaluated with all data pooled together* ***(A)****, and with saline* ***(B)*** *and PEGPH20 treated* ***(C)*** *tumour data kept separate. Significant p-values are shown in bold ($p < 0.05$).*

6.2.1 Correlations between MRI biomarkers

T_2 negatively correlated with MTR in all cases whether saline and PEGPH20 data were evaluated together or kept separate (Figures 6.2 and 6.4; all data: $n = 47$, $r = -0.74$, $p < 0.0001$). This relationship has been noted previously in healthy brain and disease states including multiple sclerosis and gliomas[237-239]. MTR is sensitive to the proportion of macromolecules within tissue, with more macromolecule content contributing to more magnetisation transfer and a higher MTR value. T_2 is a less direct measure of this, however, water molecules bound to macromolecules have rapid T_2 signal decay and so contribute to a shorter T_2 relaxation time.

When HA was present in the tumour, MTR positively correlated with G_d (Figures 6.2b and 6.4; saline data: $n = 27$, $r = 0.45$, $p = 0.02$). However, in tumours where HA was degraded by PEGPH20, this relationship disappeared. HA degradation may alter the tumour microenvironment such that MTR and G_d are no longer sensitive to the same tumour properties. Later in this Chapter, consideration of the underlying biology with MRI-aligned histology will help to identify which components MTR and G_d are sensitive to and how these differ in saline and PEGPH20 treated tumours.

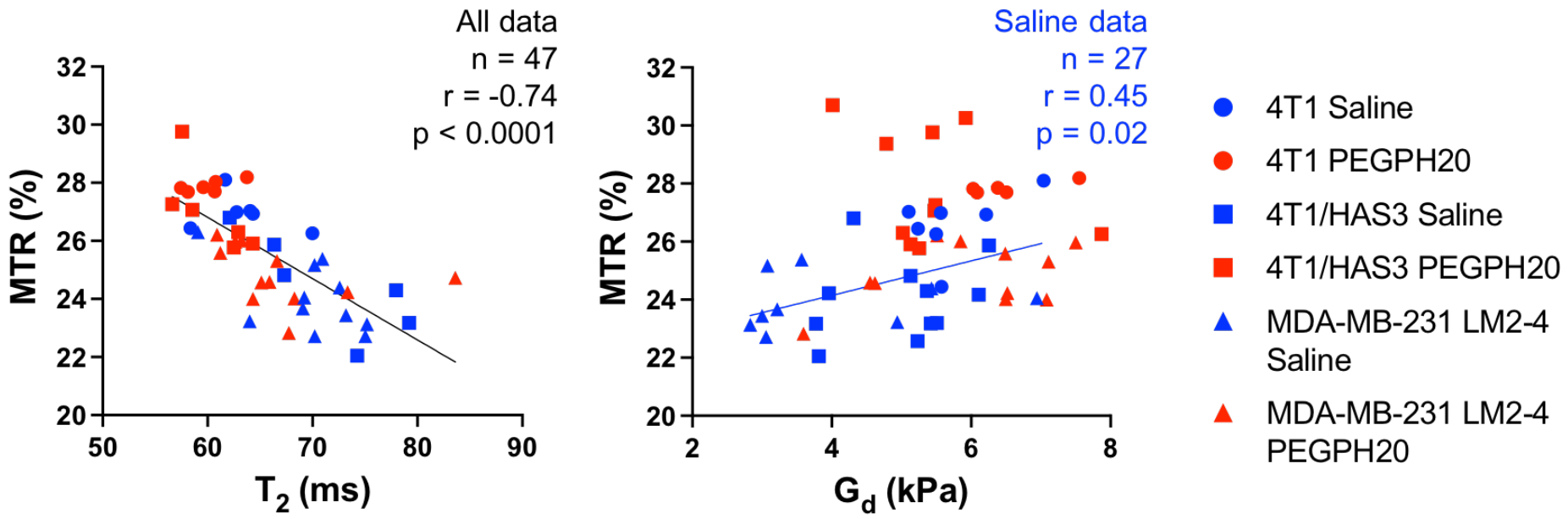

Figure 6.4: *Correlations between MRI biomarkers in saline (HA present) and PEGPH20 treated (HA degraded) 4T1, 4T1/HAS3, and MDA-MB-231 LM2-4 breast tumours. Saline control and PEGPH20 treated tumour data are shown in blue and red respectively, with different shaped symbols indicating the different breast tumour models. The sample size (n), Pearson's correlation coefficient (r), and p-value are shown by the linear regression they relate to.*

6.2.2 Correlations between MRI biomarkers and nuclear density

Nuclear density was used throughout this project as an estimate of tumour cellularity because it is easy to quantify from H&E staining, the limitation being that cells can occasionally contain multiple nuclei.

In saline and PEGPH20 treated tumours, T_1 negatively correlated with nuclear density (Figures 6.2 and 6.5; all data: n = 47, r = -0.44, p = 0.002). T_1 is sensitive to the bound to free water ratio within tissue, with bound water having a shorter T_1 than free water. Increased cellularity will likely accompany an increased density of hydrophilic components such as proteins and polysaccharides which bind water molecules and reduce T_1 relaxation time within the tumour.

In saline control tumours, ADC negatively correlated with nuclear density (Figures 6.2b and 6.5; n = 27, r = -0.38, p = 0.05). Similar relationships between ADC and cellularity have been previously reported in several tumour types, including breast cancer[240, 241]. Increased cell density will increase barriers and restrict water diffusion, and thus decrease ADC. Interestingly, when HA was degraded in PEGPH20 treated tumours ADC was no longer related to nuclear density. This demonstrates that ADC is not always a biomarker of cellularity in a tumour and is presumably also influenced by other tumour characteristics[240]. Degradation of HA leads to reduction of the extracellular space bringing many components of the tumour (e.g. cells, stroma, and blood vessels) closer together, which will restrict movement of water in a way not only related to tumour cellularity.

In saline control tumours, cellularity did not influence tumour viscoelastic properties, in agreement with previous pre-clinical work[46]. However, in PEGPH20 treated tumours, G_d positively correlated with nuclear density (Figures 6.2c & 6.5; n = 26, r = 0.51, p = 0.008). HA degradation affects the integrity of the ECM, reducing the ability of fibrillar collagen and blood vessels to increase tumour stiffness. As a result, the viscoelastic properties of PEGPH20 treated tumours are reliant on the cellular network.

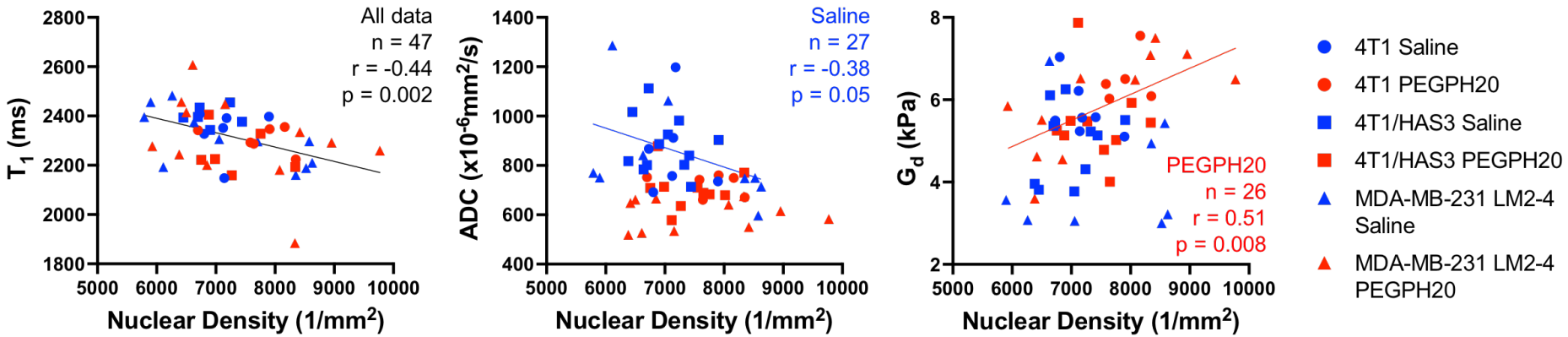

Figure 6.5: *Correlations between MRI biomarkers and nuclear density (quantified from H&E staining) in saline (HA present) and PEGPH20 treated (HA degraded) 4T1, 4T1/HAS3, and MDA-MB-231 LM2-4 breast tumours. Saline control and PEGPH20 treated tumour data are shown in blue and red respectively, with different shaped symbols indicating the different breast tumour models. The sample size (n), Pearson's correlation coefficient (r), and p-value are shown by the linear regression they relate to.*

6.2.3 Correlations between MRI biomarkers and HA

There were no significant correlations between MRI biomarkers and percent HA when using saline data in isolation (Figure 6.2b, 6.3b & 6.6; $p>0.05$). The MRI biomarkers evaluated may be sensitive, but they are not specific to HA and can be influenced by other tumour characteristics. To further understand whether these biomarkers are truly sensitive to HA, PEGPH20 treated data were also included as effective 'low HA' values. This approach reduced the influence of other tumour characteristics to the correlation and increased the range of percent HA values available. When analysing saline and PEGPH20 treated data together, percent HA significantly correlated with T_2, MTR and ADC (Figure 6.6).

ADC exhibited the strongest, positive correlation with percent HA (Figures 6.2a & 6.6; all data: $n = 54$, $r = 0.60$, $p < 0.0001$), reaffirming the conclusion from Chapter 3 that ADC is the most sensitive biomarker of tumour response to PEGPH20, possibly because of its sensitivity to the size of the extracellular space. This finding was corroborated by clinical data from patients bearing tumours from other anatomical sites including colon, lung and pancreas[242].

T_2 and MTR are other, less specific, parameters related to percent HA, again possibly due to being sensitive to the size and composition of the extracellular space. T_2 positively correlated with HA (all data: $n = 47$, $r = 0.44$, $p = 0.002$). MTR negatively correlated with HA (all data: $n = 57$, $r = -0.46$, 0.0003). Greater HA accumulation is expected to result in elevated fluid retention, as well as extracellular expansion which should regulate the amount of free water, thus increasing T_2 and attenuating the effect of MT-inducing components of the ECM such as fibrillar collagen.

Saline control 4T1 tumours showed the greatest intra-tumour heterogeneity in HA accumulation, and within this model the relationships between ADC, T_2, and HA were seen spatially within a tumour (Figure 6.7). Despite the numerical inter-tumour association, areas of high HA accumulation were not visibly associated with low MTR and vice versa

(Figure 6.7a & c). There were some 4T1 tumour areas with high and low HA accumulation which aligned with high and low T_2 (green and blue arrows respectively, Figure 6.7a & b). However, in other tumour regions, T_2 and HA appeared unrelated (yellow arrow, Figure 6.7b). As well as having the strongest numerical inter-tumour association, visual comparison of ADC maps with HA staining images revealed that tumour regions with high ADC also had high HA accumulation and vice versa (all green and blue arrows; Figure 6.7a & d).

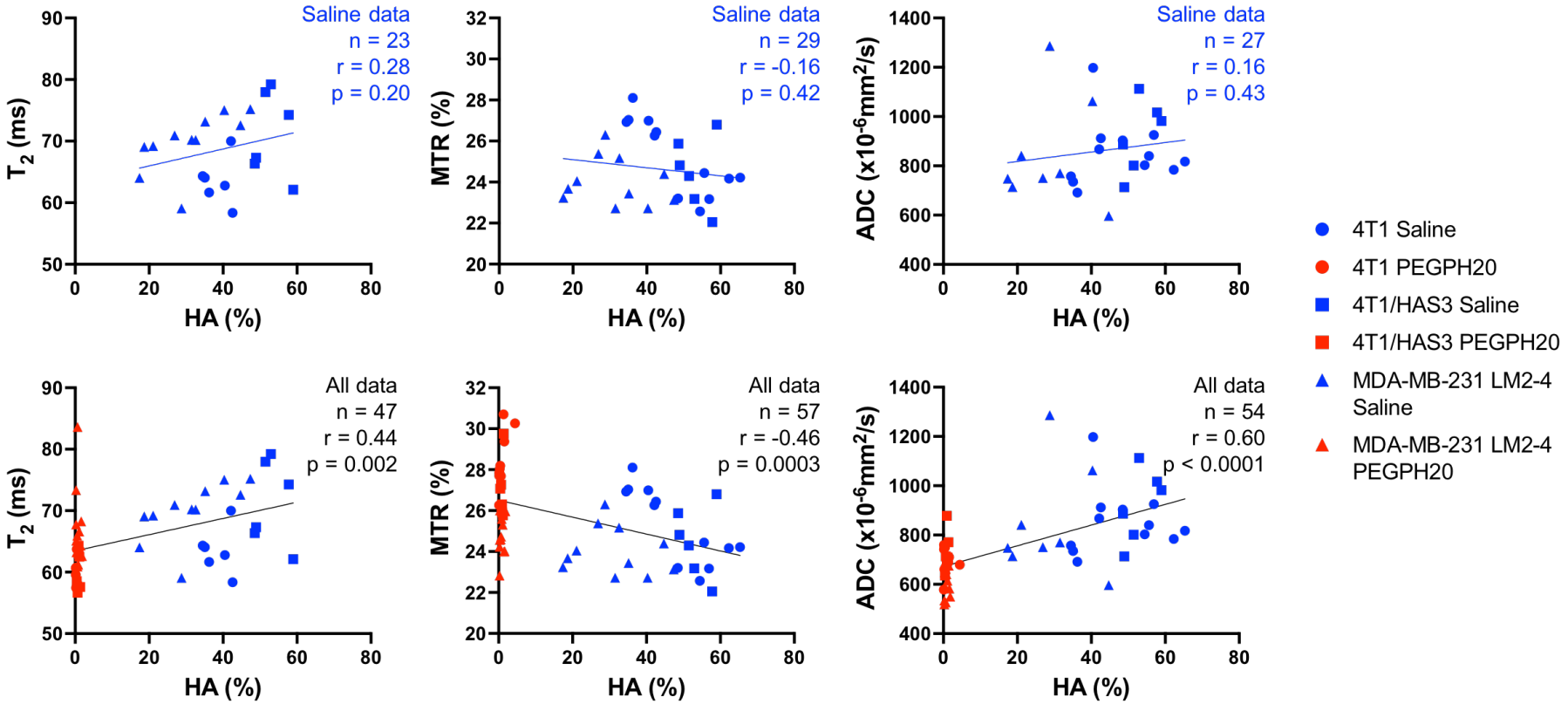

Figure 6.6: *Correlations between MRI biomarkers and percent HA (quantified from HTI-601 staining) in saline (HA present) and PEGPH20 treated (HA degraded) 4T1, 4T1/HAS3, and MDA-MB-231 LM2-4 breast tumours. Saline control and PEGPH20 treated tumour data are shown in blue and red respectively, with different shaped symbols indicating the different breast tumour models. The sample size (n), Pearson's correlation coefficient (r), and p-value are shown by the linear regression they relate to.*

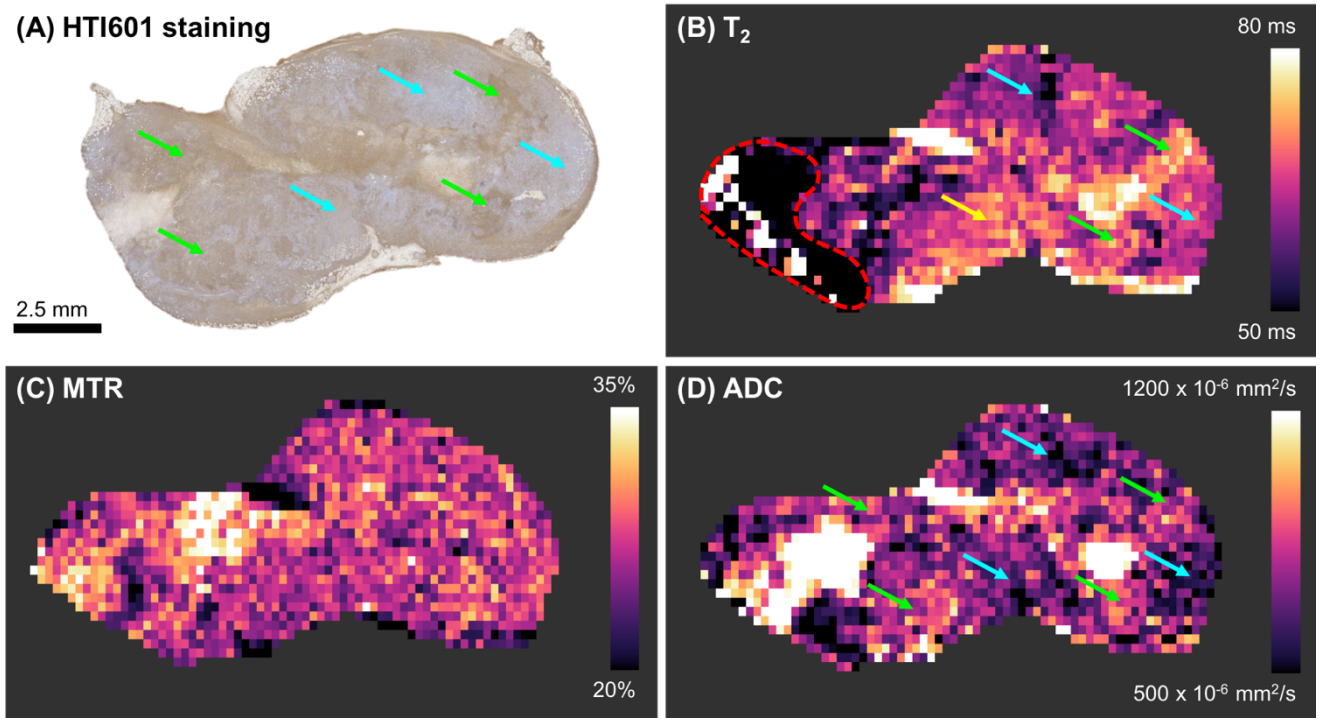

Figure 6.7: *A HTI-601 (HA) stained section* ***(A)*** *alongside matched parametric maps of T_2* ***(B)****, MTR* ***(C)****, and ADC* ***(D)*** *for one saline control 4T1 tumour with representative intra-tumour heterogeneity in HA accumulation for this model. Spatial associations between T_2, ADC, and HA were apparent, with areas of high HA accumulation corresponding to areas of high T_2 and ADC (green arrows) and regions of low HA related to areas of low T_2 and ADC (blue arrows). Some regions of the T_2 map appeared unrelated to HA accumulation (yellow arrow). Tumour areas with high HA accumulation did not correspond to low MTR as suggested by the inter-tumour correlation in Figure 6.6. An artefact on the T_2 map was excluded from analyses (red dashed ROI).*

6.2.4 Correlations between MRI biomarkers and collagen

MTR positively correlated with collagen content in both saline and PEGPH20 treated tumours (Figure 6.8; saline: n = 29, r = 0.37, p = 0.05 and PEGPH20: n = 28, r = 0.49, p = 0.008). Whilst HA degradation increases MTR, as shown by an upward shift in the trendline of PEGPH20 treated tumours, it does not affect the sensitivity of MTR to collagen deposition.

Surprisingly, when analysing all the data (saline and PEGPH20 treated tumours) collagen did not appear a major determinant of tumour viscoelastic properties, contrary to previous observations (Figure 6.2a)[46, 235, 243]. When only saline control tumours were considered, G_d positively correlated with collagen content (Figure 6.8; G_d: n= 27, r = 0.44, p = 0.02), thus supporting the hypothesis that collagen is a major determinant of MRE-derived tumour elastic properties, consistent with previous work[46]. In PEGPH20 treated tumours where HA had been degraded, G_d was not significantly associated with collagen content (Figures 6.2c & 6.8). The lack of correlation between G_d and collagen in PEGPH20 treated tumours suggests that HA degradation has downstream effects on the structure-function of collagen or more generally the mechanical integrity of the ECM.

In PEGPH20 treated tumours, ADC positively correlated with collagen content (Figures 6.2c & 6.8; PEGPH20 data: n = 27, r = 0.55, p = 0.003). This relationship has been previously shown in clinical breast tumours and is likely to result from increased water diffusion along the direction of the collagen fibres[241, 244]. These data support the conclusion that collagen fibres remain in the extracellular space following HA degradation by PEGPH20, however, as shown by the G_d data above, its ability to influence tumour stiffness is dampened.

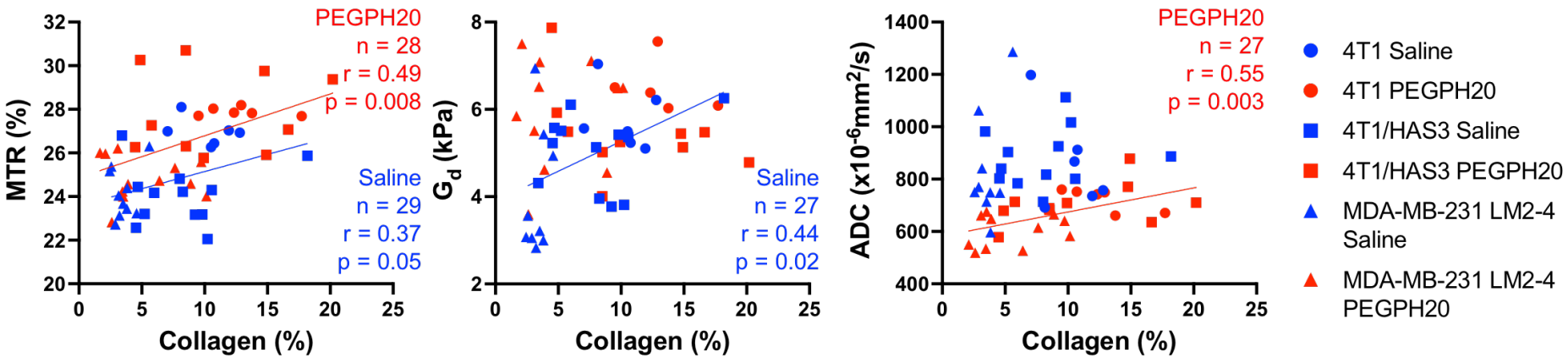

Figure 6.8: *Correlations between MRI biomarkers and collagen content (quantified from picrosirius red staining) in saline (HA present) and PEGPH20 treated (HA degraded) 4T1, 4T1/HAS3, and MDA-MB-231 LM2-4 breast tumours. Saline control and PEGPH20 treated tumour data are shown in blue and red respectively, with different shaped symbols indicating the different breast tumour models. The sample size (n), Pearson's correlation coefficient (r), and p-value are shown by the linear regression they relate to.*

6.2.5 Correlations between MRI biomarkers and blood vessel density

In PEGPH20 treated tumours, blood vessel density negatively correlated with T_2 ($n = 24$, $r = 0.55$, $p = 0.006$) and positively correlated with MTR and ADC (Figures 6.2c & 6.9; MTR: $n = 24$, $r = 0.74$, $p < 0.0001$ and ADC: $n = 23$, $r = 0.68$, $p = 0.0004$). The basement membrane of blood vessels contains various ECM proteins and so more blood vessels will likely be associated with a higher proportion of water bound to macromolecules and more barriers to water diffusion. As mentioned in section 6.2.1, a greater proportion of macromolecules within tissue can increase MTR and decrease T_2. None of these associations are seen in saline control tumours where HA is present. As ADC, MTR and T_2 are affected by HA accumulation (Figure 6.6), it may be that HA elicits a stronger affect than blood vessels and it is only when HA is degraded by PEGPH20 that the contribution of blood vessels on ADC, MTR and T_2 becomes clear.

R_2* is sensitive to the paramagnetic deoxyhaemoglobin present in perfused tumour blood vessels. CD31 is expressed on all blood vessels, both perfused and non-perfused. Thus, it is not surprising that, in saline control tumours, R_2* is not associated with blood vessel density quantified from CD31 staining (Figures 6.2b & 6.9). However, in PEGPH20 treated tumours where blood vessels have likely decompressed, R_2* positively correlated with blood vessel density (Figure 6.9; $n = 24$, $r = 0.41$, $p = 0.05$). When blood vessels are decompressed, CD31 expression is more likely to mirror R_2* signal, assuming the decompressed vessel lumen size is sufficient to enable transit of RBCs (~6 μm), the source of R_2* contrast.

In saline control tumours, G_d positively correlated with vessel density ($n = 21$, $r = 0.44$, $p = 0.05$). This is consistent with previous work demonstrating the ability of blood vessels to alter the shear modulus, with the presence of vascular outgrowths resulting in increased shear wave speed and thus higher G_d[245]. Similar to the relationship between G_d and collagen, when HA was degraded in PEGPH20 treated tumours, the association between G_d and blood vessels diminished.

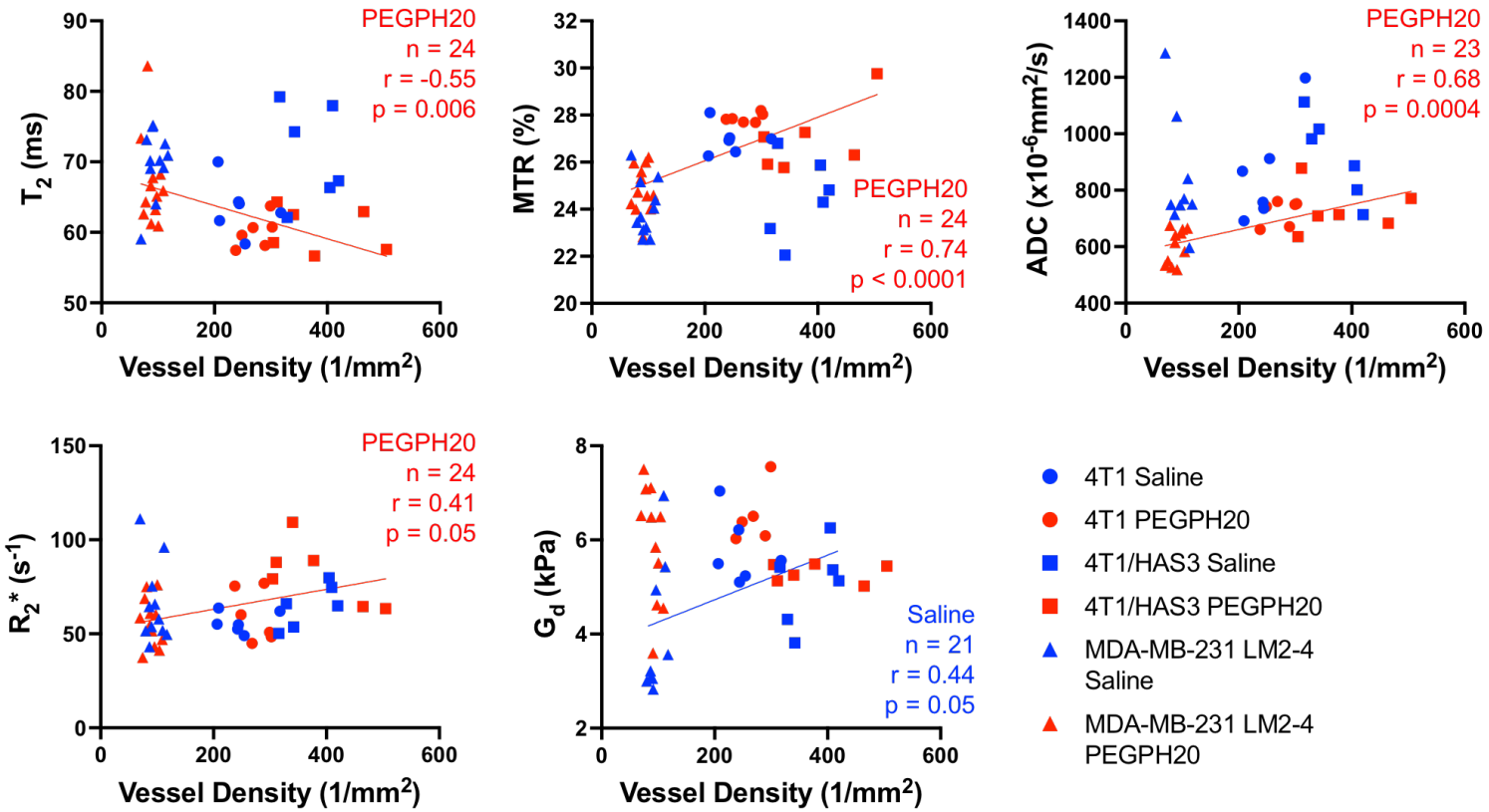

Figure 6.9: *Correlations between MRI biomarkers and blood vessel density (quantified from CD31 staining) in saline (HA present) and PEGPH20 treated (HA degraded) 4T1, 4T1/HAS3, and MDA-MB-231 LM2-4 breast tumours. Saline control and PEGPH20 treated tumour data are shown in blue and red respectively, with different shaped symbols indicating the different breast tumour models. The sample size (n), Pearson's correlation coefficient (r), and p-value are shown by the linear regression they relate to.*

6.3 Summary & Conclusion:

ADC exhibited the strongest correlation with percent HA, whilst concomitantly showing a negative correlation with cellularity. This reinforces the ability of ADC to inform on HA accumulation and its degradation by PEGPH20, probably because of the sensitivity of ADC to the size of the extracellular space. T_2 and MTR should also be sensitive to the size and composition of the extracellular space but here had weaker associations with percent HA.

Collagen was an important contributor to tumour viscoelastic properties in saline control tumours, consistent with previous studies[46, 235, 243]. Despite collagen fibres remaining in the extracellular space following HA degradation, as confirmed by picrosirius red staining and the correlation of collagen content with ADC, collagen itself seemingly did not significantly affect tumour viscoelasticity in PEGPH20 treated tumours. Similar correlations were seen between G_d and blood vessel density, with a significant positive correlation in saline controls and no relationship in PEGPH20 treated tumours. In PEGPH20 treated tumours, G_d was instead correlated with nuclear density. These data suggest that HA degradation by PEGPH20 can suppress the contribution of collagen and blood vessels to tumour viscoelastic properties, likely due to loss of connection between HA and other ECM components. This may disrupt the mechanical integrity of the ECM and shift the sensitivity of G_d towards the remaining intact cell network. A summary schematic is shown in Figure 6.10.

In conclusion, these data support ADC as the most sensitive biomarker of tumour response to PEGPH20 and, although HA does not directly correlate with tumour biomechanical properties, its rapid degradation by PEGPH20 appears to influence whether tumour stiffness is determined by the extracellular (collagen and blood vessels) or cellular compartment of a tumour.

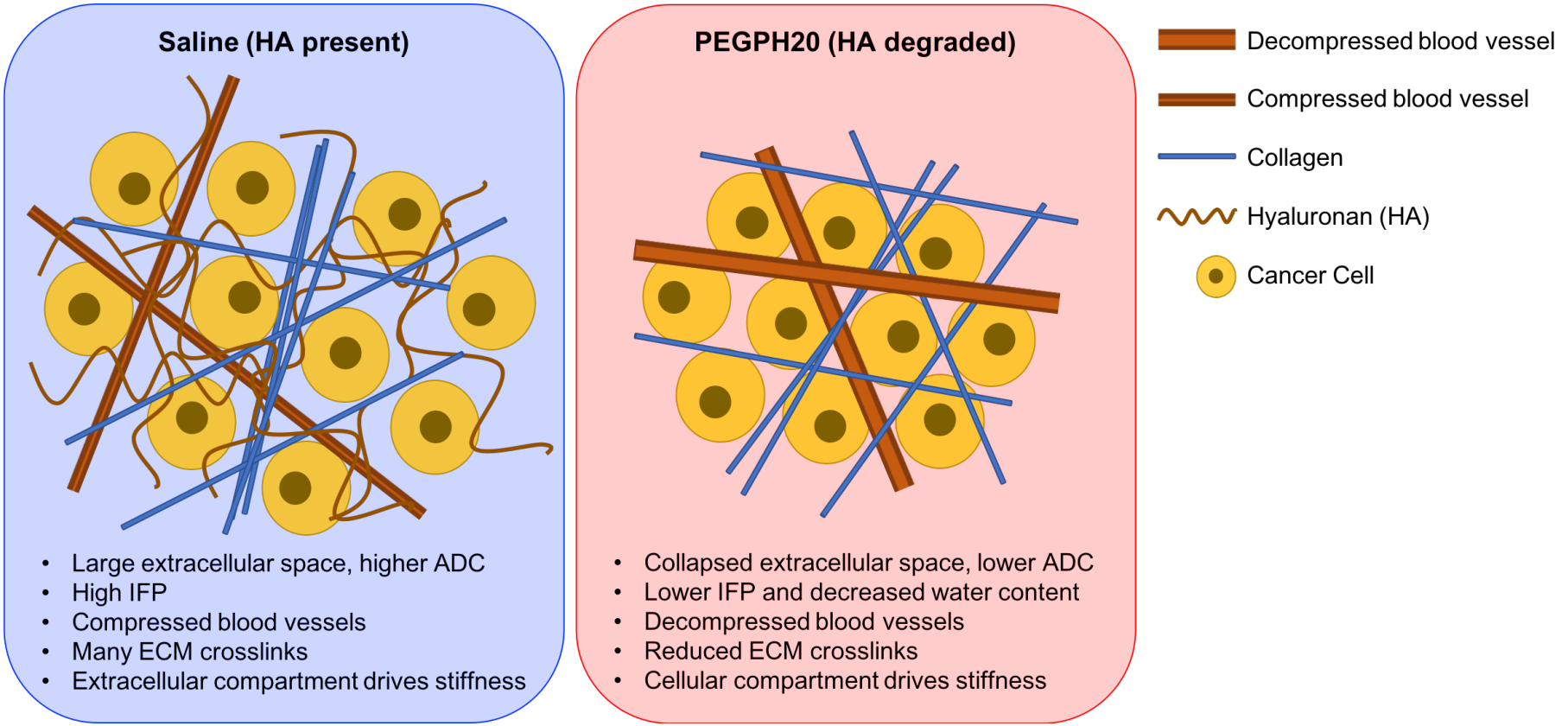

Figure 6.10: *A simplified graphic summarising the hypothesised explanation for the different characteristics of pre-clinical breast tumours treated with either saline (HA present; blue) or PEGPH20 (HA degraded; red). ADC = the apparent diffusion coefficient. IFP = interstitial fluid pressure. ECM = extracellular matrix.*

Chapter 7: Summary and Conclusions

7.1 Summary of results:

7.1.1 ADC can inform on HA accumulation and its therapeutic modulation by PEGPH20

The ability of T_1, T_2, MTR and ADC to inform on breast tumour response to PEGPH20 was assessed. T_1, T_2, and ADC decreased, and MTR increased following PEGPH20 treatment in 4T1/HAS3 tumours. ADC decreased in MDA-MB-231 LM2-4 tumours following PEGPH20, but no significant change was seen in T_1, T_2, or MTR. No significant changes in T_1, T_2, MTR or ADC were seen in 4T1 breast tumours following PEGPH20 treatment. 4T1/HAS3 tumours had the highest HA accumulation at baseline and so likely experienced the biggest biophysical changes occurring following HA degradation. MDA-MB-231 LM2-4 tumours had lower baseline HA accumulation and ADC was able to inform on a more subtle yet significant response to PEGPH20. Despite no significant change in ADC following PEGPH20 treatment, there was intra-tumour spatial correspondence between ADC and HA in saline control 4T1 tumours.

When evaluating median values from all tumours, ADC exhibited the strongest correlation with percent HA, suggesting that ADC is the most sensitive biomarker of HA accumulation and can reliably inform on its therapeutic modulation by PEGPH20. T_2 and MTR had weaker correlations with percent HA, suggesting they are sensitive but less specific to HA accumulation and the size and composition of the extracellular space.

Recent clinical data from patients bearing solid tumours, including colon, lung, bladder and pancreatic cancer, revealed that, despite administration of a lower clinical dose, ADC also decreased by approximately 20% one day after PEGPH20 monotherapy[242]. The absence of any ADC dose response despite the very different treatment regimens used pre-clinically

(1 mg/kg) and clinically (0.5 – 50 μg/kg) is not hugely surprising, as PEGPH20 is an enzyme and, unlike other therapies, is not depleted upon interaction with its target[242].

A common limitation with many of the MRI biomarkers evaluated, including ADC, is that they are sensitive to HA but are not completely specific and so they can also be affected by other biological phenomena within the tumour. In this thesis, the use of PEGPH20 as a monotherapy and relative changes between pre- and post-treatment MRI likely reduced the influence of other tumour characteristics on the MRI biomarkers. Further work should consider the recommended use of PEGPH20 in a combination treatment strategy and evaluate whether a decrease in ADC can still be seen following PEGPH20 when it is used alongside chemo-, radio- or immunotherapy, treatments that typically result in tumour cell death and hence an increase in ADC. If a decrease in ADC is no longer evident, an appropriate timepoint for imaging would need to be established which is soon after HA degradation by PEGPH20 and prior to administration of the combination therapy.

7.1.2 HA degradation by PEGPH20 can increase tumour viscoelasticity as measured by MRE

Whilst there was no change in the viscoelastic properties of 4T1 and 4T1/HAS3 tumours, PEGPH20 induced an unprecedented ~80% increase in G_d, G_l, and $|G^*|$ in MDA-MB-231 LM2-4 tumours. No changes in Y were apparent.

Collagen positively correlated with tumour viscoelastic properties in saline control tumours, consistent with our previous study[46]. Despite collagen fibres remaining in the extracellular space following HA degradation, collagen did not correlate with tumour viscoelasticity in PEGPH20 treated tumours. Similarly, blood vessel density positively correlated with G_d in saline control tumours, but no relationship was seen in PEGPH20 treated tumours. In PEGPH20 treated tumours, G_d was instead correlated with

nuclear density. These data suggest that HA degradation by PEGPH20 can suppress the contribution of collagen and blood vessels to tumour viscoelastic properties, likely due to disruption of ECM integrity, and a shift in the sensitivity of G_d towards the aggregated cellular compartment.

HA did not directly correlate with tumour viscoelastic properties; however, it can influence whether G_d is determined by the extracellular or cellular compartment of a tumour. MRE is unlikely to provide a biomarker of tumour response to PEGPH20 but can inform on pharmacologically-induced increases in tumour stiffness. Quantitation of G_d, G_l and $|G^*|$ should thus continue to be evaluated as binary imaging biomarkers of tumour treatment response.

7.1.3 R_2* can inform on vascular response to PEGPH20 in well vascularised tumours with high HA accumulation

R_2* significantly increased following PEGPH20 treatment in 4T1/HAS3 tumours, however, no change was seen in 4T1 and MDA-MB-231 LM2-4 tumours. The increase in 4T1/HAS3 tumour R_2* is consistent with decompression of blood vessels and increased accessibility of RBCs. The lack of change in 4T1 and MDA-MB-231 LM2-4 tumour R_2* following PEGPH20 may suggest that vessel decompression is not always correlated with an increase in deoxygenated haemoglobin and/or RBCs, or that decompression of a smaller number of blood vessels does not create a large enough change in magnetisation to be detected by R_2*. The capillary network in tumours is chaotic and often capillary lumens are similar in size to RBCs (approximately 6 μm diameter), thus preventing RBC movement and hence a change in R_2* even when decompressed[201].

R_2* is a sensitive endogenous imaging biomarker of tumour vascular response to PEGPH20 in well vascularised tumours with high HA accumulation. However, CE-MRI may provide more specific biomarkers of PEGPH20 response in relatively hypovascular tumours with less HA accumulation.

7.1.4 Impact for patients living with cancer

ADC can be estimated on most modern clinical MRI scanners with good repeatability and reproducibility[171]. Therefore, ADC could be used immediately to monitor response to HA modulation in clinical trials. Following some further work to confirm sensitivity, ADC could also be used relatively quickly to monitor tumour response in clinical trials of therapies predicted to alter the size or composition of the extracellular space.

MRE can inform on tumour response to effective therapy, typically seen as a decrease in tumour stiffness following tumour cell death[74, 157, 198]. The data herein support the use of G_d, G_l and $|G^*|$ to inform on increased tumour stiffness, for example following response to immunotherapy[246]. Immunotherapies have demonstrated survival benefit across various cancer types, however durable responses are only seen in a small proportion of patients and there is a need for biomarkers that identify patient response[247]. Localised regions with elevated stiffness have been associated with increased immune cell infiltration in human breast tumours[5]. Moreover, increased MRE-derived tumour stiffness was associated with improved overall survival in a small number of patients with hepatocellular carcinoma (HCC) treated with the immunotherapy Pembrolizumab[246]. Expansion of this research to evaluate the ability of MRE to detect tumour response to immunotherapy in a wider range of cancer types would be hugely beneficial to clinicians and patients.

7.2 Future work

7.2.1 Further analysis of the multiparametric MRI and matched histology datasets

The multiparametric MRI protocol, which was designed using MRI sequences previously optimised by other members of the team, enabled detailed spatial comparisons between different MRI biomarkers, and

between MRI and the underlying histology. Fairly large datasets were created throughout this PhD and should be further used to understand more about the histological determinants of breast cancer which underly the MRI biomarkers. This information would assist with translation of MRI biomarkers into the clinic. The oncological application of MRE in the clinic is still in its relative infancy, though vendor support for MRE capability on clinical scanners is increasing. Information on how necrosis, for example, may impact tumour viscoelastic properties will help increase its clinical adoption as a measure of tumour cell death following therapy.

Computational methods would remove the bias which accompanies visual assessment of intra-tumour spatial comparisons between MRI biomarkers and histology. This has been done in other studies and involves the generation of histological feature maps with the same resolution as the MRI and use of a registration algorithm[46, 202].

Throughout this thesis the value of each MRI biomarker was assessed individually. Combining the information provided by multiple biomarkers through a habitat imaging approach may improve the specificity of the MRI protocol to HA and its therapeutic modulation[248]. For instance, a tumour habitat with high ADC, low MTR, and high T_2 may better associate with regions of high HA accumulation than one biomarker alone.

7.2.2 Evaluation of MRI histology associations following knock-down or long-term degradation of HA

This thesis evaluated rapid degradation of HA using a single intravenous dose of PEGPH20 (1 mg/kg) and a 24-hour timepoint. A follow up study which uses the same breast tumour models but with a knock-down of HA synthases or continuous treatment with PEGPH20 would assess the longer-term impact of HA absence on the correlations between ECM components and tumour characteristics, with the association between collagen and viscoelastic properties being of particular interest.

7.2.3 Other MRI biomarkers which may inform on tumour response to PEGPH20

SC-MRI can estimate fractional tumour blood volume (%) and vessel size (μm) by measuring USPIO-induced changes in the transverse relaxation rates R_2 and R_2*[162, 163, 201, 207]. A recent study showed that SC-MRI-derived fractional blood volume increased ~40% following two doses of PEGPH20 monotherapy in a pre-clinical model of pancreatic cancer[209]. SC-MRI may provide a more robust method of evaluating tumour blood vessel decompression following PEGPH20, as the paramagnetic signal from intravascular USPIO particles is not affected by hypoxia, and USPIO particles are much smaller (~25-30 nm diameter) than RBCs, thereby negating the capillary accessibility issue. Accurate monitoring of blood vessel decompression is very important for predicting drug delivery and response. Use of SC-MRI following PEGPH20 monotherapy may help identify the optimal time for administration of a combination therapy and improve patient outcomes.

PEGPH20 treatment can reduce tumour hypoxia and sensitise tumours to radiotherapy[230, 249]. Imaging tumour hypoxia was not explored in this thesis, but methods do exist which may inform on PEGPH20-induced changes in tumour hypoxia. IS-MRI can inform on tissue oxygenation through measurement of R_2* prior to and during hyperoxic gas challenge[165-167, 201]. Blood vessels within hypoxic areas have a higher baseline R_2* because they contain more deoxyhaemoglobin. Hypoxic regions are likely to show a larger reduction in R_2* following hyperoxic gas challenge compared to normoxic tissues which display little change in R_2*[250]. Oxygen Enhanced (OE)-MRI can map tumour hypoxia by utilising the sensitivity of R_1 ($1/T_1$) to the partial pressure of oxygen (pO_2)[236, 251]. R_1 increases in well oxygenated tissues following hyperoxic gas challenge because haemoglobin is completely saturated and excess oxygen remains in the blood plasma and tissue fluid. Haemoglobin is not fully saturated in hypoxic tissues and so hyperoxic gas challenge increases oxyhaemoglobin

but has little effect on pO_2 and R_1. When combined with an MRI biomarker of perfusion, perfused tumour sub-volumes refractory to hyperoxia-induced changes in R_1 have been shown to be hypoxic[251].

7.2.4 Relevance of MRI biomarkers to other stromal modulatory therapies

The MRI biomarkers, T_2, MTR, ADC, G_d, G_l, and $|G^*|$ were all sensitive to the size and/or composition of the extracellular space. In the case of HA degradation ADC was the most robust, however any of these MRI biomarkers may be useful in understanding and assessing tumour response to other stromal modulatory therapies currently under clinical development, such as losartan (TGF-β) and fasudil (ROCK inhibitor). Recently there has been a lot of interest in therapeutically targeting cancer associated fibroblasts (CAFs) which play a fundamental role in ECM production and organisation[252]. MRI biomarkers which can detect early tumour response could accelerate the clinical development and hopefully improve the success of stromal modulatory therapies.

7.2.5 HA degradation as a therapeutic strategy

Stomal modulatory therapies have been described as a double-edged sword because of their potential to suppress tumour progression through enhancement of drug delivery, yet promote tumour progression by removing barriers to invasion and metastasis[41, 57, 107, 253].

The failure of PEGPH20 to improve overall survival of patients with HA 'high' metastatic PDAC in the phase III trial HALO-109-301 highlights that much is still to be learnt about stromal modulatory therapies and patient selection[139, 145]. Given that increased tumour stiffness can contribute to tumour progression, the elevated G_d, G_l, and $|G^*|$ observed in PEGPH20 treated MDA-MB-231 LM2-4 tumours may indicate a potentially negative, tumour-promoting effect of PEGPH20. Future work should evaluate

whether PEGPH20 treatment has a detrimental effect in other models of stromal-dense cancer and assess how this would translate to patients.

It is unclear why the phase III trial of PEGPH20 failed to improve patient survival. If PEGPH20 effectively degraded HA and improved tumour drug delivery but increasing the concentration of chemotherapy in the pancreatic tumour microenvironment was not enough to improve overall survival, then degradation of HA may still be a viable therapeutic strategy in other settings. HA degradation may be particularly useful when delivering larger biologic treatments such as antibodies and virotherapies, with recent data highlighting that combination of a hyaluronidase with virotherapy improved survival in a pre-clinical model of glioma[146].

7.3 Conclusion

In conclusion, through its sensitivity to the size and composition of the extracellular space, ADC can reliably inform on tumour HA accumulation and its therapeutic degradation by PEGPH20. This thesis demonstrated that multiparametric MRI investigations alongside matched histology provide an understanding of what tumour tissue components underpin the MRI biomarkers and give confidence that the useful biomarker(s) identified are more sensitive than the other clinically available biomarkers evaluated. Both biological understanding and comparison with other biomarkers will improve the chances of successful clinical implementation of imaging biomarkers as practice-changing tools that enable personalised adaptation to treatment.

References

1. Torre, L.A., et al., *Global cancer statistics, 2012.* CA Cancer J Clin, 2015. **65**(2): p. 87-108.

2. Insua-Rodríguez, J. and T. Oskarsson, *The extracellular matrix in breast cancer.* Advanced Drug Delivery Reviews, 2016. **97**(Supplement C): p. 41-55.

3. Conklin, M.W. and P.J. Keely, *Why the stroma matters in breast cancer: Insights into breast cancer patient outcomes through the examination of stromal biomarkers.* Cell Adhesion & Migration, 2012. **6**(3): p. 249-260.

4. Soysal, S.D., A. Tzankov, and S.E. Muenst, *Role of the Tumor Microenvironment in Breast Cancer.* Pathobiology, 2015. **82**(3-4): p. 142-52.

5. Acerbi, I., et al., *Human breast cancer invasion and aggression correlates with ECM stiffening and immune cell infiltration.* Integr Biol (Camb), 2015. **7**(10): p. 1120-34.

6. Boyd, N.F., et al., *Heritability of mammographic density, a risk factor for breast cancer.* N Engl J Med, 2002. **347**(12): p. 886-94.

7. Northey, J.J., et al., *Stiff stroma increases breast cancer risk by inducing the oncogene ZNF217.* The Journal of Clinical Investigation, 2020. **130**(11): p. 5721-5737.

8. Frantz, C., K.M. Stewart, and V.M. Weaver, *The extracellular matrix at a glance.* Journal of Cell Science, 2010. **123**(24): p. 4195-4200.

9. Egeblad, M., M.G. Rasch, and V.M. Weaver, *Dynamic interplay between the collagen scaffold and tumor evolution.* Current Opinion in Cell Biology, 2010. **22**(5): p. 697-706.

10. Lu, P.F., V.M. Weaver, and Z. Werb, *The extracellular matrix: A dynamic niche in cancer progression.* Journal of Cell Biology, 2012. **196**(4): p. 395-406.

11. Munn, L.L. and R.K. Jain, *The Forces of Cancer.* Scientist, 2016. **30**(4): p. 52-57.

12. Zanotelli, M.R., et al., *The Physical Microenvironment of Tumors: Characterization and Clinical Impact.* Biophysical Reviews and Letters, 2020. **15**(02): p. 51-82.

13. Feig, C., et al., *The pancreas cancer microenvironment.* Clinical cancer research : an official journal of the American Association for Cancer Research, 2012. **18**(16): p. 4266-4276.

14. Thompson, C.B., et al., *Enzymatic depletion of tumor hyaluronan induces antitumor responses in preclinical animal models.* Mol Cancer Ther, 2010. **9**(11): p. 3052-64.

15. Provenzano, P.P., et al., *Enzymatic targeting of the stroma ablates physical barriers to treatment of pancreatic ductal adenocarcinoma.* Cancer Cell, 2012. **21**(3): p. 418-29.

16. Northcott, J.M., et al., *Feeling Stress: The Mechanics of Cancer Progression and Aggression.* Front Cell Dev Biol, 2018. **6**: p. 17.

17. Cox, T.R. and J.T. Erler, *Remodeling and homeostasis of the extracellular matrix: implications for fibrotic diseases and cancer.* Disease Models & Mechanisms, 2011. **4**(2): p. 165-178.

18. Pickup, M.W., J.K. Mouw, and V.M. Weaver, *The extracellular matrix modulates the hallmarks of cancer.* Embo Reports, 2014. **15**(12): p. 1243-1253.

19. Hanahan, D. and R.A. Weinberg, *Hallmarks of Cancer: The Next Generation.* Cell, 2011. **144**(5): p. 646-674.

20. Pang, M.-F., et al., *Tissue stiffness and hypoxia modulate the integrin-linked kinase ILK to control breast cancer stem-like cells.* Cancer Research, 2016.

21. Guan, J.L., *Role of focal adhesion kinase in integrin signaling.* Int J Biochem Cell Biol, 1997. **29**(8-9): p. 1085-96.

22. Gilmore, A.P., et al., *Integrin-mediated survival signals regulate the apoptotic function of Bax through its conformation and subcellular localization.* J Cell Biol, 2000. **149**(2): p. 431-46.

23. Jablonska-Trypuc, A., M. Matejczyk, and S. Rosochacki, *Matrix metalloproteinases (MMPs), the main extracellular matrix (ECM) enzymes in collagen degradation, as a target for anticancer drugs.* J Enzyme Inhib Med Chem, 2016. **31**(sup1): p. 177-183.

24. Liu, T., et al., *Telomerase activity is required for bleomycin-induced pulmonary fibrosis in mice.* The Journal of Clinical Investigation, 2007. **117**(12): p. 3800-3809.

25. Minchinton, A.I. and I.F. Tannock, *Drug penetration in solid tumours.* Nat Rev Cancer, 2006. **6**(8): p. 583-92.

26. Xiong, G.-F. and R. Xu, *Function of cancer cell-derived extracellular matrix in tumor progression.* Journal of Cancer Metastasis and Treatment, 2016. **2**(9): p. 357-64.

27. Jones, C.E., et al., *Stromal PTEN Regulates Extracellular Matrix Organization in the Mammary Gland.* Neoplasia, 2019. **21**(1): p. 132-145.

28. Bondareva, A., et al., *The lysyl oxidase inhibitor, beta-aminopropionitrile, diminishes the metastatic colonization potential of circulating breast cancer cells.* PLoS One, 2009. **4**(5): p. e5620.

29. Pickup, M.W., et al., *Stromally derived lysyl oxidase promotes metastasis of transforming growth factor-beta-deficient mouse mammary carcinomas.* Cancer Res, 2013. **73**(17): p. 5336-46.

30. Vander Heiden, M.G., L.C. Cantley, and C.B. Thompson, *Understanding the Warburg Effect: The Metabolic Requirements of Cell Proliferation.* Science (New York, N.Y.), 2009. **324**(5930): p. 1029-1033.

31. Salmon, H., et al., *Matrix architecture defines the preferential localization and migration of T cells into the stroma of human lung tumors.* J Clin Invest, 2012. **122**(3): p. 899-910.

32. Rockwell, S., et al., *Hypoxia and radiation therapy: Past history, ongoing research, and future promise.* Current molecular medicine, 2009. **9**(4): p. 442-458.

33. Gilkes, D.M., G.L. Semenza, and D. Wirtz, *Hypoxia and the extracellular matrix: drivers of tumour metastasis.* Nature reviews. Cancer, 2014. **14**(6): p. 430-439.

34. Wang, B., et al., *Targeting hypoxia in the tumor microenvironment: a potential strategy to improve cancer immunotherapy.* Journal of Experimental & Clinical Cancer Research, 2021. **40**(1): p. 24.

35. Netti, P.A., et al., *Role of extracellular matrix assembly in interstitial transport in solid tumors.* Cancer Res, 2000. **60**(9): p. 2497-503.

36. Gottesman, M.M., *Mechanisms of cancer drug resistance.* Annu Rev Med, 2002. **53**: p. 615-27.

37. Eikenes, L., et al., *Collagenase Increases the Transcapillary Pressure Gradient and Improves the Uptake and Distribution of Monoclonal Antibodies in Human Osteosarcoma Xenografts.* Cancer Research, 2004. **64**(14): p. 4768.

38. Hingorani, S.R., et al., *Phase Ib Study of PEGylated Recombinant Human Hyaluronidase and Gemcitabine in Patients with Advanced Pancreatic Cancer.* Clin Cancer Res, 2016. **22**(12): p. 2848-54.

39. Fang, M., et al., *Collagen as a double-edged sword in tumor progression.* Tumour Biology, 2014. **35**(4): p. 2871-2882.

40. Nieskoski, M.D., et al., *Separation of Solid Stress From Interstitial Fluid Pressure in Pancreas Cancer Correlates With Collagen Area Fraction.* J Biomech Eng, 2017. **139**(6).

41. Nia, H.T., et al., *Solid stress and elastic energy as measures of tumour mechanopathology.* Nature Biomedical Engineering, 2016. **1**: p. 0004.

42. Goetz, J.G., et al., *Biomechanical remodeling of the microenvironment by stromal caveolin-1 favors tumor invasion and metastasis.* Cell, 2011. **146**(1): p. 148-63.

43. Conklin, M.W., et al., *Collagen Alignment as a Predictor of Recurrence after Ductal Carcinoma <em>In Situ</em&gt.* Cancer Epidemiology Biomarkers & Prevention, 2018. **27**(2): p. 138.

44. Lattouf, R., et al., *Picrosirius red staining: a useful tool to appraise collagen networks in normal and pathological tissues.* J Histochem Cytochem, 2014. **62**(10): p. 751-8.

45. Wang, H., et al., *Elastography can map the local inverse relationship between shear modulus and drug delivery within the pancreatic ductal adenocarcinoma microenvironment.* Clin Cancer Res, 2018.

46. Li, J., et al., *Investigating the Contribution of Collagen to the Tumor Biomechanical Phenotype with Noninvasive Magnetic Resonance Elastography.* Cancer Research, 2019.

47. Kultti, A., et al., *Therapeutic targeting of hyaluronan in the tumor stroma.* Cancers (Basel), 2012. **4**(3): p. 873-903.

48. Jacobetz, M.A., et al., *Hyaluronan impairs vascular function and drug delivery in a mouse model of pancreatic cancer.* Gut, 2013. **62**(1): p. 112-U153.

49. DuFort, Christopher C., et al., *Interstitial Pressure in Pancreatic Ductal Adenocarcinoma Is Dominated by a Gel-Fluid Phase.* Biophysical Journal, 2016. **110**(9): p. 2106-2119.

50. Hirose, Y., et al., *Inhibition of Stabilin-2 elevates circulating hyaluronic acid levels and prevents tumor metastasis.* Proc Natl Acad Sci U S A, 2012. **109**(11): p. 4263-8.

51. Sato, N., et al., *Role of hyaluronan in pancreatic cancer biology and therapy: Once again in the spotlight.* Cancer Sci, 2016. **107**(5): p. 569-75.

52. McAtee, C.O., J.J. Barycki, and M.A. Simpson, *Emerging roles for hyaluronidase in cancer metastasis and therapy.* Advances in cancer research, 2014. **123**: p. 1-34.

53. Itano, N. and K. Kimata, *Altered hyaluronan biosynthesis in cancer progression.* Semin Cancer Biol, 2008. **18**(4): p. 268-74.

54. Cowman, M.K., et al., *The Content and Size of Hyaluronan in Biological Fluids and Tissues.* Frontiers in Immunology, 2015. **6**: p. 261.

55. Bourguignon, L.Y.W., et al., *Interaction of Low Molecular Weight Hyaluronan (LMW-HA) with CD44 and Toll-Like Receptors Promotes the Actin Filament-Associated Protein (AFAP-110)-Actin Binding and MyD88-NFκB Signaling Leading to Pro-inflammatory Cytokine/Chemokine Production and Breast Tumor Invasion.* Cytoskeleton (Hoboken, N.j.), 2011. **68**(12): p. 671-693.

56. Auvinen, P., et al., *Hyaluronan in peritumoral stroma and malignant cells associates with breast cancer spreading and predicts survival.* Am J Pathol, 2000. **156**(2): p. 529-36.

57. Neesse, A., et al., *Stromal biology and therapy in pancreatic cancer: a changing paradigm.* Gut, 2015. **64**(9): p. 1476-84.

58. Tammi, R.H., et al., *Hyaluronan in human tumors: pathobiological and prognostic messages from cell-associated and stromal hyaluronan.* Semin Cancer Biol, 2008. **18**(4): p. 288-95.

59. Kultti, A., et al., *Accumulation of extracellular hyaluronan by hyaluronan synthase 3 promotes tumor growth and modulates the pancreatic cancer microenvironment.* Biomed Res Int, 2014. **2014**: p. 817613.

60. Toole, B.P., *Hyaluronan: from extracellular glue to pericellular cue.* Nature Reviews Cancer, 2004. **4**: p. 528.

61. Singha, N.C., et al., *Tumor-associated hyaluronan limits efficacy of monoclonal antibody therapy.* Mol Cancer Ther, 2015. **14**(2): p. 523-32.

62. Porsch, H., et al., *Efficient TGFbeta-induced epithelial-mesenchymal transition depends on hyaluronan synthase HAS2.* Oncogene, 2013. **32**(37): p. 4355-65.

63. Liang, J., D. Jiang, and P.W. Noble, *Hyaluronan as a therapeutic target in human diseases.* Advanced drug delivery reviews, 2016. **97**: p. 186-203.

64. Sohr, S. and K. Engeland, *RHAMM is differentially expressed in the cell cycle and downregulated by the tumor suppressor p53.* Cell Cycle, 2008. **7**(21): p. 3448-3460.

65. Godar, S., et al., *Growth-inhibitory and tumor- suppressive functions of p53 depend on its repression of CD44 expression.* Cell, 2008. **134**(1): p. 62-73.

66. Thapa, R. and G.D. Wilson, *The Importance of CD44 as a Stem Cell Biomarker and Therapeutic Target in Cancer.* Stem Cells International, 2016. **2016**: p. 2087204.

67. Heldin, P., et al., *HAS2 and CD44 in breast tumorigenesis.* Adv Cancer Res, 2014. **123**: p. 211-29.

68. Schwertfeger, K.L., et al., *Hyaluronan, Inflammation, and Breast Cancer Progression.* Front Immunol, 2015. **6**: p. 236.

69. de la Motte, C.A. and J.A. Drazba, *Viewing Hyaluronan: Imaging Contributes to Imagining New Roles for This Amazing Matrix Polymer.* Journal of Histochemistry and Cytochemistry, 2011. **59**(3): p. 252-257.

70. Jadin, L., et al., *Characterization of a Novel Recombinant Hyaluronan Binding Protein for Tissue Hyaluronan Detection.* Journal of Histochemistry & Cytochemistry, 2014. **62**(9): p. 672-683.

71. Jain, R.K., J.D. Martin, and T. Stylianopoulos, *The Role of Mechanical Forces in Tumor Growth and Therapy.* Annual Review of Biomedical Engineering, Vol 16, 2014. **16**: p. 321-346.

72. Nia, H.T., L.L. Munn, and R.K. Jain, *Mapping Physical Tumor Microenvironment and Drug Delivery.* Clinical Cancer Research, 2019. **25**(7): p. 2024.

73. Meyers, M.A. and K.K. Chawla, *Mechanical Behavior of Materials*. 2 ed. 2008, Cambridge: Cambridge University Press.

74. Pepin, K.M., R.L. Ehman, and K.P. McGee, *Magnetic resonance elastography (MRE) in cancer: Technique, analysis, and applications.* Progress in Nuclear Magnetic Resonance Spectroscopy, 2015. **90-91**: p. 32-48.

75. Low, G., S.A. Kruse, and D.J. Lomas, *General review of magnetic resonance elastography.* World Journal of Radiology, 2016. **8**(1): p. 59-72.

76. Chaudhuri, O., et al., *Extracellular matrix stiffness and composition jointly regulate the induction of malignant phenotypes in mammary epithelium.* Nat Mater, 2014. **13**(10): p. 970-8.

77. Mouw, J.K., et al., *Tissue mechanics modulate microRNA-dependent PTEN expression to regulate malignant progression.* Nat Med, 2014. **20**(4): p. 360-7.

78. Wirtz, D., K. Konstantopoulos, and P.C. Searson, *The physics of cancer: the role of physical interactions and mechanical forces in metastasis.* Nat Rev Cancer, 2011. **11**(7): p. 512-22.

79. Holle, A.W., et al., *Cell-Extracellular Matrix Mechanobiology: Forceful Tools and Emerging Needs for Basic and Translational Research.* Nano letters, 2018. **18**(1): p. 1-8.

80. Pfeifer, C.R., et al., *Genome variation across cancers scales with tissue stiffness - an invasion-mutation mechanism and implications for immune cell infiltration.* Curr Opin Syst Biol, 2017. **2**: p. 103-114.

81. Voutouri, C., et al., *Role of Constitutive Behavior and Tumor-Host Mechanical Interactions in the State of Stress and Growth of Solid Tumors.* PLOS ONE, 2014. **9**(8): p. e104717.

82. Discher, D.E., P. Janmey, and Y.L. Wang, *Tissue cells feel and respond to the stiffness of their substrate.* Science, 2005. **310**(5751): p. 1139-43.

83. Jamin, Y., et al., *Exploring the biomechanical properties of brain malignancies and their pathologic determinants in vivo with magnetic resonance elastography.* Cancer Res, 2015. **75**(7): p. 1216-1224.

84. Swaminathan, V., et al., *Mechanical stiffness grades metastatic potential in patient tumor cells and in cancer cell lines.* Cancer Res, 2011. **71**(15): p. 5075-80.

85. Chamming's, F., et al., *Shear wave elastography of tumour growth in a human breast cancer model with pathological correlation.* Eur Radiol, 2013. **23**(8): p. 2079-86.

86. Oswald, L., et al., *Jamming transitions in cancer.* Journal of Physics D: Applied Physics, 2017. **50**(48): p. 483001.

87. Pfeifer, C.R., et al., *Constricted migration increases DNA damage and independently represses cell cycle.* Mol Biol Cell, 2018. **29**(16): p. 1948-1962.

88. Tse, J.M., et al., *Mechanical compression drives cancer cells toward invasive phenotype.* Proc Natl Acad Sci U S A, 2012. **109**(3): p. 911-6.

89. Stylianopoulos, T., et al., *Co-evolution of solid stress and interstitial fluid pressure in tumors during progression: Implications for vascular collapse.* Cancer research, 2013. **73**(13): p. 3833-3841.

90. Jain, R.K., *Antiangiogenesis strategies revisited: from starving tumors to alleviating hypoxia.* Cancer Cell, 2014. **26**(5): p. 605-22.

91. Hassid, Y., et al., *Non-Invasive Imaging of Barriers to Drug Delivery in Tumors.* Microvascular Research, 2008. **76**(2): p. 94-103.

92. Heldin, C.H., et al., *High interstitial fluid pressure - an obstacle in cancer therapy.* Nat Rev Cancer, 2004. **4**(10): p. 806-13.

93. Walker-Samuel, S., et al., *Investigating low-velocity fluid flow in tumors using convection-MRI.* Cancer Research, 2018.

94. Rofstad, E.K., et al., *Pulmonary and lymph node metastasis is associated with primary tumor interstitial fluid pressure in human melanoma xenografts.* Cancer Res, 2002. **62**(3): p. 661-4.

95. Jain, R.K. and L.T. Baxter, *Mechanisms of heterogeneous distribution of monoclonal antibodies and other macromolecules in tumors: significance of elevated interstitial pressure.* Cancer Res, 1988. **48**(24 Pt 1): p. 7022-32.

96. Song, J.W. and L.L. Munn, *Fluid forces control endothelial sprouting.* Proceedings of the National Academy of Sciences of the United States of America, 2011. **108**(37): p. 15342-15347.

97. Swartz, M.A. and A.W. Lund, *Lymphatic and interstitial flow in the tumour microenvironment: linking mechanobiology with immunity.* Nat Rev Cancer, 2012. **12**(3): p. 210-9.

98. Qazi, H., et al., *Cancer cell glycocalyx mediates mechanotransduction and flow-regulated invasion.* Integr Biol (Camb), 2013. **5**(11): p. 1334-43.

99. Hassid, Y., et al., *Noninvasive Magnetic Resonance Imaging of Transport and Interstitial Fluid Pressure in Ectopic Human Lung Tumors.* Cancer Research, 2006. **66**(8): p. 4159.

100. Liu, L.J. and M. Schlesinger, *MRI contrast agent concentration and tumor interstitial fluid pressure.* Journal of Theoretical Biology, 2016. **406**: p. 52-60.

101. Liu, L.J., et al., *Estimation of Tumor Interstitial Fluid Pressure (TIFP) Noninvasively.* PLoS ONE, 2016. **11**(7): p. e0140892.

102. Haider, M.A., et al., *Assessment of the tumor microenvironment in cervix cancer using dynamic contrast enhanced CT, interstitial fluid pressure and oxygen measurements.* Int J Radiat Oncol Biol Phys, 2005. **62**(4): p. 1100-7.

103. Gulliksrud, K., K.G. Brurberg, and E.K. Rofstad, *Dynamic contrast-enhanced magnetic resonance imaging of tumor interstitial fluid pressure.* Radiother Oncol, 2009. **91**(1): p. 107-13.

104. Gulliksrud, K., K. Galappathi, and E.K. Rofstad, *Interstitial fluid pressure and vascularity of intradermal and intramuscular human tumor xenografts.* Int J Radiat Oncol Biol Phys, 2011. **80**(1): p. 258-64.

105. Tan, L., et al., *A numerical framework for interstitial fluid pressure imaging in poroelastic MRE.* PLoS ONE, 2017. **12**(6): p. e0178521.

106. Pagé, G., et al., *Tumor Solid Stress: Assessment with MR Elastography under Compression of Patient-Derived Hepatocellular Carcinomas and Cholangiocarcinomas Xenografted in Mice.* Cancers (Basel), 2021. **13**(8).

107. Mpekris, F., et al., *Stress-mediated progression of solid tumors: effect of mechanical stress on tissue oxygenation, cancer cell proliferation, and drug delivery.* Biomech Model Mechanobiol, 2015. **14**(6): p. 1391-402.

108. Khan, S., et al., *Ormeloxifene Suppresses Desmoplasia and Enhances Sensitivity of Gemcitabine in Pancreatic Cancer.* Cancer Research, 2015. **75**(11): p. 2292.

109. Hu, L., et al., *An overview of hedgehog signaling in fibrosis.* Mol Pharmacol, 2015. **87**(2): p. 174-82.

110. Olive, K.P., et al., *Inhibition of Hedgehog Signaling Enhances Delivery of Chemotherapy in a Mouse Model of Pancreatic Cancer.* Science (New York, N.Y.), 2009. **324**(5933): p. 1457-1461.

111. Rhim, A.D., et al., *Stromal elements act to restrain, rather than support, pancreatic ductal adenocarcinoma.* Cancer Cell, 2014. **25**(6): p. 735-47.

112. Ko, A.H., et al., *A Phase I Study of FOLFIRINOX Plus IPI-926, a Hedgehog Pathway Inhibitor, for Advanced Pancreatic Adenocarcinoma.* Pancreas, 2016. **45**(3): p. 370-5.

113. Chauhan, V.P., et al., *Angiotensin inhibition enhances drug delivery and potentiates chemotherapy by decompressing tumour blood vessels.* Nature Communications, 2013. **4**: p. 2516.

114. Diop-Frimpong, B., et al., *Losartan inhibits collagen I synthesis and improves the distribution and efficacy of nanotherapeutics in tumors.* Proc Natl Acad Sci U S A, 2011. **108**(7): p. 2909-14.

115. Coulson, R., et al., *The angiotensin receptor blocker, Losartan, inhibits mammary tumor development and progression to invasive carcinoma.* Oncotarget, 2017. **8**(12): p. 18640-18656.

116. Liu, J., et al., *TGF-beta blockade improves the distribution and efficacy of therapeutics in breast carcinoma by normalizing the tumor stroma.* Proc Natl Acad Sci U S A, 2012. **109**(41): p. 16618-23.

117. Cathcart, J., A. Pulkoski-Gross, and J. Cao, *Targeting matrix metalloproteinases in cancer: Bringing new life to old ideas.* Genes & Diseases, 2015. **2**(1): p. 26-34.

118. Chen, J., et al., *Efficacy and safety profile of celecoxib for treating advanced cancers: a meta-analysis of 11 randomized clinical trials.* Clin Ther, 2014. **36**(8): p. 1253-63.

119. Sobolewski, C., et al., *The role of cyclooxygenase-2 in cell proliferation and cell death in human malignancies.* Int J Cell Biol, 2010. **2010**: p. 215158.

120. Greenhough, A., et al., *The COX-2/PGE 2 pathway: key roles in the hallmarks of cancer and adaptation to the tumour microenvironment.* Carcinogenesis, 2009. **30**(3): p. 377-386.

121. Esbona, K., et al., *COX-2 modulates mammary tumor progression in response to collagen density.* Breast Cancer Res, 2016. **18**(1): p. 35.

122. Levental, K.R., et al., *Matrix Crosslinking Forces Tumor Progression by Enhancing Integrin Signaling.* Cell, 2009. **139**(5): p. 891-906.

123. Erler, J.T., et al., *Hypoxia-induced lysyl oxidase is a critical mediator of bone marrow cell recruitment to form the pre-metastatic niche.* Cancer cell, 2009. **15**(1): p. 35-44.

124. Tang, H., et al., *Lysyl oxidase drives tumour progression by trapping EGF receptors at the cell surface.* Nature communications, 2017. **8**: p. 14909-14909.

125. Ferreira, S., et al., *LOXL2 Inhibitors and Breast Cancer Progression.* Antioxidants (Basel), 2021. **10**(2).

126. Johnston, K.A. and K.M. Lopez, *Lysyl oxidase in cancer inhibition and metastasis.* Cancer Letters, 2018. **417**: p. 174-181.

127. Jiang, H., et al., *Targeting focal adhesion kinase renders pancreatic cancers responsive to checkpoint immunotherapy.* Nat Med, 2016. **22**(8): p. 851-60.

128. Aboubakar Nana, F., et al., *Therapeutic Potential of Focal Adhesion Kinase Inhibition in Small Cell Lung Cancer.* Molecular Cancer Therapeutics, 2019. **18**(1): p. 17.

129. Shen, M., et al., *Tinagl1 Suppresses Triple-Negative Breast Cancer Progression and Metastasis by Simultaneously Inhibiting Integrin/FAK and EGFR Signaling.* Cancer Cell, 2019. **35**(1): p. 64-80.e7.

130. Dawson, J.C., et al., *Targeting FAK in anticancer combination therapies.* Nature Reviews Cancer, 2021. **21**(5): p. 313-324.

131. Mohanty, A., et al., *FAK-targeted and combination therapies for the treatment of cancer: an overview of phase I and II clinical trials.* Expert Opin Investig Drugs, 2020. **29**(4): p. 399-409.

132. Vennin, C., et al., *Transient tissue priming via ROCK inhibition uncouples pancreatic cancer progression, sensitivity to chemotherapy, and metastasis.* Sci Transl Med, 2017. **9**(384).

133. Clayton, N.S. and A.J. Ridley, *Targeting Rho GTPase Signaling Networks in Cancer.* Frontiers in Cell and Developmental Biology, 2020. **8**(222).

134. Eikenes, L., et al., *Effect of collagenase and hyaluronidase on free and anomalous diffusion in multicellular spheroids and xenografts.* Anticancer Res, 2010. **30**(2): p. 359-68.

135. Dolor, A. and F.C. Szoka, *Digesting a Path Forward: The Utility of Collagenase Tumor Treatment for Improved Drug Delivery.* Molecular Pharmaceutics, 2018. **15**(6): p. 2069-2083.

136. Xu, S., et al., *The role of collagen in cancer: from bench to bedside.* Journal of Translational Medicine, 2019. **17**(1): p. 309.

137. Whatcott, C.J., et al., *Targeting the tumor microenvironment in cancer: why hyaluronidase deserves a second look.* Cancer Discov, 2011. **1**(4): p. 291-6.

138. Stylianopoulos, T., et al., *Causes, consequences, and remedies for growth-induced solid stress in murine and human tumors.* Proceedings of the National Academy of Sciences, 2012. **109**(38): p. 15101-15108.

139. Doherty, G.J., M. Tempero, and P.G. Corrie, *HALO-109-301: a Phase III trial of PEGPH20 (with gemcitabine and nab-paclitaxel) in hyaluronic acid-high stage IV pancreatic cancer.* Future Oncol, 2018. **14**(1): p. 13-22.

140. Tolba, M.F. and H.A. Omar, *Immunotherapy, an evolving approach for the management of triple negative breast cancer: Converting non-responders to responders.* Critical Reviews in Oncology/Hematology, 2018. **122**: p. 202-207.

141. Clift, R., et al., *Abstract 641: PEGylated recombinant hyaluronidase PH20 (PEGPH20) enhances tumor infiltrating CD8⁺ T cell accumulation and improves checkpoint inhibitor efficacy in murine syngeneic breast cancer models.* Cancer Research, 2017. **77**(13 Supplement): p. 641.

142. Rosengren, S., et al., *Abstract 4886: PEGylated recombinant hyaluronidase PH20 (PEGPH20) enhances checkpoint inhibitor efficacy in syngeneic mouse models of cancer.* Cancer Research, 2016. **76**(14 Supplement): p. 4886.

143. Infante, J.R., et al., *Phase 1 trials of PEGylated recombinant human hyaluronidase PH20 in patients with advanced solid tumours.* British Journal Of Cancer, 2017. **118**: p. 153.

144. Hingorani, S.R., et al., *HALO 202: Randomized Phase II Study of PEGPH20 Plus Nab-Paclitaxel/Gemcitabine Versus Nab-Paclitaxel/Gemcitabine in Patients With Untreated, Metastatic Pancreatic Ductal Adenocarcinoma.* J Clin Oncol, 2018. **36**(4): p. 359-366.

145. Hakim, N., et al., *Why HALO 301 Failed and Implications for Treatment of Pancreatic Cancer.* Pancreas (Fairfax, Va.), 2019. **3**(1): p. e1-e4.

146. Kiyokawa, J., et al., *Modification of Extracellular Matrix Enhances Oncolytic Adenovirus Immunotherapy in Glioblastoma.* Clinical Cancer Research, 2021. **27**(3): p. 889.

147. O'Connor, J.P.B., et al., *Imaging biomarker roadmap for cancer studies.* Nature Reviews Clinical Oncology, 2017. **14**(3): p. 169-186.

148. Waterton, J.C. and L. Pylkkanen, *Qualification of imaging biomarkers for oncology drug development.* European Journal of Cancer, 2012. **48**(4): p. 409-415.

149. Hunter, D.J., et al., *Imaging Biomarker Validation and Qualification Report: Sixth OARSI Workshop on Imaging in Osteoarthritis combined with Third OA Biomarkers Workshop.* Osteoarthritis and Cartilage, 2013. **21**(7): p. 939-942.

150. Massoud, T.F. and S.S. Gambhir, *Molecular imaging in living subjects: seeing fundamental biological processes in a new light.* Genes Dev, 2003. **17**(5): p. 545-80.

151. Tichauer, K.M., et al., *Quantitative in vivo cell-surface receptor imaging in oncology: kinetic modeling and paired-agent principles from*

nuclear medicine and optical imaging. Phys Med Biol, 2015. **60**(14): p. R239-69.

152. Narunsky, L., et al., *Imaging aspects of the tumor stroma with therapeutic implications.* Pharmacology & Therapeutics, 2014. **141**(2): p. 192-208.

153. Li, X., et al., *Parallel Accumulation of Tumor Hyaluronan, Collagen and Other Drivers of Tumor Progression.* Clinical Cancer Research, 2018.

154. McRobbie, D.W., et al., *MRI from Picture to Proton*. 3 ed. 2017, Cambridge: Cambridge University Press.

155. Grossman, R.I., et al., *Magnetization transfer: theory and clinical applications in neuroradiology.* RadioGraphics, 1994. **14**(2): p. 279-290.

156. Padhani, A.R., et al., *Diffusion-Weighted Magnetic Resonance Imaging as a Cancer Biomarker: Consensus and Recommendations.* Neoplasia (New York, N.Y.), 2009. **11**(2): p. 102-125.

157. Li, J., et al., *Tumour biomechanical response to the vascular disrupting agent ZD6126 in vivo assessed by magnetic resonance elastography.* British Journal of Cancer, 2014. **110**(7): p. 1727-1732.

158. Streitberger, K.J., et al., *High-resolution mechanical imaging of glioblastoma by multifrequency magnetic resonance elastography.* PLoS One, 2014. **9**(10): p. e110588.

159. Schregel, K., et al., *Magnetic Resonance Elastography reveals effects of anti-angiogenic glioblastoma treatment on tumor stiffness and captures progression in an orthotopic mouse model.* Cancer Imaging, 2020. **20**(1): p. 35.

160. O'Connor, J.P.B., et al., *Dynamic contrast-enhanced imaging techniques: CT and MRI.* The British Journal of Radiology, 2011. **84**(Spec Iss 2): p. S112-S120.

161. Robinson, S.P., et al., *Monitoring the Vascular Response and Resistance to Sunitinib in Renal Cell Carcinoma In Vivo with Susceptibility Contrast MRI.* Cancer Res, 2017. **77**(15): p. 4127-4134.

162. Dennie, J., et al., *NMR imaging of changes in vascular morphology due to tumor angiogenesis.* Magn Reson Med, 1998. **40**(6): p. 793-9.

163. Tropres, I., et al., *Vessel size imaging.* Magn Reson Med, 2001. **45**(3): p. 397-408.

164. Burrell, J.S., et al., *MRI measurements of vessel calibre in tumour xenografts: Comparison with vascular corrosion casting.* Microvascular Research, 2012. **84**(3): p. 323-329.

165. McPhail, L.D. and S.P. Robinson, *Intrinsic Susceptibility MR Imaging of Chemically Induced Rat Mammary Tumors: Relationship to Histologic Assessment of Hypoxia and Fibrosis.* Radiology, 2009. **254**(1): p. 110-118.

166. Neeman, M., et al., *In vivo BOLD contrast MRI mapping of subcutaneous vascular function and maturation: validation by intravital microscopy.* Magn Reson Med, 2001. **45**(5): p. 887-98.

167. Robinson, S.P., F.A. Howe, and J.R. Griffiths, *Noninvasive monitoring of carbogen-induced changes in tumor blood flow and oxygenation by functional magnetic resonance imaging.* Int J Radiat Oncol Biol Phys, 1995. **33**(4): p. 855-9.

168. Almeida, G.S., et al., *Pre-clinical imaging of transgenic mouse models of neuroblastoma using a dedicated 3-element solenoid coil on a clinical 3T platform.* British journal of cancer, 2017. **117**(6): p. 791-800.

169. Jamin, Y., et al., *Intrinsic susceptibility MRI identifies tumors with ALKF1174L mutation in genetically-engineered murine models of high-risk neuroblastoma.* PloS one, 2014. **9**(3): p. e92886-e92886.

170. Jamin, Y., et al., *Evaluation of clinically translatable MR imaging biomarkers of therapeutic response in the TH-MYCN transgenic mouse model of neuroblastoma.* Radiology, 2013. **266**(1): p. 130-40.

171. Winfield, J.M., G.S. Payne, and N.M. deSouza, *Functional MRI and CT biomarkers in oncology.* Eur J Nucl Med Mol Imaging, 2015. **42**(4): p. 562-78.

172. Jensen, K.E., et al., *Magnetic resonance imaging of the bone marrow in patients with acute leukemia during and after chemotherapy. Changes in T1 relaxation.* Acta Radiol, 1990. **31**(4): p. 361-9.

173. Klein, J., et al., *Chemical exchange saturation transfer MRI to assess cell death in breast cancer xenografts at 7T.* Oncotarget, 2018. **9**(59): p. 31490-31501.

174. Li, W., et al., *Magnetization transfer MRI in pancreatic cancer xenograft models.* Magn Reson Med, 2012. **68**(4): p. 1291-7.

175. Lundbom, N., *Determination of magnetization transfer contrast in tissue: an MR imaging study of brain tumors.* American Journal of Roentgenology, 1992. **159**(6): p. 1279-1285.

176. Cai, K., et al., *Magnetic Resonance Imaging of Glutamate.* Nature medicine, 2012. **18**(2): p. 302-306.

177. Walker-Samuel, S., et al., *In vivo imaging of glucose uptake and metabolism in tumors.* Nature Medicine, 2013. **19**: p. 1067.

178. Ling, W., et al., *Assessment of glycosaminoglycan concentration in vivo by chemical exchange-dependent saturation transfer (gagCEST).* Proc Natl Acad Sci U S A, 2008. **105**(7): p. 2266-70.

179. Singh, A., et al., *Chemical exchange saturation transfer magnetic resonance imaging of human knee cartilage at 3 T and 7 T.* Magn Reson Med, 2012. **68**(2): p. 588-94.

180. Kogan, F., H. Hariharan, and R. Reddy, *Chemical Exchange Saturation Transfer (CEST) Imaging: Description of Technique and Potential Clinical Applications.* Current Radiology Reports, 2013. **1**(2): p. 102-114.

181. Charles-Edwards, E.M. and N.M. deSouza, *Diffusion-weighted magnetic resonance imaging and its application to cancer.* Cancer imaging : the official publication of the International Cancer Imaging Society, 2006. **6**(1): p. 135-143.

182. Sinkus, R., et al., *Apparent diffusion coefficient from magnetic resonance imaging as a biomarker in oncology drug development.* Eur J Cancer, 2012. **48**(4): p. 425-31.

183. Le Bihan, D., *What can we see with IVIM MRI?* NeuroImage, 2019. **187**: p. 56-67.

184. Doyley, M.M. and K.J. Parker, *Elastography: general principles and clincial applications.* Ultrasound clinics, 2014. **9**(1): p. 1-11.

185. Uff, C., et al., *Further characterization of changes in axial strain elastograms due to the presence of slippery tumor boundaries.* J Med Imaging (Bellingham), 2018. **5**(2): p. 021211.

186. Mariappan, Y.K., K.J. Glaser, and R.L. Ehman, *Magnetic resonance elastography: a review.* Clinical anatomy (New York, N.Y.), 2010. **23**(5): p. 497-511.

187. Muthupillai, R., et al., *Magnetic resonance elastography by direct visualization of propagating acoustic strain waves.* Science, 1995. **269**(5232): p. 1854-7.

188. Sinkus, R., et al., *Viscoelastic shear properties of in vivo breast lesions measured by MR elastography.* Magn Reson Imaging, 2005. **23**(2): p. 159-65.

189. Wang, J.-W., et al., *Ultrasound elastography as an imaging biomarker for detection of early tumor response to chemotherapy in a murine breast cancer model: a feasibility study.* The British journal of radiology, 2018. **91**(1085): p. 20170698-20170698.

190. Sigrist, R.M.S., et al., *Ultrasound Elastography: Review of Techniques and Clinical Applications.* Theranostics, 2017. **7**(5): p. 1303-1329.

191. Plekhanov, A.A., et al., *Histological validation of in vivo assessment of cancer tissue inhomogeneity and automated morphological segmentation enabled by Optical Coherence Elastography.* Scientific Reports, 2020. **10**(1): p. 11781.

192. Gubarkova, E.V., et al., *OCT-elastography-based optical biopsy for breast cancer delineation and express assessment of morphological/molecular subtypes.* Biomedical optics express, 2019. **10**(5): p. 2244-2263.

193. Klatt, D., et al., *Noninvasive assessment of the rheological behavior of human organs using multifrequency MR elastography: a study of brain and liver viscoelasticity.* Phys Med Biol, 2007. **52**(24): p. 7281-94.

194. Asbach, P., et al., *Assessment of liver viscoelasticity using multifrequency MR elastography.* Magn Reson Med, 2008. **60**(2): p. 373-9.

195. Sinkus, R., et al., *High-resolution tensor MR elastography for breast tumour detection.* Phys Med Biol, 2000. **45**(6): p. 1649-64.

196. Pepin, K.M., et al., *MR Elastography Analysis of Glioma Stiffness and IDH1-Mutation Status.* AJNR. American journal of neuroradiology, 2018. **39**(1): p. 31-36.

197. Jugé, L., et al., *Colon Tumor Growth and Antivascular Treatment in Mice: Complementary Assessment with MR Elastography and Diffusion-weighted MR Imaging.* Radiology, 2012. **264**(2): p. 436-444.

198. Gordic, S., et al., *Value of tumor stiffness measured with MR elastography for assessment of response of hepatocellular carcinoma to locoregional therapy.* Abdominal radiology (New York), 2017. **42**(6): p. 1685-1694.

199. Pepin, K.M., et al., *MR elastography derived shear stiffness--a new imaging biomarker for the assessment of early tumor response to chemotherapy.* Magnetic resonance in medicine, 2014. **71**(5): p. 1834-1840.

200. Guo, J., et al., *1537: Assessment of treatment response of lymphoma in an animal model with in vivo MR elastography.* Proceedings of the International Society of Magnetic Resonance in Medicine 26, 2018.

201. Robinson, S.P., et al., *Tumor vascular architecture and function evaluated by non-invasive susceptibility MRI methods and immunohistochemistry.* J Magn Reson Imaging, 2003. **17**(4): p. 445-54.

202. Zormpas-Petridis, K., et al., *MRI Imaging of the Hemodynamic Vasculature of Neuroblastoma Predicts Response to Anti-angiogenic Treatment.* Cancer Research, 2019: p. canres.3412.2018.

203. O'Connor, J.P., et al., *Dynamic contrast-enhanced MRI in clinical trials of antivascular therapies.* Nat Rev Clin Oncol, 2012. **9**(3): p. 167-77.

204. Vergauwen, E., et al., *Central nervous system gadolinium accumulation in patients undergoing periodical contrast MRI screening for hereditary tumor syndromes.* Hereditary Cancer in Clinical Practice, 2018. **16**: p. 2.

205. Cao, J., et al., *Dynamic contrast-enhanced MRI detects responses to stroma-directed therapy in mouse models of pancreatic ductal adenocarcinoma.* Clin Cancer Res, 2018.

206. Pasquini, L., et al., *Gadolinium-Based Contrast Agent-Related Toxicities.* CNS Drugs, 2018. **32**(3): p. 229-240.

207. Walker-Samuel, S., et al., *Non-invasive in vivo imaging of vessel calibre in orthotopic prostate tumour xenografts.* International Journal of Cancer, 2011. **130**(6): p. 1284-1293.

208. Yang, S., et al., *Use of Ultrasmall Superparamagnetic Iron Oxide Enhanced Susceptibility Weighted Imaging and Mean Vessel Density Imaging to Monitor Antiangiogenic Effects of Sorafenib on Experimental Hepatocellular Carcinoma.* Contrast media & molecular imaging, 2017. **2017**: p. 9265098-9265098.

209. Saida, Y., et al., *0919: Hyaluronan depletion improved intratumor pO2 and sensitized tumor to radiation therapy in pancreatic cancer model mouse.* Proceedings of the International Society of Magnetic Resonance in Medicine 29, 2021.

210. Ernest, L.M., et al., *Tissue-mimicking agar/gelatin materials for use in heterogeneous elastography phantoms.* Physics in Medicine & Biology, 2005. **50**(23): p. 5597.

211. Sack, I., et al., *Structure-sensitive elastography: on the viscoelastic powerlaw behavior of in vivo human tissue in health and disease.* Soft Matter, 2013. **9**(24): p. 5672-5680.

212. Sinkus, R., et al., *MR elastography of breast lesions: understanding the solid/liquid duality can improve the specificity of contrast-enhanced MR mammography.* Magn Reson Med, 2007. **58**(6): p. 1135-44.

213. Kilkenny, C., et al., *Improving bioscience research reporting: the ARRIVE guidelines for reporting animal research.* PLoS Biol, 2010. **8**(6): p. e1000412.

214. Workman, P., et al., *Guidelines for the welfare and use of animals in cancer research.* British Journal of Cancer, 2010. **102**(11): p. 1555-1577.

215. Clift, R., et al., *Remodeling the Tumor Microenvironment Sensitizes Breast Tumors to Anti-Programmed Death-Ligand 1 Immunotherapy.* Cancer Research, 2019. **79**(16): p. 4149.

216. Menke, H. and P. Vaupel, *Effect of injectable or inhalational anesthetics and of neuroleptic, neuroleptanalgesic, and sedative agents on tumor blood flow.* Radiat Res, 1988. **114**(1): p. 64-76.

217. Walker-Samuel, S., et al., *Robust estimation of the apparent diffusion coefficient (ADC) in heterogeneous solid tumors.* Magnetic Resonance in Medicine, 2009. **62**(2): p. 420-429.

218. Sinkus, R., et al., *Imaging anisotropic and viscous properties of breast tissue by magnetic resonance-elastography.* Magnetic Resonance in Medicine, 2005. **53**(2): p. 372-387.

219. Nieskoski, M.D., et al., *Collagen Complexity Spatially Defines Microregions of Total Tissue Pressure in Pancreatic Cancer.* Scientific Reports, 2017. **7**.

220. Ge, X., et al., *Test-Retest Performance of a 1-Hour Multiparametric MR Image Acquisition Pipeline With Orthotopic Triple-Negative Breast Cancer Patient-Derived Tumor Xenografts.* Tomography, 2019. **5**(3): p. 320-331.

221. Tamura, T., S. Usui, and M. Akiyama, *[Investigation of a phantom for diffusion weighted imaging that controlled the apparent diffusion coefficient using gelatin and sucrose].* Nihon Hoshasen Gijutsu Gakkai Zasshi, 2009. **65**(11): p. 1485-93.

222. Guo, J., et al., *Magnetization transfer contrast imaging in Niemann pick type C mouse liver.* J Magn Reson Imaging, 2003. **18**(3): p. 321-7.

223. Jiang, P., et al., *Effective targeting of the tumor microenvironment for cancer therapy.* Anticancer Res, 2012. **32**(4): p. 1203-12.

224. Shepard, H.M., *Breaching the Castle Walls: Hyaluronan Depletion as a Therapeutic Approach to Cancer Therapy.* Frontiers in Oncology, 2015. **5**: p. 192.

225. Chalkidou, A., et al., *Correlation between Ki-67 immunohistochemistry and 18F-fluorothymidine uptake in patients with cancer: A systematic review and meta-analysis.* Eur J Cancer, 2012. **48**(18): p. 3499-513.

226. McSheehy, P.M., et al., *Quantified tumor t1 is a generic early-response imaging biomarker for chemotherapy reflecting cell viability.* Clin Cancer Res, 2010. **16**(1): p. 212-25.

227. O'Connor, J.P.B., et al., *Quantifying Antivascular Effects of Monoclonal Antibodies to Vascular Endothelial Growth Factor: Insights from Imaging.* Clinical Cancer Research, 2009. **15**(21): p. 6674.

228. Afaq, A., A. Andreou, and D.M. Koh, *Diffusion-weighted magnetic resonance imaging for tumour response assessment: why, when and how?* Cancer Imaging, 2010. **10 Spec no A**(1a): p. S179-88.

229. Gillard, J.H., A. Waldman, and P.B. Barker, *Clinical MR Neuroimaging: Physiological and Functional Techniques*. Second edition ed. 2010: Cambridge University Press.

230. Bahn, J.D., et al., *Abstract 2501: PEGylated human recombinant hyaluronidase (PEGPH20) enhances radiotherapy in hyaluronan-rich solid tumors.* Cancer Research, 2011. **71**(8 Supplement): p. 2501.

231. Northey, J.J., L. Przybyla, and V.M. Weaver, *Tissue Force Programs Cell Fate and Tumor Aggression.* Cancer Discovery, 2017. **7**(11): p. 1224.

232. Dewhirst, M.W. and T.W. Secomb, *Transport of drugs from blood vessels to tumour tissue.* Nat Rev Cancer, 2017. **17**(12): p. 738-750.

233. Hall, T.J., et al., *Phantom materials for elastography.* IEEE Transactions on Ultrasonics, Ferroelectrics, and Frequency Control, 1997. **44**(6): p. 1355-1365.

234. Bamber, J.C., *Attenuation and Absorption*, in *Physical Principles of Medial Ultrasonics*. 2005, John Wiley & Sons, Ltd. p. 93-166.

235. Riegler, J., et al., *Tumor Elastography and Its Association with Collagen and the Tumor Microenvironment.* Clinical Cancer Research, 2018. **24**(18): p. 4455.

236. O'Connor, J.P.B., S.P. Robinson, and J.C. Waterton, *Imaging tumour hypoxia with oxygen-enhanced MRI and BOLD MRI.* The British journal of radiology, 2019. **92**(1095): p. 20180642-20180642.

237. Papanikolaou, N., et al., *Biexponential T2 relaxation time analysis of the brain: correlation with magnetization transfer ratio.* Invest Radiol, 2002. **37**(7): p. 363-7.

238. Papanikolaou, N., et al., *T2 relaxation time analysis in patients with multiple sclerosis: correlation with magnetization transfer ratio.* Eur Radiol, 2004. **14**(1): p. 115-22.

239. Goebell, E., et al., *Macromolecule content influences proton diffusibility in gliomas.* Eur Radiol, 2011. **21**(12): p. 2626-32.

240. Surov, A., H.J. Meyer, and A. Wienke, *Correlation between apparent diffusion coefficient (ADC) and cellularity is different in several tumors: a meta-analysis.* Oncotarget, 2017. **8**(35): p. 59492-59499.

241. Egnell, L., et al., *Stromal Collagen Content in Breast Tumors Correlates With In Vivo Diffusion-Weighted Imaging: A Comparison of Multi b-Value DWI With Histologic Specimen From Benign and Malignant Breast Lesions.* Journal of Magnetic Resonance Imaging, 2019. **n/a**(n/a).

242. Arias-Lorza, A.M. and N. Raghunand, *0949: ADC Decreases in Solid Tumors Following Monotherapy With PEGylated Recombinant Human Hyaluronidase: Results From Early-Phase Clincal Trials.* Proc. Intl. Soc. Mag. Reson. Med. 29., 2021.

243. Wang, H., et al., *Elastography Can Map the Local Inverse Relationship between Shear Modulus and Drug Delivery within the Pancreatic Ductal Adenocarcinoma Microenvironment.* Clinical Cancer Research, 2019. **25**(7): p. 2136.

244. Kakkad, S., et al., *Collagen fibers mediate MRI-detected water diffusion and anisotropy in breast cancers.* Neoplasia, 2016. **18**(10): p. 585-593.

245. Jugé, L., et al., *Microvasculature alters the dispersion properties of shear waves – a multi-frequency MR elastography study.* NMR in Biomedicine, 2015. **28**(12): p. 1763-1771.

246. Qayyum, A., et al., *Immunotherapy response evaluation with magnetic resonance elastography (MRE) in advanced HCC.* Journal for ImmunoTherapy of Cancer, 2019. **7**(1): p. 329.

247. Liu, Y., et al., *Imaging Biomarkers to Predict and Evaluate the Effectiveness of Immunotherapy in Advanced Non-Small-Cell Lung Cancer.* Frontiers in Oncology, 2021. **11**(773).

248. Jardim-Perassi, B.V., et al., *Multiparametric MRI and Coregistered Histology Identify Tumor Habitats in Breast Cancer Mouse Models.* Cancer Research, 2019. **79**(15): p. 3952.

249. Li, X., et al., *Abstract 3796: Pegylated human recombinant hyaluronidase PH20 reduces solid tumor hypoxia.* Cancer Research, 2012. **72**(8 Supplement): p. 3796.

250. Rodrigues, L.M., et al., *Tumor R2* is a prognostic indicator of acute radiotherapeutic response in rodent tumors.* J Magn Reson Imaging, 2004. **19**(4): p. 482-8.

251. O'Connor, J.P.B., et al., *Oxygen-enhanced MRI accurately identifies, quantifies, and maps tumor hypoxia in preclinical cancer models.* Cancer research, 2016. **76**(4): p. 787-795.

252. Sahai, E., et al., *A framework for advancing our understanding of cancer-associated fibroblasts.* Nature Reviews Cancer, 2020. **20**(3): p. 174-186.

253. Jiang, B., et al., *Stroma-Targeting Therapy in Pancreatic Cancer: One Coin With Two Sides?* Frontiers in Oncology, 2020. **10**(2272).

Conference proceedings & publications

Oral Presentations:

Reeves, E.L., Li, J., Boult, J.K.R., Blouw, B., Kang, D., Bamber, J.C., Jamin, Y., and Robinson, S.P., *Breast tumour response to PEGPH20-induced stromal modulation assessed by multiparametric MRI.* ISMRM 2020.

Reeves, E.L., *Imaging extracellular matrix modulation in vivo in mouse models of breast cancer.* ICR conference 2020.

Reeves, E.L., Li, J., Boult, J.K.R., Blouw, B., Kang, D., Bamber, J.C., Jamin, Y., and Robinson, S.P., *Non-invasive evaluation of PEGPH20-mediated hyaluronan degradation in vivo using an orthotopic breast tumour model and multiparametric MRI.* Postgraduate BC-ISMRM 2019.

Poster Presentations:

Reeves, E.L., Li, J., Zormpas-Petridis, K., Boult, J.K.R., Sullivan, J., Cummings, C., Blouw, B., Kang, D., Sinkus, R., Jamin, Y., Bamber, J.C., and Robinson, S.P., *MR elastography reveals a marked increase in breast cancer viscoelasticity in vivo following hyaluronan degradation by PEGPH20.* ISMRM 2021.

Reeves, E.L.*, Hoebart, J.*, Li, J., Sinkus, R., Jamin, Y., Bamber, J.C., Melcher, A., Harrington, K., Kramer-Marek, G.**, Robinson, S.P.**, *Can magnetic resonance elastography inform on tumour response to oncolytic virotherapy?* BACR Imaging Cancer 2021. Joint first* and senior** authors.

Reeves, E.L., Li, J., Boult, J.K.R., Blouw, B., Kang, D., Bamber, J.C., Jamin, Y., and Robinson, S.P., *Intrinsic susceptibility MRI can inform on tumour vascular decompression in response to the stromal targeted therapy PEGPH20.* ISMRM 2020.

Reeves, E.L., Li, J., Boult, J.K.R., Blouw, B., Kang, D., Bamber, J.C., Jamin, Y., and Robinson, S.P., *Non-Invasive Evaluation of Murine Breast Tumour Response to PEGPH20-Mediated Hyaluronan Degradation in vivo with Magnetic Resonance Imaging.* BACR Tumour Microenvironment Meeting 2019.

Reeves, E.L., Li, J., Zormpas-Petridis, K., Heindl, A., Boult, J.K.R., Cummings, C., Bamber, J.C., Yuan, Y., Sinkus, R., Jamin, Y., and Robinson, S.P., *Stiffness, measured in vivo by magnetic resonance elastography, correlates with collagen content in stromal-dense tumours.* Forces in Cancer Meeting 2018.

Published Papers:

Li, J., Zormpas-Petridis, K., Boult, J.K.R., **Reeves, E.L.,** Heindl, A., Vinci, M., Lopes, F., Cummings, C., Springer, C.J., Chesler, L., Jones, C., Bamber, J.C., Yuan, Y., Sinkus, R., Jamin, Y., and Robinson, S.P., *Investigating the Contribution of Collagen to the Tumor Biomechanical Phenotype with Noninvasive Magnetic Resonance Elastography.* Cancer Research, 2019.

In preparation & submitted:

Reeves, E.L., Li, J., Zormpas-Petridis, K., Sullivan, J., Cummings, C., Blouw, B., Kang, D., Sinkus, R., Bamber, J.C., Jamin, Y., and Robinson, S.P., *Monitoring breast tumour response to extracellular matrix modulation with multiparametric MRI.* **Full paper in preparation.**

Reeves, E.L., Li, J., Zormpas-Petridis, K., Sullivan, J., Cummings, C., Blouw, B., Kang, D., Sinkus, R., Bamber, J.C., Jamin, Y., and Robinson, S.P., *Investigating the contribution of hyaluronan (HA) to the breast tumour microenvironment using multiparametric MRI and histology.* **Abstract submitted to ISMRM 2022.**